Department of Physics and Astronomy

University of Heidelberg

Master thesis

in Physics

submitted by

Tobias Valentin Heldt

born in Ostfildern

2020

Strong-Field-Driven Electron Dynamics near an Ionization Threshold

This Master thesis has been carried out by

Tobias Valentin Heldt

at the

Max-Planck-Institut für Kernphysik

under the supervision of

Prof. Dr. Thomas Pfeifer

Strong-Field-Driven Electron Dynamics near an Ionization Threshold:

Excitation of atoms with light that spectrally spans across the ionization threshold leads to free electrons initially located close to the parent ions. The dynamics of these ionized electrons driven by external light fields are studied by transient-absorption spectroscopy on helium in this thesis. Implementing an *ab initio* simulation, the time-dependent Schrödinger equation (TDSE) is solved for a model atom, giving direct access to the strong-field-driven evolution of the electron's wave function. In a separate theoretical approach, absorption spectra are calculated based on classical trajectories. Experimentally, an extension of a transient-absorption beamline allowed polarization-dependent measurements. The recorded absorption spectra of helium, depending on the intensity of a superimposed near-infrared femtosecond laser pulse with both linear and circular polarization, are presented and discussed. The observed absorption features can be assigned to two intensity regimes. For moderate intensities, light-induced states adequately explain the observed structures in the absorption spectra in agreement with the TDSE simulations. For higher laser intensities, the photon picture breaks down and the analysis of the dipole moment in the time domain suggests an interpretation in terms of classical electron trajectories. The combined theoretical and experimental investigation provides access to regimes in which the classical description of strong-field-driven electron dynamics emerges.

Elektronendynamik nahe einer Ionisationsschwelle getrieben durch starke Felder:

Die Anregung von Atomen mit Licht, das spektral die Ionisationsschwelle umfasst, führt zu freien Elektronen, die sich zunächst in der Nähe der Mutterionen befinden. Die durch externe Lichtfelder getriebene Dynamik der ionisierten Elektronen wird in dieser Arbeit durch zeitaufgelöste Absorptionsspektroskopie an Helium untersucht. Durch die Implementierung einer *ab initio*-Simulation wird die zeitabhängige Schrödingergleichung (TDSE) für ein Modellatom gelöst, was einen direkten Zugang zur feldgetriebenen Entwicklung der Elektronen-Wellenfunktion ermöglicht. In einem separaten theoretischen Ansatz werden Absorptionsspektren auf der Basis klassischer Trajektorien berechnet. Experimentell erlaubte eine Erweiterung eines zeitaufgelösten Absorptionsspektroskopie-Aufbaus polarisationsabhängige Messungen. Die aufgezeichneten Absorptionsspektren von Helium, abhängig von der Intensität eines überlagerten Nahinfrarot-Femtosekunden-Laserpulses mit sowohl linearer als auch zirkularer Polarisation, werden vorgestellt und diskutiert. Die beobachteten Absorptionsmerkmale lassen sich zwei Intensitätsregimen zuordnen. Bei moderaten Intensitäten können lichtinduzierte Zustände die beobachteten Strukturen in den Absorptionsspektren in Übereinstimmung mit den TDSE-Simulationen erklären. Bei höheren Laserintensitäten bricht das Photonenbild zusammen und die Analyse des zeitabhängigen Dipolmoments legt eine Interpretation im Sinne klassischer Elektronentrajektorien nahe. Die kombinierte theoretische und experimentelle Untersuchung bietet den Zugang zu Regimen, in denen die klassische Beschreibung von Elektronendynamik getrieben durch starke Felder möglich wird.

Contents

Introduction

By the end of the 19th century, when most physical phenomena were believed to be understood, the emergence of quantum physics opened a door to a new world. It was a paradigm change from continuous quantities to a quantized description of nature, which was necessary to explain the spectrum of black-body radiation and the photoelectric effect. Over more than a hundred years, science has evolved tremendously and the quantum mechanical framework has established itself as an adequate description of atoms and their interaction with light.

Since the discovery of the photoelectric effect [1], the methods to examine light-matter interaction improved, so that by the end of the 20th century, they were finally pushed into an extreme regime. Especially the development of chirped pulse amplification [2] allowed for the production of light pulses only a couple of femtoseconds short ($1\,\mathrm{fs} = 1 \times 10^{-15}\,\mathrm{s}$), with a peak electric field comparable to the one the electrons experience by the atomic Coulomb potential. This technique led to the advent of high harmonic generation (HHG) [3], which converts visible or near-infrared (NIR) light into extreme ultraviolet radiation (XUV). The XUV spectral range is of interest, as most atoms exhibit transitions within it. Even more outstanding is another property of this radiation: Due to its very broad spectrum, the energy-time uncertainty principle allows extremely short pulses. The locked phase relation between the harmonics, which is necessary to achieve this, is inherent to the generation process [4]. Therefore, XUV pulses with a hundred attoseconds ($1\,\mathrm{as} = 1 \times 10^{-18}\,\mathrm{s}$) width are feasible to probe atomic systems on the intrinsic electron timescale.

The emerging tools of highly sophisticated quantum mechanics show attributes that can be classically interpreted. In this sense, the ability to excite a system at a sharply defined point of time is very helpful for triggering classical dynamics. The intense NIR light, which is able to generate these short XUV pulses, can itself very well be described classically as an oscillating electric field. But quantum physics is still required to describe the discretized energy levels of all atomic systems. However, only bound states have a distinct energy, the continuum is truly continuous. The continuum has a very simple classical description, namely an ionic core and a free, ionized electron, which can have an arbitrary amount of kinetic energy. In general, continua are not restricted to such a case, but appear in many systems, in which energy levels cannot be distinguished any more, e.g. in molecular bands or in solid-state models, where they are characterized by their density of states.

A prominent example of a semi-classical theory including a continuum is the three-step model, which describes high harmonic generation [5]. After the first quantum step, which

is tunnel ionization of the electron, the electron's motion is described classically. Only the trajectories returning to the nucleus can result in emittance of an XUV photon by quantum recombination.

Within this thesis, similar electron dynamics are investigated. However, instead of the tunnel ionization step of the HHG process, the atoms are ionized through an attosecond XUV pulse, which defines a clear starting time of the classical trajectory. This approach enables the study of electron dynamics for arbitrary field intensities because, contrary to HHG, vanishing tunnel ionization rates for low intensities impose no restriction. The observation of the triggered electron dynamics is optical. The transient absorption of a helium target is measured during interaction with a time-delay, intensity, and polarization controlled NIR pulse. The absorption spectra can be traced back to the system's dipole response in the time domain [6], which allows comparing with classical electron trajectories.

This thesis is structured as follows: The first chapter gives an overview of the theoretical concepts which are used throughout this work.

Thereafter, Chapter 2 introduces an *ab initio* simulation, which solves the time-dependent Schrödinger equation for a model helium atom. The numerical simulation illustrates the evolution of the electron wave function and it allows studying the transient absorption features qualitatively for arbitrary pulse parameters, e.g. central photon wavelength, pulse length or form of the excitation spectrum. The concepts of light-induced states (LIS) and laser-induced continuum structure (LICS) are studied.

In a second theoretical approach, Chapter 3 examines the option to simulate absorption spectra out of classical electron trajectories in the strong-field approximation. Different methods are compared and the influence of recurrences to the nucleus of the trajectories ('recollision' of the wave packet) is studied.

Chapter 4 presents the experimental setup which was used to perform the measurements and explains important measurement procedures. The focus lies on the implementation of an external NIR beam path and its stability characterization. This extension of the existing experiment enabled NIR polarization-dependent measurements.

Finally, Chapter 5 shows the results of the time-delay, intensity, and polarization-dependent measurements of the absorption spectrum around the first ionization potential of helium. The spectral absorption features in the temporal overlap of XUV and NIR are explained in two regimes of moderate (ponderomotive energy $U_\mathrm{p} \ll$ photon energy ω_0) and high ($U_\mathrm{p} \gtrsim \omega_0$) peak intensity.

Chapter 1

Theoretical Considerations

This chapter introduces the basic concepts which are necessary to understand the presented work in this thesis.

If not stated otherwise, atomic units are used. This means, that the electron mass m_e, the elementary charge e, the reduced Planck constant $\hbar$ and the Bohr radius a_0 are set to unity

$$1 = m_\mathrm{e} = e = \hbar = a_0.$$

From this it follows that all quantities can be expressed in atomic units, for instance intensity $1\,\mathrm{a.u.} = 3.55 \times 10^{16}\,\mathrm{W/cm^2}$.

1.1 Fundamentals of Quantum Mechanics

In non-relativistic quantum mechanics, the Schrödinger equation is one of the most fundamental formulations of the evolution of states $|\psi\rangle$

$$i\frac{\partial}{\partial t}|\psi\rangle = H|\psi\rangle\,. \tag{1.1}$$

H denotes the Hamiltonian, which is a measure of the system's energy. It is possible to represent the states either in position $\Psi(\boldsymbol{r},t)$ or in momentum space $\Phi(\boldsymbol{k},t)$. These representations are called wave functions and they are connected by the Fourier transformation $\mathcal{F}$:

$$\Psi(\boldsymbol{r},t) = \mathcal{F}^{-1}(\Phi(\boldsymbol{k},t)) \tag{1.2}$$

$$= \frac{1}{\sqrt{2\pi}}\int \mathrm{d}\boldsymbol{k}\exp(i\boldsymbol{k}\boldsymbol{r})\Phi(\boldsymbol{k},t). \tag{1.3}$$

1.2 Dispersion of a Free Gaussian Wave Packet

We assume a free Gaussian wave packet at rest with variance σ^2 at time $t = 0$

$$\Psi(\boldsymbol{r},0) = \left(\frac{1}{\sqrt{\pi}\sigma}\right)^{3/2}\exp\left(\frac{-\boldsymbol{r}^2}{2\sigma^2}\right). \tag{1.4}$$

The time evolution in momentum space is given by $\Phi(\boldsymbol{k},t) = \exp(-iHt)\Phi(\boldsymbol{k},0)$. Thus the time-dependent wave function in position space for the free Hamiltonian $H = \boldsymbol{k}^2/2$ is computed by

$$\Psi(\boldsymbol{r},t) = \mathcal{F}^{-1}\left[\exp\left(-i\frac{\boldsymbol{k}^2}{2}t\right)\mathcal{F}(\Psi(\boldsymbol{r},0))\right] \tag{1.5}$$

$$= \left(\frac{\sigma}{\sqrt{\pi(\sigma^2+it)}}\right)^{3/2}\exp\left(\frac{-\boldsymbol{r}^2}{2(\sigma^2+it)}\right). \tag{1.6}$$

$\mathcal{F}$ and $\mathcal{F}^{-1}$ denote the Fourier transformation and its inverse respectively. The absolute value squared of the wave function is

$$|\Psi(\boldsymbol{r},t)|^2 = \left(\frac{\sigma}{\sqrt{\pi(\sigma^4+t^2)}}\right)^3\exp\left(\frac{-\sigma^2\boldsymbol{r}^2}{\sigma^4+t^2}\right) \tag{1.7}$$

$$= \left(\frac{1}{\sqrt{\pi}\varsigma(t)}\right)^3\exp\left(\frac{-\boldsymbol{r}^2}{\varsigma^2(t)}\right), \tag{1.8}$$

which is a Gaussian with an increasing width $\varsigma(t)^2 = \sigma^2 + \frac{t^2}{\sigma^2}$. For more details see [7, 8].

1.3 Electron in an Electromagnetic Field

The Hamiltonian of an electron in a vector potential $\boldsymbol{A}(\boldsymbol{r},t)$ and scalar potential $V(\boldsymbol{r},t)$ reads

$$H = \frac{1}{2}\left(\boldsymbol{p} + \frac{1}{\mathrm{c}}\boldsymbol{A}(\boldsymbol{r},t)\right)^2 - V(\boldsymbol{r},t), \tag{1.9}$$

where $\boldsymbol{p}$ denotes the momentum operator and c the speed of light. Throughout this thesis, the wavelength of the light is always much larger than an atom, which is the investigated system. Additionally, the considered intensities are small enough that the magnetic field component doesn't matter. Thus, we can use the dipole approximation, which eliminates the spatial dependency of the field. The value of the field at the nucleus $\boldsymbol{r}_0$ is set to be valid for the full atom

$$\boldsymbol{A}(t) = \boldsymbol{A}(\boldsymbol{r}_0,t). \tag{1.10}$$

If we assume linear polarized light along the x direction $\mathcal{E}(t)\boldsymbol{e}_x$, the Hamiltonian can, by gauge transformation, be expressed in the length gauge

$$H = \frac{1}{2}\boldsymbol{p}^2 - V(\boldsymbol{r},t) - x\mathcal{E}(t). \tag{1.11}$$

1.4 From Hydrogen to Rydberg Atoms

Using the Coulomb potential $V(\boldsymbol{r}, t) = \frac{1}{|\boldsymbol{r}|}$, we obtain the Hamiltonian for the hydrogen atom in an external electric field

$$H = \frac{1}{2}\boldsymbol{p}^2 - \frac{1}{|\boldsymbol{r}|} - x\mathcal{E}(t). \tag{1.12}$$

The nuclear motion has been neglected in the above formula. It is only a minor contribution, as the reduced mass $\mu \approx m_\mathrm{e}$. Solving the Schrödinger equation for this Hamiltonian analytically without the external field, is possible and thus it is a standard problem in atomic physics and discussed in many textbooks (e.g. [9]). As a result, we obtain discrete energy states represented by atomic orbitals, each described by a set of quantum numbers. For small electric fields the additional part of the Hamiltonian can be treated in perturbation theory, which is done to describe the Stark effect, for example. In principle, there is an infinite number of states, as the principle quantum number n is not limited. Neglecting the angular momentum and the spin, the energy of the states is given by

$$E_n = -\frac{R_\mathrm{Ryd}}{n^2}, \tag{1.13}$$

where $R_\mathrm{Ryd} = 0.5\,\mathrm{a.u.} = 13.6\,\mathrm{eV}$ is the Rydberg energy. The negative sign indicates that these are bound states. Atoms in Rydberg states $n \gg 1$ show exciting properties. Among others their size becomes macroscopic in the order of μm and the polarizability scales with n^7 [10]. It is also interesting to note, that the atomic element is not as important any more, as the spacing of the energy levels is in principle the same in this regime. As the polarizability of the atoms increases strongly, there is a practical limitation to the principle quantum number. Atoms with $n = 700$ were observed [11], but at this region they are very easily ionizable by an electric field. Ionization means, that the electron is not bound any more to the nucleus. It has a positive energy, which is not discrete, as the free electron can have an arbitrary value of momentum. In other words, the transition from discrete Rydberg states to the continuum is smooth, especially under the influence of a strong electric field. This is the interesting regime, which is treated in this thesis.

1.5 Helium Atom

A helium atom consists of a doubly positively charged nucleus and two electrons $i = 1, 2$. Its Hamiltonian reads:

$$H = \sum_{\mathrm{i}=1}^{2}\left(\frac{1}{2}\boldsymbol{p}_\mathrm{i}^2 - \frac{2}{|\boldsymbol{r}_\mathrm{i}|}\right) + \underbrace{\frac{1}{|\boldsymbol{r}_1 - \boldsymbol{r}_2|}}_{\text{Coulomb repulsion between electrons}}. \tag{1.14}$$

Although it is very similar to the hydrogen Hamiltonian (1.12), the interaction between the electrons preclude an analytical solution of the Schrödinger equation with this Hamiltonian. An approximate solution can be found reconstructing the states out of hydrogen

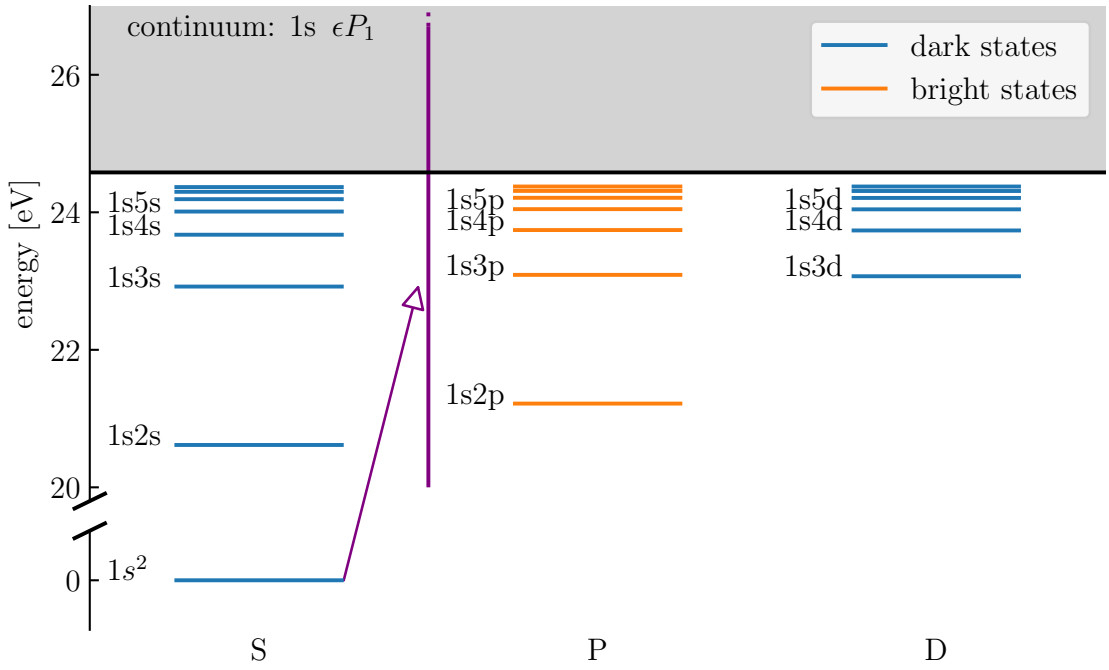

Figure 1.1: Energy levels of helium up to $n = 8$ and $L = 2$
Level scheme of singly excited (para)helium depending on angular momentum. The purple line indicates states which can be excited out of the ground state by a short XUV pulse. The energies are taken from [12].

wave functions. Thereby, one has to consider that the electrons are indistinguishable. Thus, the wave function has to be (anti-)symmetrized correctly. Additionally, perturbation theory can be used to treat the interaction term. Standard textbooks deal with this problem in detail, e.g. [9].

For the following discussion it is more important to recall the experimental level scheme of helium, shown in Figure 1.1. The ground state has zero angular momentum ($L = 0$), which is called an S orbital. Dipole transition rules only allow $\Delta L = \pm 1$, because the ground state is a singlet ($S = 0$). As a result, only P-states with $L = 1$ can be excited from the ground state in the dipole approximation. They are called bright states, because they are visible in an absorption spectrum. Excited states with $L = 0$ (S) or $L = 2$ (D) have out of symmetry reasons a vanishing transition dipole moment to the ground state. Thus, they cannot be observed directly, if the transition to the ground state is probed. Such states are referred to as dark states.

1.6 Linear Absorption

In linear optics, light-matter interaction is described by the dielectric susceptibility $\chi(\omega)$, which determines the response of the medium's polarization $P(\omega)$ on the electric field $\mathcal{E}(\omega)$

$$P(\omega) \propto \chi(\omega)\mathcal{E}(\omega). \tag{1.15}$$

In the case of an isotropic medium χ is a scalar, which is the reason why the problem can be treated in one dimension here. The polarization $P(\omega)$ connects to the microscopic world, as it is the mean dipole expectation value $d(\omega)$ scaled with the atomic number density ρ_{N}

$$P(\omega) = \rho_{\mathrm{N}} d(\omega). \tag{1.16}$$

The susceptibility can then be expressed as

$$\chi(\omega) \propto \rho_{\mathrm{N}} \frac{d(\omega)}{\mathcal{E}(\omega)}. \tag{1.17}$$

For a dilute atomic gas, $\chi(\omega)$ is sufficiently small to approximate the refractive index $n(\omega) = \sqrt{1+\chi(\omega)}$ by

$$n(\omega) \approx 1 + \frac{\Re(\chi(\omega))}{2} + i\frac{\Im(\chi(\omega))}{2}. \tag{1.18}$$

This means, that diffraction (real part) and absorption (imaginary part) can be treated independently from each other. The absorption coefficient $\alpha(\omega)$ depends only on the imaginary part of the susceptibility

$$\alpha(\omega) = \frac{\omega}{c}\Im(\chi(\omega)). \tag{1.19}$$

When light of intensity $I_0(\omega)$ propagates the distance z, the absorption reduces the intensity according to Beer-Lambert's law to

$$I(\omega, z) = I_0(\omega)\exp(-\alpha(\omega)z). \tag{1.20}$$

The absorbance $A(\omega)$ in units of optical density $OD(\omega)$, which is defined by $\frac{I(\omega,z)}{I_0(\omega)} = 10^{-A}$ is thus proportional to the absorption coefficient

$$A(\omega) = -\log 10\left(\frac{I(\omega,z)}{I_0(\omega)}\right) \propto \alpha(\omega). \tag{1.21}$$

Additionally, the absorption coefficient connects to the atomic cross section $\sigma(\omega)$ by

$$\alpha(\omega) = \rho_{\mathrm{N}}\sigma(\omega). \tag{1.22}$$

Combining equations (1.22),(1.21), (1.19) and (1.17) results in

$$\sigma(\omega) \propto A(\omega) \propto \omega\Im\left[\frac{d(\omega)}{\mathcal{E}(\omega)}\right]. \tag{1.23}$$

This equation connects the measurable quantity optical density with the atoms' dipole moment, which can be calculated in theoretical models. It shall be noted, that this formula is only correct if the electric field is a weak perturbation, which does not alter the population of the states significantly.

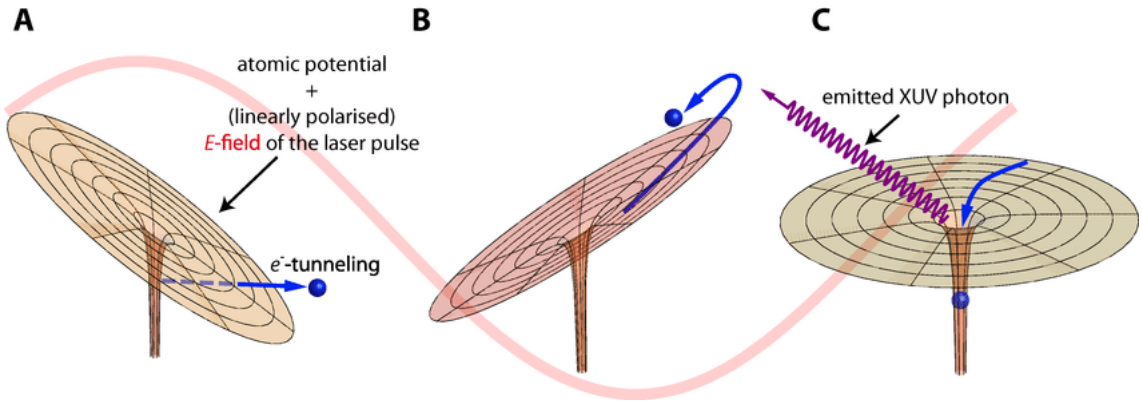

Figure 1.2: Three step model of HHG, taken from [15]
A An atom is tunnel ionized by a strong electric field. **B** The free electron follows a classical trajectory driven by the field. After half an optical cycle it is accelerated back to the nucleus. **C** The electron recombines with the original atom under emission of a high-energetic photon.

1.7 High-Harmonic Generation (HHG)

If an intense short-pulse laser is focused in an inert gas, one can observe the emission of odd harmonics, typically in the extreme ultraviolet (XUV) [3, 13]. Their phases are locked, which leads to the emergence of a train of attosecond pulses [4]. Experimental techniques allow to achieve a single attosecond pulse with a smooth spectrum (e.g. [14]).

1.7.1 Simple Man Three Step Model

The simplest model to explain the emergence of the high energetic light is semi-classical [5]. It consists of three steps, which are depicted in Figure 1.2. In a first step, the electron can tunnel out of the Coulomb potential due to the strong electric field, which modifies the total binding potential. Then, in the second step, the residual atomic potential is neglected and the evolution of the electron wave packet is described classically as trajectory. Since the optical cycle determines the direction of the force, the electron is first pushed away and then accelerated back to the nucleus. In the third step, the electron recombines with the original atom, i.e. it becomes bound again. Its kinetic energy and the ionization potential is released in a single high energetic photon.

1.7.2 Quantum Mechanical Description

Lewenstein et al. have presented a quantum theory that can recover the classical three step interpretation of HHG [16]. Based on the approximations that all bound states can be neglected except the ground state which negligible depletion and that in the continuum the potential has no effect on an electron, they derived the formula for the time-dependent

dipole moment $d(t)$

$$d(t) = \langle \Psi(t)|x|\Psi(t)\rangle \tag{1.24}$$

$$= i\int_0^t \mathrm{d}t' \int d^3p \quad \mathcal{E}(t')\; d_x(p + A(t'))\; d_x^*(p + A(t))\; e^{i\int_{t'}^t (p+A(t''))^2/2 + I_p\; \mathrm{d}t''}, \tag{1.25}$$

where t' denotes the time when the electron is freed by tunnel ionization, $\mathcal{E}$ is the electric field that triggers the tunneling, A the vector potential of the field, d_x the dipole matrix elements along the polarization direction ($d_x(p) = \langle p|x|\Psi_0\rangle$ for an momentum eigenstate $|p\rangle$), I_p the vector potential and p the canonical momentum of the electron. The phase of the integral is the quasi classical action $S(t,p,A) = \int_0^t \frac{(p+A(t'))^2}{2} + I_p \mathrm{d}t'$.

1.7.3 Assuming XUV Excitation

Within this thesis the dynamics of free electrons under the influence of a laser field in the vicinity of the parent atom are studied. Therefore, the electron is not tunnel-ionized but set free by a short XUV pulse. As the XUV pulse is much shorter than the other timescales, we will assume it to be a Dirac delta function: $\mathcal{E}(t') = \mathcal{E}\delta(t')$. This results in an ionization at time $t = 0$, so that equation (1.25) simplifies to

$$d(t) = i\int \mathrm{d}^3p \quad d_x(p + A(0))\; d_x^*(p + A(t))\; e^{i\int_0^t (p+A(t'))^2/2 + I_p \mathrm{d}t'}. \tag{1.26}$$

We can now introduce the velocity as $v(t) = p + A(t)$ and use the approximation that the dipole moment vanishes for velocities in a different direction than the laser polarization $d_x \propto \delta(v_y)\delta(v_z)$, which reduces the dimension of the integral

$$d(t) = i\int \mathrm{d}^3v \quad d_x(v(0))\; d_x^*(v(t))\; e^{i\int_0^t v(t')^2/2 + I_p \mathrm{d}t'} \tag{1.27}$$

$$= i\int \mathrm{d}v \quad d_x(v(0))\; d_x^*(v(t))\; e^{i\int_0^t v(t')^2/2 + I_p\; \mathrm{d}t'}. \tag{1.28}$$

This formula will allow us to calculate the dipole moment out of classical trajectories of the electrons.

1.8 Ponderomotive Energy

Due to its charge, an electron experiences in an electric field $\mathcal{E}(t)$ the acceleration $a(t) = \mathcal{E}(t)$ (in a.u.). Assuming a monochromatic light field $\mathcal{E}(t) = \mathcal{E}_0 \exp(-i\omega t)$ with frequency ω and vanishing initial velocity and position, integration results in

$$x(t) = -\frac{1}{\omega^2}\mathcal{E}(t). \tag{1.29}$$

This is a harmonic motion, whose time-averaged kinetic energy is

$$U_\mathrm{p} = \frac{1}{2}\omega^2\overline{x^2} \tag{1.30}$$

$$= \frac{\mathcal{E}_0^2}{4\omega^2} \tag{1.31}$$

$$= \frac{I}{4\omega^2}, \tag{1.32}$$

where I denotes the intensity of the light. The ponderomotive energy U_p is thus the cycle-averaged kinetic energy of a free electron in an oscillating electric field.

1.9 Reconstruction of the Strong-Field-Driven Dipole Response

The following is a key concept, which will be used extensively throughout the thesis. It was introduced by Veit Stooß *et al.* in [6]. The idea is to extract the time dependent-dipole moment, which is the response to an initial excitation, out of a single absorption spectrum.

Let's consider an atomic system which interacts with a weakly perturbing field $\mathcal{E}(t)$. This leads to a response of the system, namely an oscillating dipole moment $d(t)$. It will decay corresponding to the system's life time τ_s. During this time, there can be a time-dependent interaction $V(t)$, which modifies the dipole. This interaction can, for instance, experimentally be achieved by a strong near-infrared (NIR) laser pulse. Experimentally measurable is not the modified dipole moment $d(t, V(t))$ itself, but the absorption spectrum $A(\omega)$, in which the information is decoded (see eq. (1.23))

$$A(\omega) \propto \omega\Im\left[\frac{\mathcal{F}[d(t, V(t))]}{\mathcal{F}[\mathcal{E}(t)]}\right]. \tag{1.33}$$

If the initial weak excitation $\mathcal{E}(t)$ is much shorter than τ_s and the time scale of the perturbation $V(t)$, the problem can be treated in the impulsive limit. This means that the excitation can be assumed to be a Dirac delta function $\mathcal{E}(t) = \mathcal{E}\delta(t)$. This limit is for example justified, if the excitation is an extreme ultraviolet (XUV) pulse with a few hundred attosecond width, and the interaction is due to a strong NIR pulse with a half-cycle time of more than a femtosecond. Veit Stooß *et al.* have proven, that in this limit, the dipole response can be reconstructed due to causality by a simple Fourier transform

$$d(t, V(t)) \propto \mathcal{F}^{-1}[iA(\omega)] = \frac{1}{2\pi}\int_{-\infty}^{\infty} iA(\omega)\exp(-i\omega t)\mathrm{d}\omega \qquad \text{for } t > 0. \tag{1.34}$$

The time-dependent dipole moment $d(t, V(t))$ is in this case a complex quantity and contains amplitude and phase.

$A(\omega)$ is the full absorption spectrum. Experimentally, it is often not accessible due to limitations of the spectrometer. It is a valid approach to use only a part of the absorption spectrum for the reconstruction. Formally, this corresponds to a window function $w(\omega)$,

which cuts out the spectral features of interest

$$d_{\mathrm{part}}(t, V(t)) \propto \mathcal{F}^{-1}[iw(\omega)A(\omega)]. \tag{1.35}$$

$d_{\mathrm{part}}(t, V(t))$ denotes the dipole moment which corresponds to the spectral feature within $w(\omega)$, e.g. an absorption line or the continuum. In the following, the index will be omitted.

In this thesis, often the influence of the NIR interaction ($V(t)$) is the quantity of interest. It is quantified by the difference of the absolute reconstructed dipole moment with and without NIR interaction

$$|d(t)| - |d_{\mathrm{noNIR}}(t)| = |d(t, V(t))| - |d(t, V(t) = 0)|. \tag{1.36}$$

Chapter 2

Solving the Time Dependent Schrödinger Equation (TDSE) for a Model Helium Atom

In a previous attosecond transient absorption experiment interesting spectral features have been observed in the continuum of single excited helium. Some of the observations can be explained by the ponderomotive energy shift of the electrons [17]. Especially in the pulse overlap of XUV and NIR light, there seem to be additional influences on the spectrum. To explore the relevant features of the system, a time dependent Schrödinger equation simulation was set up.

Our aim is to solve the Schrödinger equation (given by (1.1)) for the Hamiltonian of a helium atom in a light field, which is given by the following expression in length gauge and dipole approximation according to (1.14) and (1.11):

$$H = \sum_{\mathrm{i}=1}^{2} \left(\frac{1}{2}\boldsymbol{p}_{\mathrm{i}}^2 - \frac{2}{|\boldsymbol{r}_{\mathrm{i}}|} - \boldsymbol{r}_{\mathrm{i}}\boldsymbol{\mathcal{E}} \right) + \frac{1}{|\boldsymbol{r}_1 - \boldsymbol{r}_2|}. \tag{2.1}$$

2.1 Method

The simulation consists of a split step algorithm that propagates the electronic wave function alternating between real and momentum space. The following approximations are used to obtain a feasible numerical problem:

- Propagation in one spacial dimension:
  Reducing the dimensionality from three to one spacial dimensions lowers the needed computational power dramatically. It has been shown in previous studies that fundamental features of the dimensionally reduced system still fit to experimental observations [18, 19].

- Using a discretized, finite grid:
  Numerical solutions are only possible if the quantities are discrete. The grid on which the wave function is defined in the simulation consists of $N = 4096$ points with a

spacing of $dx = 0.25\,\text{a.u.}$ thus $x = -511.75\,\text{a.u.}$ to $512\,\text{a.u.}$ The origin $x = 0\,\text{a.u.}$ corresponds to the nucleus position.

- Absorbing boundaries:
  As a consequence of the finite grid another modification is necessary. To avoid that the parts of the wave function which leave on one side of the grid reappear on the other side, absorbing boundaries are added to the model. They are implemented by adding an imaginary part to the potential, which leads to an effective damping of the wave function's amplitude. This imaginary potential is zero for $|x| \leq 350\,\text{a.u.}$ and rises outside of this region with a $\cos^2$ function to a value of 0.01 at the boundaries. The parameters are chosen to minimize reflections and effects on all bound states.

- Single active electron (SAE) approximation:
  Although we try to model helium with two electrons, the electron-electron interactions are neglected. The interesting regime in this study is the first ionization continuum of helium at $I_p = 24.58\,\text{eV}$. The first doubly excited states have an energy of over $60\,\text{eV}$. Thus we can assume that the second electron plays a minor role in our study.

- Soft-core potential:
  The coulomb potential $V(x) = \frac{-1}{|x|}$ exhibits a singularity at the origin which is troublesome for a numerical algorithm. Therefore, the simulation runs with the soft-core potential $V(x) = \frac{-1}{\sqrt{x^2+a}}$ with the soft-core parameter $a = 0.483$. This parameter has been optimized to fit the ionization edge of the model system with the experimental I_p of helium. The validity of the soft-core potential has been discussed in [18].

The real potential of the helium atom in an external electric field $\boldsymbol{\mathcal{E}}$ in dipole approximation,

$$V(\boldsymbol{r}, t) = \sum_{\mathrm{i}=1}^{2} \frac{-2}{|\boldsymbol{r}_\mathrm{i}|} + \frac{1}{|\boldsymbol{r}_1 - \boldsymbol{r}_2|} - \boldsymbol{r}\boldsymbol{\mathcal{E}}(0, t), \tag{2.2}$$

transforms with all approximations to:

$$V(x, t) = \frac{-1}{\sqrt{x^2 + a}} - x\mathcal{E}(0, t) - iV_{\text{absorb}}(x). \tag{2.3}$$

Figure 2.1 a) and b) illustrate the used approximations graphically.

Using the approximated potential from above the Hamiltonian that needs to be solved is given by:

$$H(x, p, t) = \underbrace{\frac{p^2}{2m}}_{T(p)} + \underbrace{\frac{-1}{\sqrt{x^2 + a}} - x\mathcal{E}(0, t) - iV_{\text{absorb}}(x)}_{V(x,t)}. \tag{2.4}$$

The first part depends on momentum $T(p) = \frac{p^2}{2m}$ and the second part is a potential,

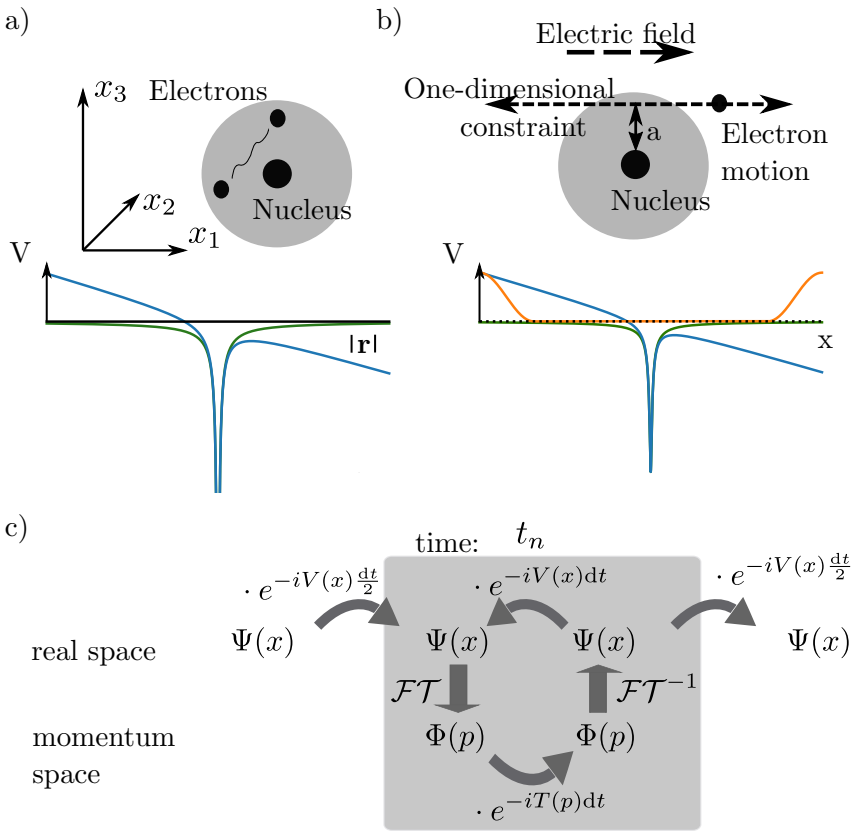

Figure 2.1: Method used for TDSE simulations
a) Artistic illustration of the helium atom, and potential. The gray shaded area depicts the electrons orbital. In green (blue) the Coulomb potential without(with) a laser interaction in dipole approximation is shown. **b)** Illustration of the 1D model with soft-core potential (graphics idea by [20]). In green (blue) the soft-core potential without(with) a laser interaction in dipole approximation is shown. The imaginary part of the potential is shown in orange. **c)** Chart of the split-step algorithm principle. The gray shaded part is repeated for each time step.

which is a function of position and time $V(x,t)$. The remaining task is to calculate the evolution of a wave function with this Hamiltonian. This problem is solved with a split step algorithm that propagates the electronic wave function alternating in real and momentum space. The propagation operator $U(t+\mathrm{d}t,t) = e^{-iH(t)\mathrm{d}t}$ describes the evolution of a wave function from t to $t+\mathrm{d}t$ by the equation:

$$\Psi(x,t+\mathrm{d}t,t) = U(t+\mathrm{d}t,t)\Psi(x,t). \tag{2.5}$$

The here applied split step algorithm in second order approximates the propagation operator by:

$$U(t+\mathrm{d}t,t) = e^{-i[T(p)+V(x,t)]\mathrm{d}t} \tag{2.6}$$

$$\approx e^{-iV(x,t+\mathrm{d}t)\frac{\mathrm{d}t}{2}} \cdot e^{-iT(p)\mathrm{d}t} \cdot e^{-iV(x,t)\frac{\mathrm{d}t}{2}}. \tag{2.7}$$

This simplifies solving the Schrödinger equation to multiplying complex numbers and applying Fourier transformations. Figure 2.1 c) shows a flow chart of the resulting computational steps. The gray shaded part is repeated until the final time is reached. The first and the last propagation step need to be over half the time interval $\frac{\mathrm{d}t}{2}$ to achieve a higher accuracy. As time step size $\mathrm{d}t = 0.05\,\mathrm{a.u.} = 1.2\,\mathrm{as} \mathrel{\hat{=}} 540\,\mathrm{eV}$ is used, which is much smaller than any time scale of the investigated system.

It is not only possible to include the light-matter interaction during the step in real space (length gauge) but also in momentum space propagation (velocity gauge). Including all approximations that were discussed, the Hamiltonian reads in velocity gauge:

$$H(x,p,t) = \frac{1}{2}\left(p + \frac{1}{\mathrm{c}}A(0,t)\right)^2 - \frac{-1}{\sqrt{x^2+a}} + iV_{\mathrm{absorb}}(x), \tag{2.8}$$

where $A(t) = -c\int_{-\infty}^{t}\mathrm{d}t'\mathcal{E}(t')$ denotes a vector potential. The differences between the two gauges have already been discussed elsewhere [21, 22], and should not be a topic in this thesis (see appendix B.3 for a brief comparison). If not stated otherwise the velocity gauge is used throughout this thesis.

Of course the above presented method will not reproduce the states of the real helium atom. The energy levels which live on the grid are depicted in 2.2. There are even and odd states, which consist of symmetric and antisymmetric wave functions in real space. The ground state Ψ_0 is even. The full wave function can be represented as $\Psi(t) = (1-a)\Psi_0 + a\Psi_{\mathrm{e}}$, where Ψ_e stands for an arbitrary superposition of all excited wave functions and $a \ll 1$ is the excited fraction. As the excitation is weak, the dipole moment can be approximated as:

$$d(t) = \langle\Psi(t)|x|\Psi(t)\rangle \tag{2.9}$$

$$\approx \langle\Psi_{\mathrm{e}}|x|\Psi_0\rangle\rangle + \underbrace{\langle\Psi_0|x|\Psi_0\rangle\rangle}_{=0} + c.c. \tag{2.10}$$

This means, only states with a non vanishing dipole moment to the ground state will be

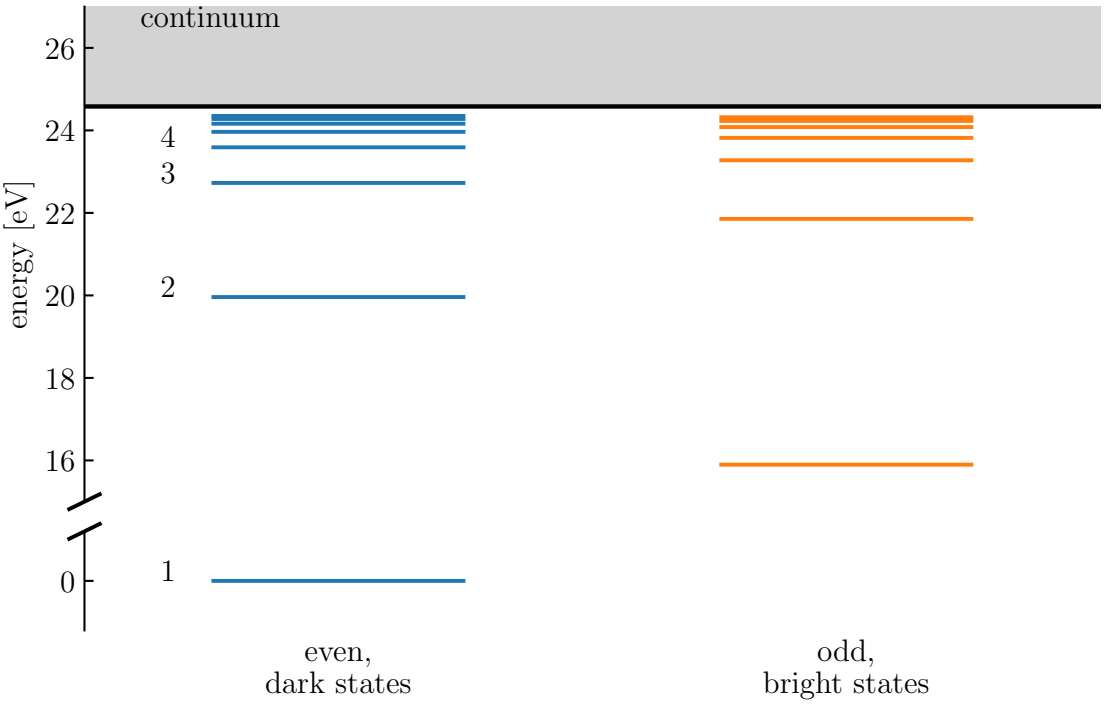

Figure 2.2: Level scheme of the used model, the continuum is shown in gray.

observable in the absorption spectrum. The even states correspond to dipole forbidden dark states. As the states' energies are not the same as for helium, all statements deduced from this model will be qualitative.

2.2 Evolution of a Wave Function

This section studies the evolution in time of the computed wave function $\Psi(x)$, to give an idea of the wave function dynamics during light-matter interaction.

2.2.1 Excitation with a Gaussian XUV Pulse

Figure 2.3 shows the evolution of a wave function. We look at the absolute value of the wave function (as in the rest of this section) and therefore omit phase information. The wave function starts in the ground state (see B.1 for details of the preparation), which is normalized to 1. At $t = 0\,\text{fs}$ it is excited by an XUV pulse defined in 2.4 a). The XUV ionizes parts of the wave function which results in a wave packet that moves away from the nucleus at the origin of the grid. The absorbing boundary, starting at $x = \pm 350\,\text{a.u.}$, damps the wave packet before it can reach the border of the grid. After 60 fs there is still a small contribution of the wave function in the continuum. This is due excitation with energies directly at the ionization edge and some minor reflections at the absorbing boundary. Additional to the continuum wave packet the XUV excites some bound states which can be seen at small distances from the nucleus. However, the majority of the wave function is not excited, but stays in the ground state.

For the orange lines in Figure 2.3 an additional Gaussian NIR pulse (see A.2) with

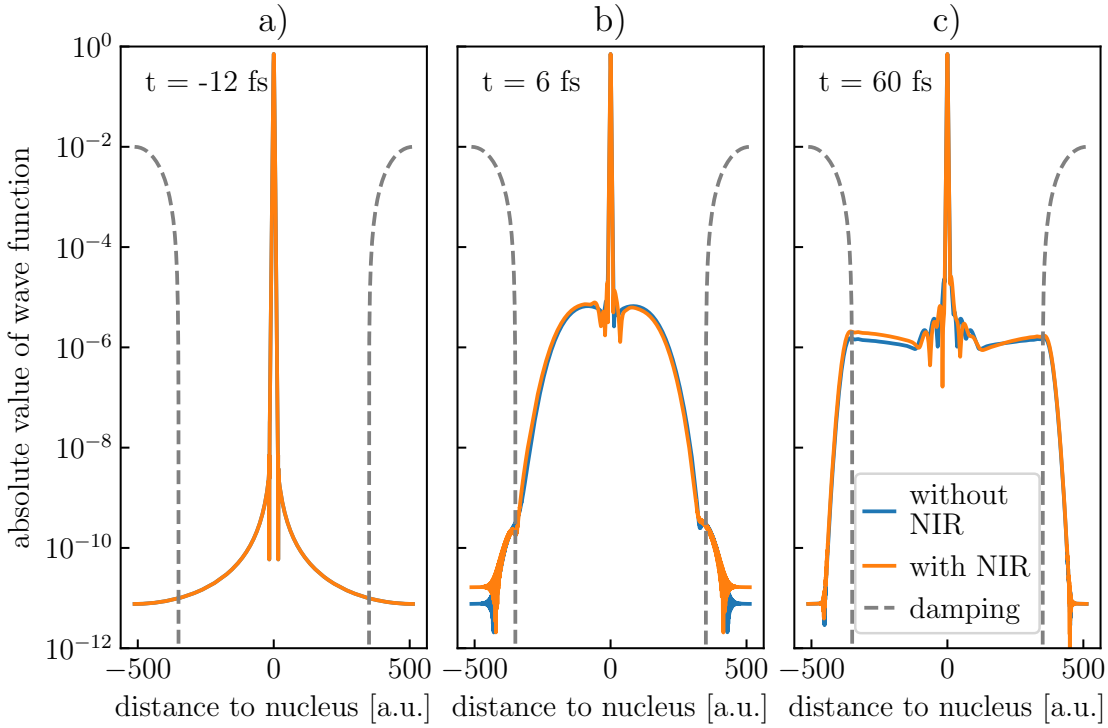

Figure 2.3: Evolution of a wave function
The absolute value of the wave function $|\Psi(x)|$ at different times with XUV excitation at t=0 and with (without) additional NIR interaction at t=0 in orange (blue). The gray dashed line indicates the absorbing boundaries.

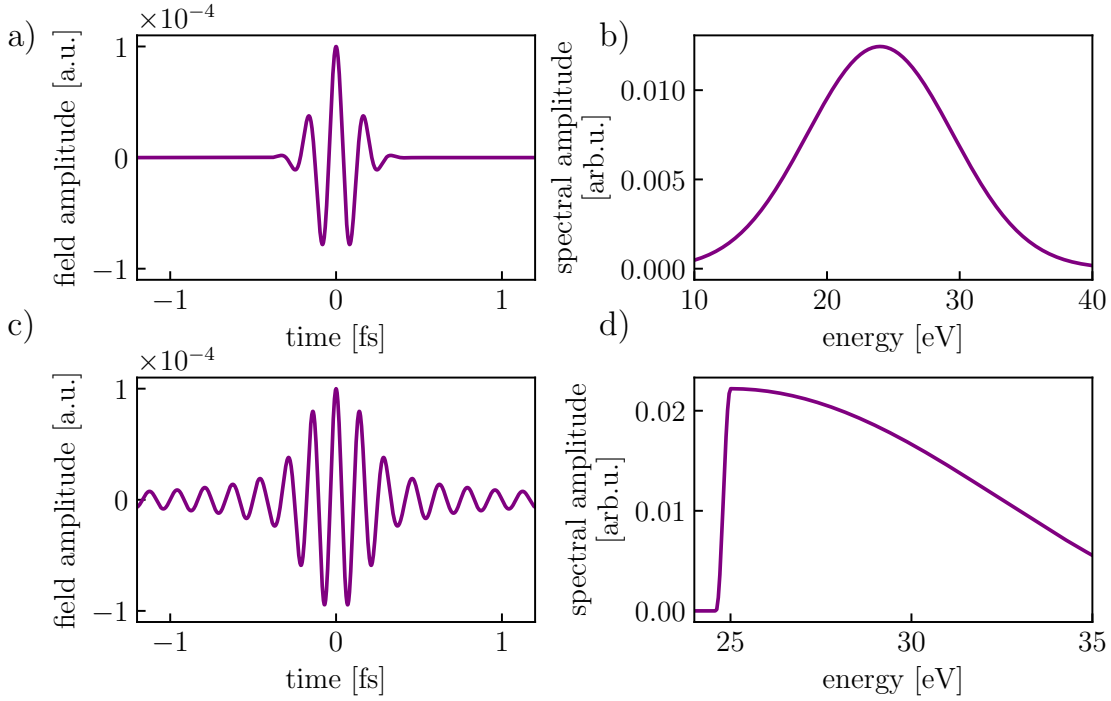

Figure 2.4: Spectra and time dependent field of XUV pulses
a), **b)** Gaussian pulse with $FWHM = 200\,\text{as}$ centered at $\omega_{\text{XUV}} = 24\,\text{eV}$ **c)**, **d)** XUV pulse defined in the spectrum by cos^2_{window} (see A.1) with maximum at 25 eV, a rising edge of 0.4 eV and a falling edge of 15 eV.

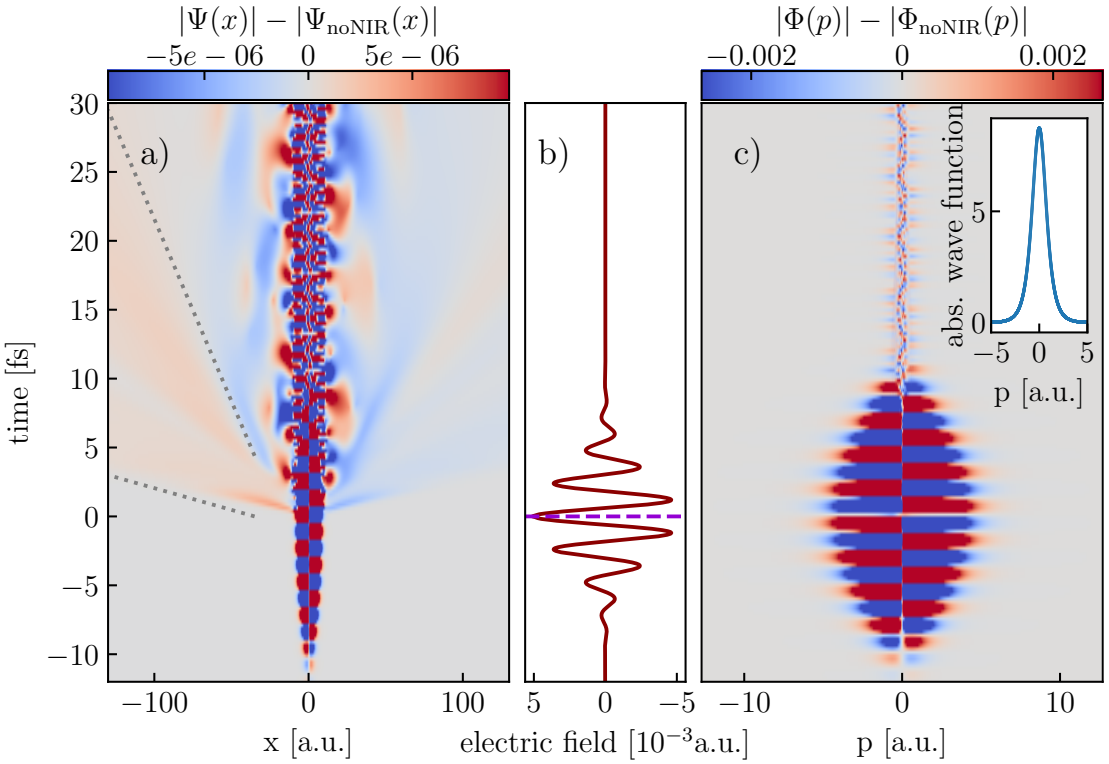

Figure 2.5: Influence of the NIR on the wave function evolution
a) Wave function evolution in real space, the color map displays the absolute value of the wave function with NIR interaction minus the wave function without NIR interaction. The gray dotted lines should highlight the ionized continuum wave packet. **b)** The electric field which acts on the wave function. The purple dashed line indicates the time of XUV excitation. **c)** Difference of the momentum wave function with and without NIR interaction. The inset shows the ground state in momentum space.

$FWHM = 5\,\mathrm{fs}$, central frequency $\omega_0 = 1.7\,\mathrm{eV}$ and peak intensity $I_{\mathrm{max}} = 0.9 \times 10^{12}\,\mathrm{Wcm}^{-2}$ perturbs the wave function with zero delay, thus at $t = 0$, as well. The NIR changes the excited bound states and introduces a small asymmetry in the continuum wave packet, i.e. the wave function has a higher amplitude in the negative x-direction than the positive x-direction.

To see the effect of the NIR pulse on the evolution of the wave function clearer, Figure 2.5 displays the difference between the wave function evolution with and without NIR interaction, thus $|\Psi(x,t)| - |\Psi_{\mathrm{noNIR}}(x,t)|$. Figure 2.5a) shows the wave function in real space. The NIR during the excitation leads to an asymmetric evolution of the continuum wave packet, i.e. the part of the wave function that departs in negative direction becomes bigger, the part in positive direction diminishes. The bound states (the part of the wave function which stays near the origin) are affected as well by the NIR pulse. During the interaction time (t=−10 fs to 10 fs) one can see a periodic shift of the ground state related to the phase of the electric field. It is possible as well, to look at the wave function in momentum space as shown in Figure 2.5c). In this representation the shift of the ground state dominates completely during the NIR interaction. Thus, the insight on dynamics in the continuum is limited.

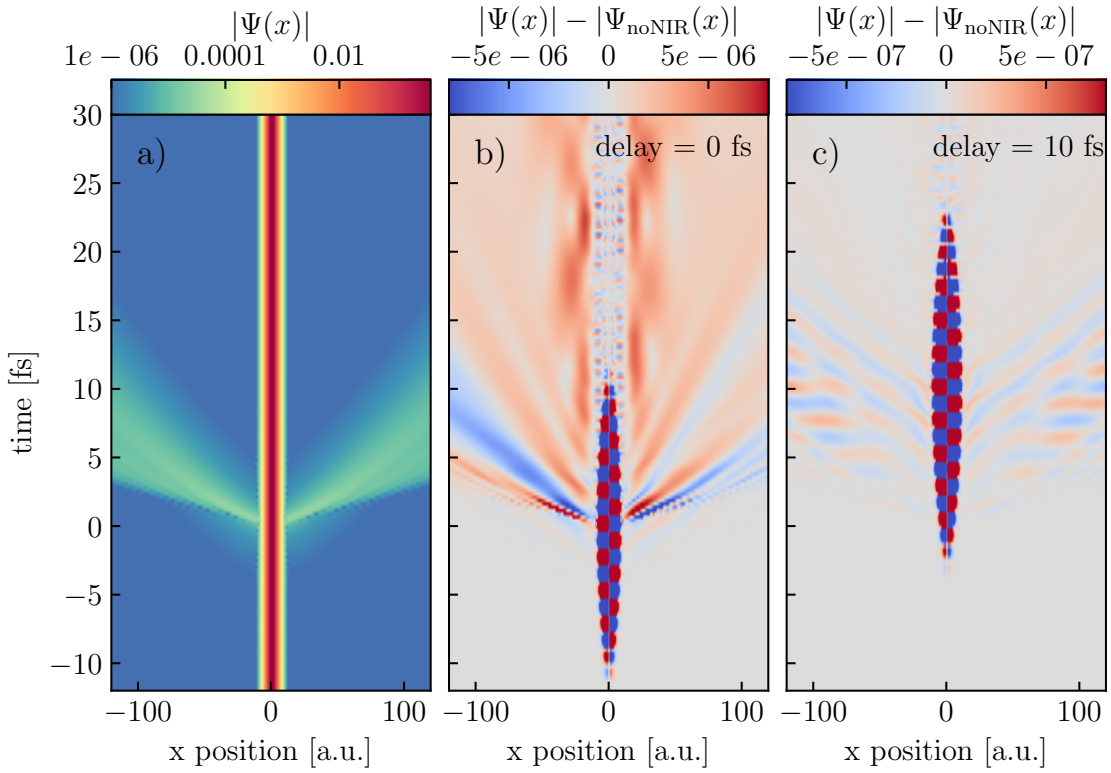

Figure 2.6: Wave function evolution with a spectrally asymmetric XUV pulse with NIR interaction at different delays
a) Evolution of the wave function with XUV excitation with the pulse from 2.4c) at $t = 0$. **b)**, **c)** Changes of the wave function due to an NIR pulse at $t = 0\,\mathrm{fs}$, $t = 10\,\mathrm{fs}$. Note the different scale in c)

To sum up, in this configuration the XUV excites continuum and bound states and both are changed (coupled) by the NIR interaction. In this work the influence of a strong NIR field on the continuum is studied. Therefore, it would be nice to separate bound and unbound states and excite only the latter.

2.2.2 Excitation of Continuum States Only

An excitation of the continuum states only can be achieved by tailoring the XUV pulse in the present simulation. Figures 2.4 c) and d) show the XUV pulse which is used in the following. This pulse only contains spectral components above 24.6 eV and below 40 eV, thus it cannot excite bound states. As downside it is less well defined in the time domain. With $FWHM \approx 500\,\mathrm{as}$ it is longer than the Gaussian pulse used before and it shows long-lasting ringing.

Figure 2.6a) shows the time evolution of a wave function which was excited by this pulse in logarithmic scale. There is a wave packet that separates from the ground state at $t = 0\,\mathrm{fs}$ and moves towards the boundaries while it is dispersing. However, next to the origin no changes are visible because no bounds states have been excited. This is exactly the behavior we wanted to achieve. Figures 2.6 b) and c) depict the change in wave function by the NIR interaction. The pulse parameters are the same as before, only

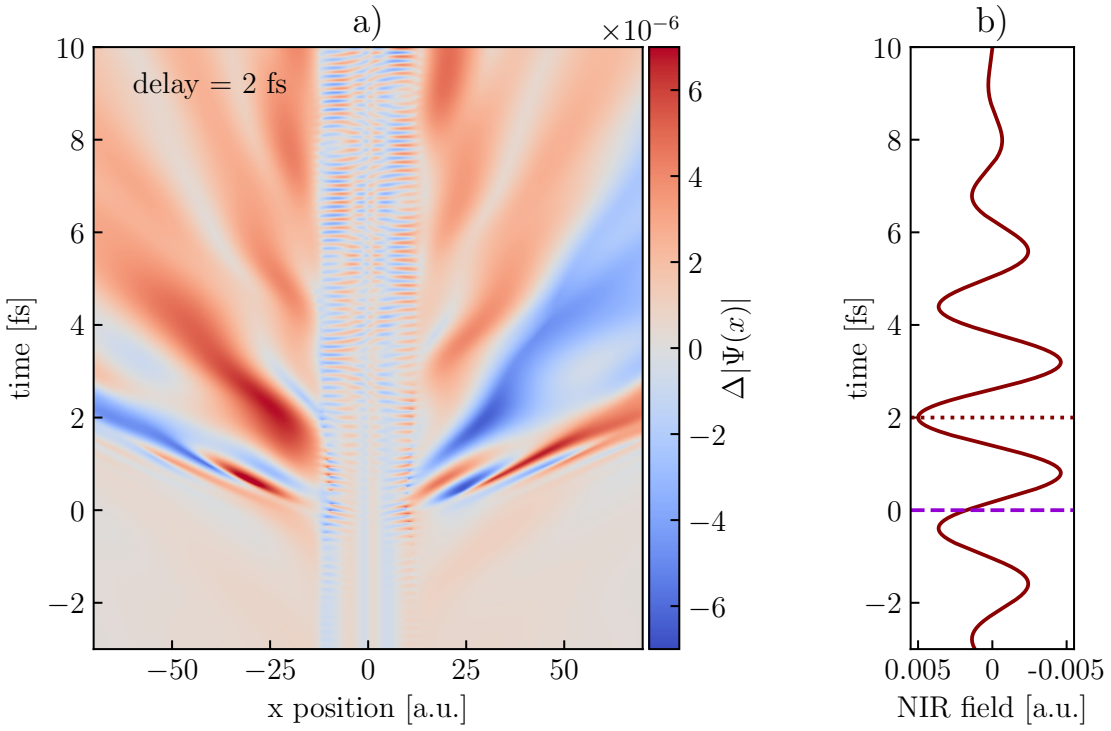

Figure 2.7: NIR and XUV induced changes of the wave function evolution
a) Changes of the wave function evolution with spectrally asymmetric XUV excitation with NIR interaction at $t = 2\,\text{fs}$. The plotted quantity is $\Delta\Psi(x)$ defined in equation (2.12). **b)** The NIR field which acts on the wave function. The dashed line indicates the time of XUV excitation, the dotted line is the time of maximal NIR field.

the time delay between NIR and XUV is changed. If the pulses are overlapping (delay 0 fs), the NIR modulates the continuum wave packet in a manner that it is alternating enhanced in positive and negative direction and the opposite direction is suppressed. In addition, bound states are populated. These are higher lying Rydberg states, which can be reached out of the continuum with one or two NIR photons. For a delay of 10 fs, the NIR has nearly no effect on the wave function, except for a very small modulation of the continuum wave packet (the color map is one magnitude more sensitive than for time delay of 0 fs). Hardly any bound states are excited after both pulses have passed.

It is an interesting question whether one can see parts of the continuum wave packet pushed back to the nucleus by the NIR field. This could be interpreted as 'recollision' of an ionized electron into the atomic core. The most interesting region to look for such a signature is close to the nucleus, but there the periodic shift of the ground state dominates the change of the wave function and potentially overlays the signature. Fortunately, it is possible to subtract this dominant contribution, as it is done in Figure 2.7. Here we see the remaining wave function after the subtraction of the the changes that the NIR introduces without XUV, the changes the XUV introduces without NIR and the ground state $\Psi_0(x)$:

$$\Delta\Psi(x) = |\Psi(x)| - (|\Psi_{noNIR}(x)| - |\Psi_0(x)|) - (|\Psi_{noXUV}(x)| - |\Psi_0(x)|) - |\Psi_0(x)| \quad (2.11)$$

$$= |\Psi(x)| - |\Psi_{noNIR}(x)| - |\Psi_{noXUV}(x)| + |\Psi_0(x)|. \quad (2.12)$$

In Figure 2.7 the time delay is set to 2 fs to follow the thinking that a wave packet is first excited, then propagates and is finally pushed back. Of course the NIR pulse is already present during the excitation due to its FWHM of 5 fs. The figure shows the induced asymmetry in the continuum wave packet clearly and one can see the population of the excited bound states. Some structures around $x = \pm 20$ a.u. look a bit bent, but there is no feature that would allow for an interpretation of 'recollision' in the classical sense, i.e. an electron trajectory returning to the nucleus.

This section gave an idea of the evolution of the electron wave function with XUV excitation and interaction with a moderate strong NIR pulse in the used model. Experimentally, the time dependent electron wave function is not measurable directly. To produce predictions comparable to experiments, we need to look at another quantity, the absorption spectrum.

2.3 Calculation of Spectra without Strong Fields

This section shows first how to calculate a spectrum from the wave function evolution. Then, the unperturbed spectrum (no strong NIR interaction) dependence on damping and grid size is studied.

By knowing the wave function at each moment in time, one can calculate the time dependent dipole moment, which is a quantum mechanical observable:

$$d(t) = \langle \Psi(t) | x | \Psi(t) \rangle \,. \tag{2.13}$$

To make the results comparable to measured data, we have to introduce an effective decay of the dipole moment. This accounts for dephasing, spontaneous decay and finite spectrometer resolution, which define an effective time scale for the dipole decay in the experiment [23]. As shown in Figure 2.8 the dipole is multiplied with an exponential function with lifetime τ

$$\tilde{d}(t) = e^{-t/\tau} d(t). \tag{2.14}$$

τ is set to be 100 fs, which will transform delta-like absorption lines into Lorentzians with a width in the order of meV. This is much longer than the time scale of any effect we want to study. Equation (1.23) states, that with the electric field of the XUV $\mathcal{E}(t)$ the absorption $A(\omega)$ is calculated by:

$$A(\omega) \propto \omega \Im \left[\frac{\mathcal{F}(\tilde{d}(t))}{\mathcal{F}(\mathcal{E}(t))} \right]. \tag{2.15}$$

In the simulation the speed of light c is used as proportionality constant (according to [24] the cross section is then $\sigma(\omega) = \frac{4\pi}{c^2} A(\omega)$). Figure 2.9 displays the resulting absorption spectrum. The bound states dominate by several orders of magnitude. In contrast to experimental absorption spectra the ionization edge is only a small bump. Additionally, there seem to be bound states after the continuum edge because of the finite grid size.

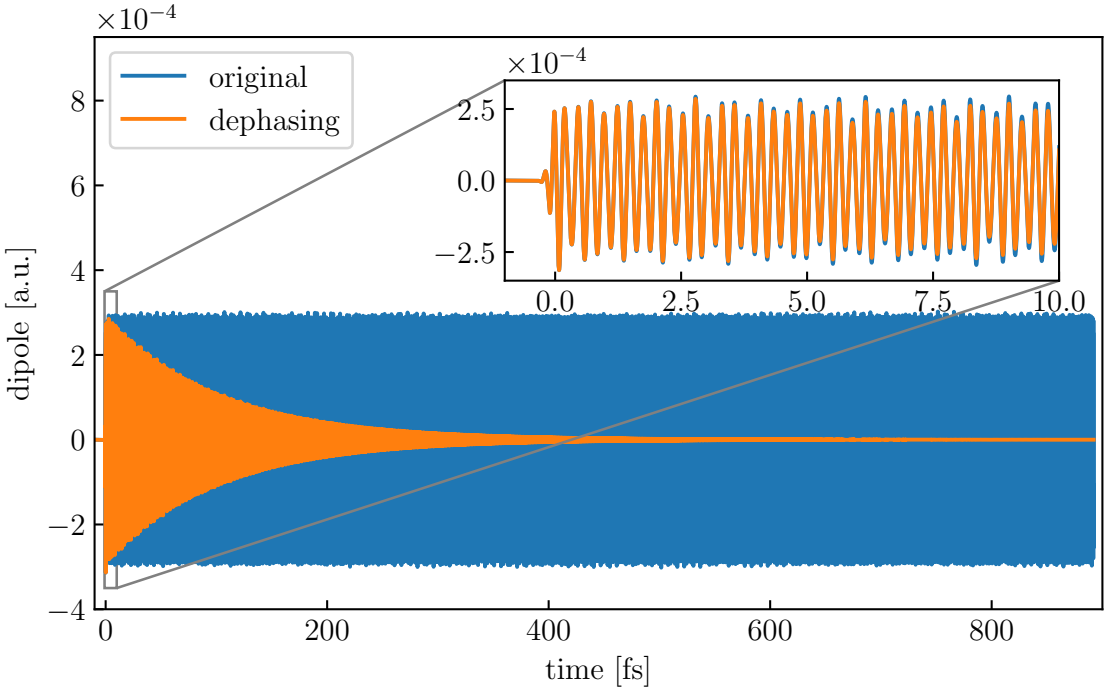

Figure 2.8: Dipole moment out of the TDSE simulation with only an XUV excitation
The dipole moment, calculated by (2.13), without (with) additional dephasing in blue (orange). The inset shows a zoom-in to illustrate the oscillation. The XUV excitation pulse is given in 2.4a).

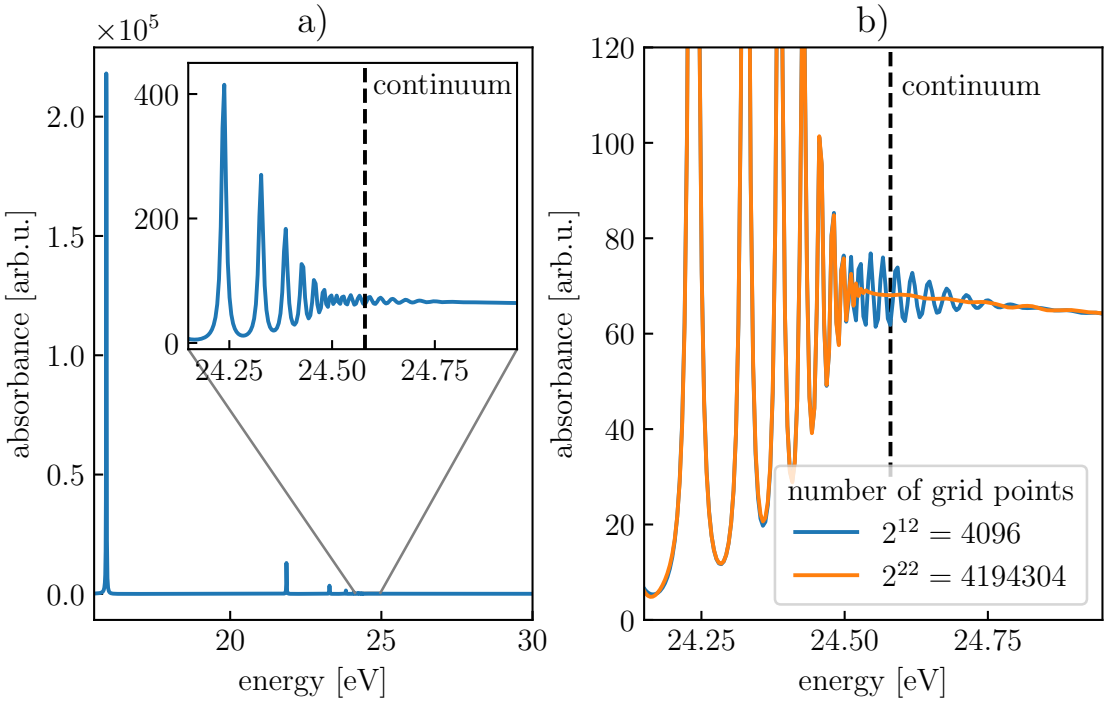

Figure 2.9: Spectrum out of the TDSE simulation with only an XUV excitation
a) The spectrum that calculates by (2.15) out of the dipole in Figure 2.8. The inset shows a zoom-in on the continuum edge, where the dashed line represents I_p. Calculations are in length gauge. **b)** Further zoom-in on the continuum edge, calculated with two different grid sizes.

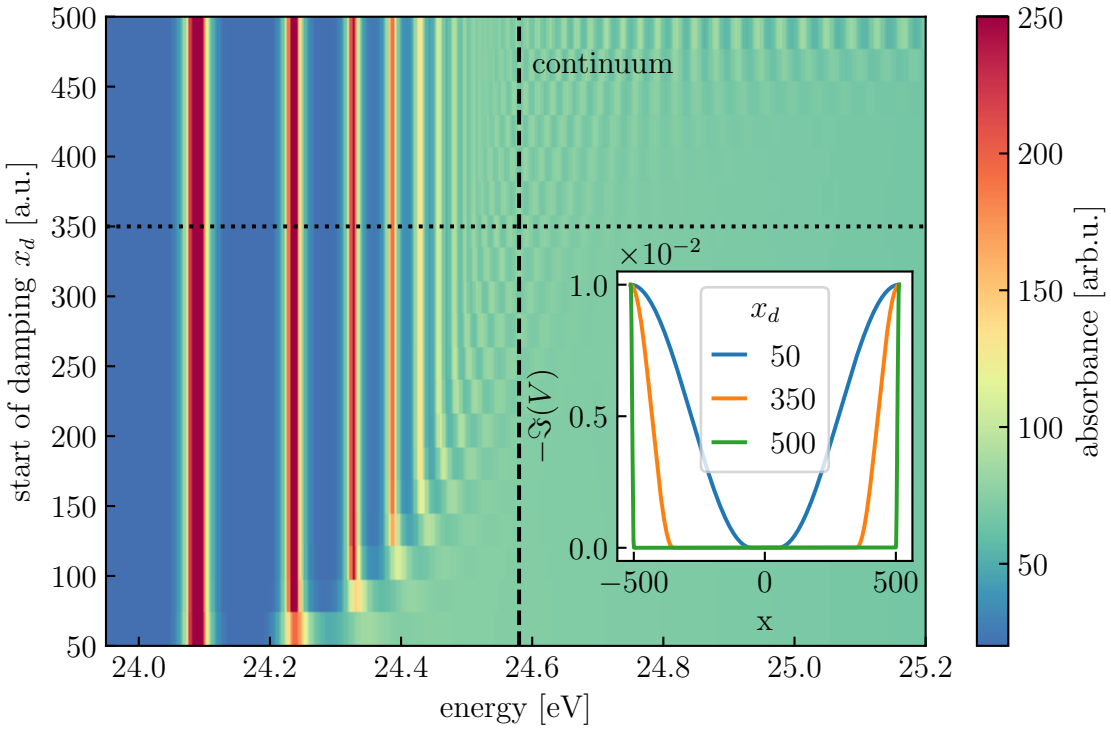

Figure 2.10: Spectrum out of the TDSE simulation for different absorbing boundaries The absorption spectrum without NIR for different start values of the absorbing boundaries. The dashed line indicates the ionization potential I_p and the dotted line depicts the damping parameter which is used for all other simulations within this chapter. The inset shows three lineouts of the absorbing boundaries for different start values x_d.

Within this work the simulation was rewritten to be run on GPUs. For a grid size of 4096 points GPU computing is slower than on CPU with an average laptop. For big grids the GPU computing unleashes its scaling power, thus the simulation could be run with more than four million grid points (this was only by a factor of 20 slower than the 4096 points on CPU). One can see in 2.9b) that the oscillations around the continuum edge disappear for this big grid. However, out of time and power consumption arguments all further calculations are conducted on the smaller grid as these features do not encumber the findings.

It is important to check the influence of the absorbing boundaries, as their impact is biggest on continuum states which we are mainly interested in. Figure 2.10 shows the absorption spectrum dependent on the size of the boundaries. If the damping starts too close to the nucleus, the absorption lines of the Rydberg states get broader and shift a bit to higher energies. If the damping starts too close to the grid borders, the artifact of the discrete states above the continuum threshold due to the finite grid size becomes stronger. As a compromise for all further calculations the start of the absorbing boundaries is set to 350 a.u.

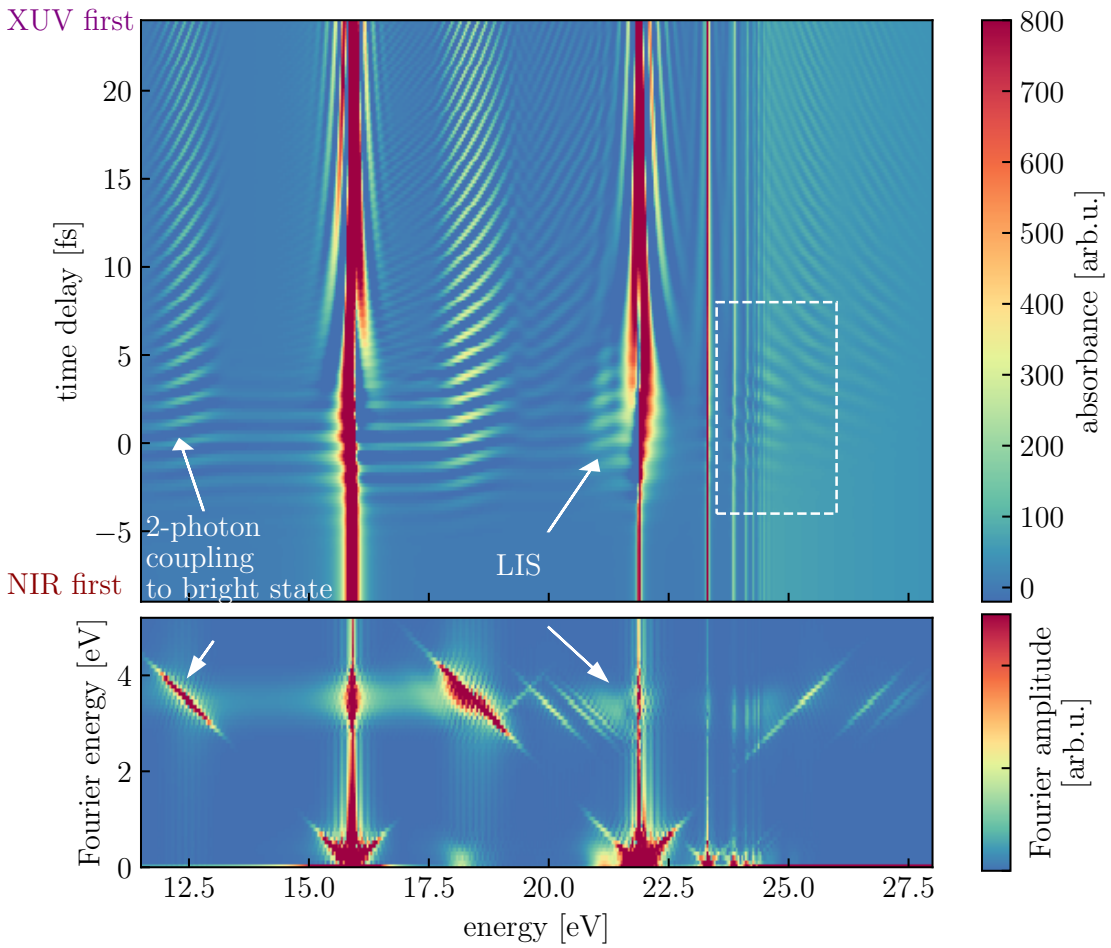

Figure 2.11: Time delay scan of the absorption spectrum with the TDSE simulation On the top, for each time delay of the NIR and XUV pulse (parameters in the text), the absorption spectrum was calculated. The white dashed box marks an interesting region at the continuum edge. The bottom part of the figure displays the same data as above, Fourier transformed along the time delay axis. The absolute value of this Fourier transform is indicated by the color scale.

2.4 Time Delay Dependent Absorption Spectra

In this section the time delay dependent influence of a strong NIR pulse on the absorption spectrum is studied.

For the simulations in this section, the NIR and XUV parameters are the same as in the previous sections (XUV: Gaussian with $FWHM = 200\,\text{as}$ centered at $\omega_{\text{XUV}} = 24\,\text{eV}$; NIR: Gaussian with $FWHM = 5\,\text{fs}$, central frequency $\omega_0 = 1.7\,\text{eV}$, maximum intensity $I_{\text{max}} = 0.9 \times 10^{12}\,\text{Wcm}^{-2}$). These are comparable to values which can be reached experimentally.

Figure 2.11 shows the time dependent absorption spectrum and its Fourier transform over the delay axis. At negative time delays, when the NIR comes before the XUV, the spectrum does not change. However, during the overlap and for NIR pulses succeeding the XUV, there is a lot of dynamics visible. Many visible effects have already been studied in various publications [24–26], which emphasize NIR-induced dynamics between bound states. For many states the absorption line shape changes by Autler-Townes splitting

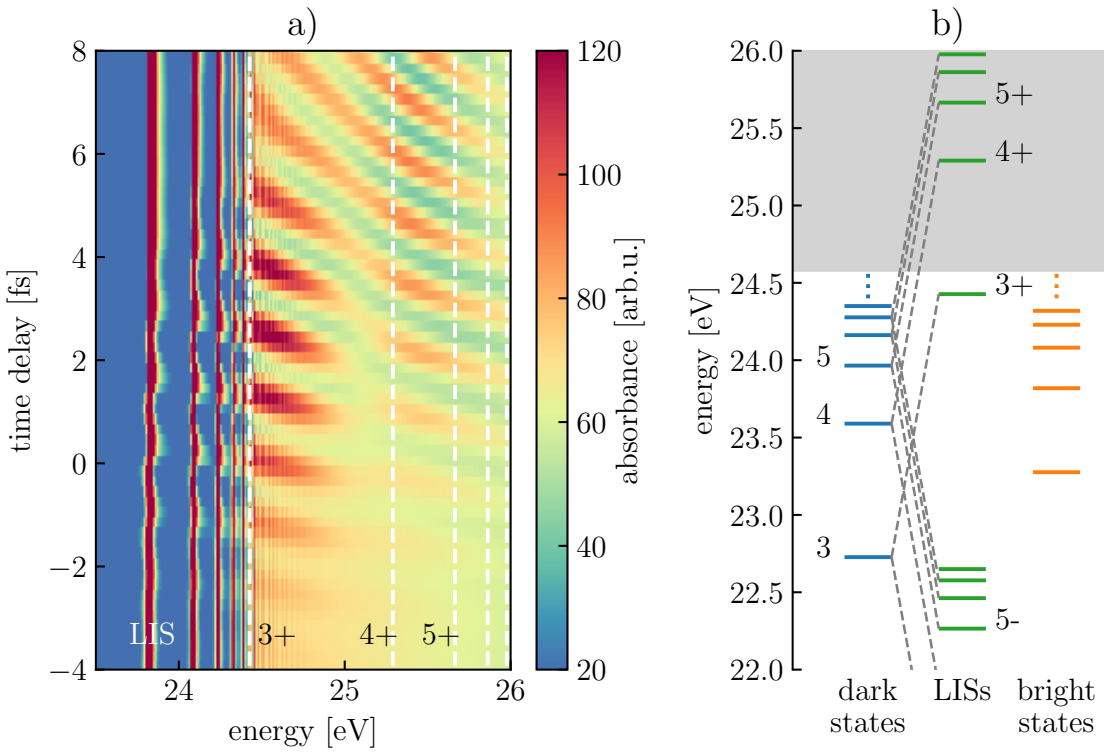

Figure 2.12: Absorption spectra continuum structure
a) Magnification of the time dependent absorption spectra in the dashed box of Figure 2.11. The white dashed lines indicate the energy position of the light induces states (LISs) without ponderomotive shifts. **b)** Level scheme of the model system at the continuum edge with dark, bright and light induced states for an NIR energy of 1.7 eV. The gray area indicates the continuum. See text for details on the states labeling.

during the overlap [27] and by perturbed free induction decay for positive delays [28]. The sub-cycle oscillations of the absorbance which produce the most dominant diagonal features in the Fourier spectrum are due to two photon coupling to the bright states [25, 26, 29]. Additionally, there are light induces states (LISs), which couple the ground state to dipole forbidden dark states with an XUV and an NIR photon [23, 25]. They are only present in the direct overlap of NIR and XUV light at $\omega_{\mathrm{LIS}} = \omega_{\mathrm{darkstate}} \pm \omega_{\mathrm{NIR}}$.

As this work concentrates on laser-induced continuum dynamics, we look for interesting features in that regime. In Figure 2.11 the dashed white box highlights a region at the continuum edge, where one can see a slight total enhancement in absorption during pulse overlap. The most probable explanation for this is either a light-induced state or a direct response of the continuum edge.

2.5 Light Induced States in the Continuum

The aim is to solve the ambiguous interpretation of the absorption enhancement at the continuum threshold of the last section. Therefore, Figure 2.12 a) shows a magnification of the continuum edge absorption spectra together with the position of the expected LISs. The numbers inside the plots indicate the order of the dark state (1 stands for the ground

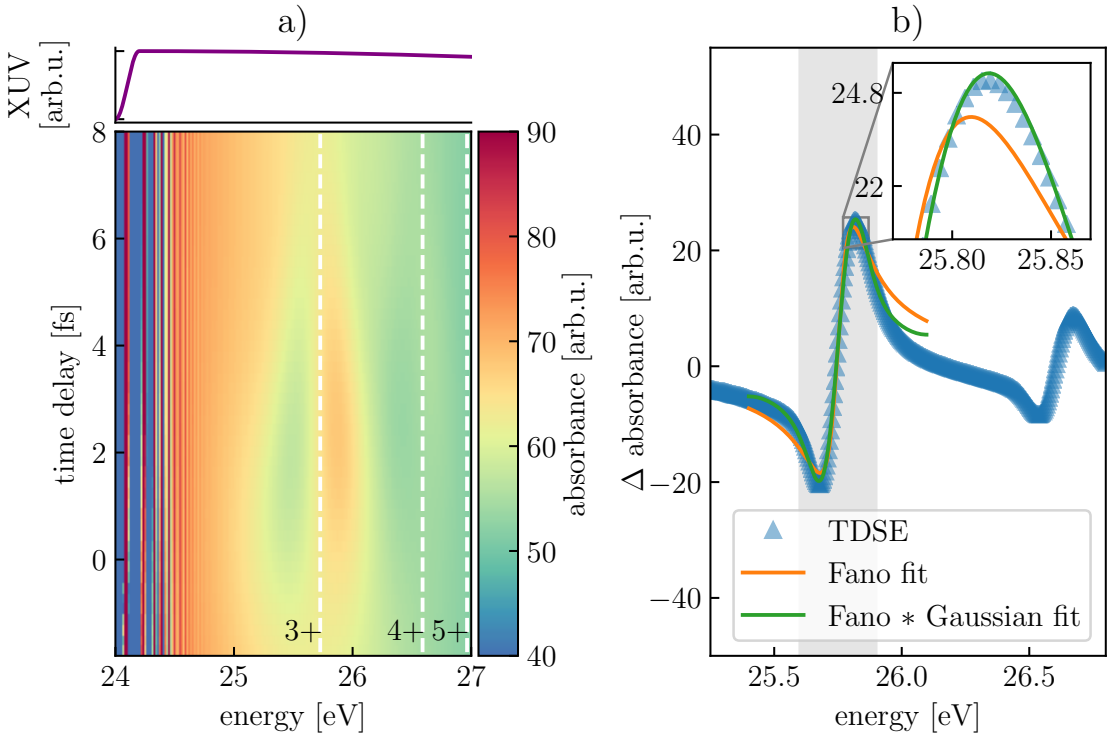

Figure 2.13: Laser induced continuum structure
a) Time-dependent absorption spectra at the continuum threshold for an asymmetric XUV excitation (spectrum shown at the top) and a strong field with central frequency $\omega_0 = 3\,\text{eV}$, pulse duration $FWHM = 5\,\text{fs}$ and peak intensity $I_{\text{max}} = 8.1 \times 10^{-5}\,\text{a.u.} = 2.8 \times 10^{12}\,\text{Wcm}^{-2}$. The white dashed lines indicate the energies of the LISs. **b)** The field induced difference of the absorption $A(\omega) - A(\omega)_{\text{nofield}}$ for a time delay of 2.6 fs of a strong pulse with the same parameters as in a) except for $FWHM = 20\,\text{fs}$. The solid orange (green) line represents a fit with the Fano formula (2.16) (Fano convolved with a Gaussian with $\sigma = 54.8\,\text{meV}$). Fit parameters are given in the text. The gray region indicates the fit region and the inset shows a zoom-in.

state) and the + implies that the LIS is one NIR photon energy higher than the dark state. Figure 2.12 b) shows the labeling on a level scheme of the simulation. There are LISs energetically lower than their dark state, they are signed with a minus, eg. 3-, 4-. As the central frequency of the NIR is $\omega_0 = 1.7\,\text{eV}$, the 3+ LIS lies at 22.73 eV (energy of 3rd dark state) $+1.7\,\text{eV} = 24.43\,\text{eV}$, which is very close to the ionization potential of 24.58 eV. At LISs 4+ and 5+ there is no distinct feature in the pulse overlap, because of a much smaller coupling strength. Thus, there is a light-induced state at the continuum edge, but we can still not be certain, that this is the reason for all of the modulation of the absorption visible at the ionization threshold in the spectrum.

To clarify this, Figure 2.13 a) shows the time dependent absorption spectra for a slightly different case. Compared to the previous settings, the XUV pulse is now not Gaussian but asymmetric in the spectral domain. It has the same shape as in 2.4 d) but starts at 24 eV and peaks at 24.2 eV (compare the lineout in the top of the figure). As a consequence the overall $2\,\omega_0$ oscillation of the absorbance vs time delay disappears for the following reasons. Firstly, the continuum cannot interfere with the bright states plus two

NIR photons, as the bright states are not populated any more. Secondly, the XUV cannot excite the light-induced states which lie energetically below the corresponding dark state, e.g. the 3-. Thus, the 3- and the 3+ states cannot interfere but this interference would be responsible for the periodic modulation of the absorbance with time delay at the LISs [25]. Consequently, all sub-cycle structure has disappeared from the absorption spectra. Another important change in the settings is the central light frequency of the strong pulse, which corresponds to 3 eV in Figure 2.13 a). This change shifts the 3+ LIS away from the ionization potential (LIS 2+ is at 23 eV, thus it will not effect the continuum edge either). The intensity of the light has been adjusted to keep the ponderomotive energy the same as for the NIR light at 1.7 eV. This was done, because the continuum structure can be explained by a ponderomotive shift of the free electrons to some extend (see [17]). Mainly two things can be learned from Figure 2.13 a).

- There is no time-delay dependent feature at the continuum edge. The absorption is exactly the same for all time delays, thus the modulation in the former case must have been caused by LIS 3+.
- Without the $2\,\omega_0$ periodicity the shape of the LIS absorption profile becomes clearly visible. In the pulse overlap, the absorption decreases first and increases afterwards in the energy domain.

The feature of LIS 3+ is spectrally broad as the light pulse is short and broad in the spectrum. To prevent a mixture of the 3+ and 4+ LISs, the pulse width is increased to $FWHM = 20\,\text{fs}$. Figure 2.13 b) shows the absorption at 2.6 fs minus the absorption without a strong field. The energy range in the figure covers the 3+ and the 4+ LISs. Both light-induced states have a similar spectral line shape, which is very much Fano like.

Fano explained the absorption line shape of autoionizing doubly excited helium states [30] which is due to the interference between two quantum pathways leading to ionization. According to Fano the change in absorption ΔA due to the resonance is:

$$\Delta A_{\text{Fano}}(E) = A_0 \left(\frac{(q+\epsilon)^2}{1+\epsilon^2} - 1 \right), \tag{2.16}$$

$$\epsilon = \frac{E - E_0}{\Gamma/2}, \tag{2.17}$$

where ϵ stands for the reduced energy, A_0 for the absorption far away from the resonance, E_0 for the position of the resonance and Γ for its width. q is the asymmetry parameter introduced by Fano. Additionally, Lorentzian absorption lines can be converted to show a Fano profile by inducing a phase onto the dipole response by a strong laser pulse [31]. How can we understand the origin of the Fano absorption line in the present case?

The phenomenon which leads to the observed absorption features is known as Laser-Induced Continuum Structure (LICS). It has already been described in the 70s [32] as 'pseudo-autoionizing states' and studied on several systems by sweeping a narrowband laser through the resonance [33–35]. Reference [36] offers a review of this topic. The process is the following: an embedding laser couples an unpopulated discrete bound state with the continuum. Simultaneously, a weak probe laser examines the absorption in the

structured continuum. This is exactly the situation given in the attosecond transient absorption experiment with a strong light field in the temporal overlap. In analogy to autoionizing states [36], where a bound state is embedded in the continuum, the LICS has a Fano profile.

Fitting the simulated absorption spectrum of Figure 2.13 b) with the Fano profile given by equation (2.16) results in the parameters:

$$\Gamma = 0.13\,\text{eV} \qquad q = 1.14 \qquad E_0 = 25.753\,\text{eV} \qquad A_0 = 18.4\,\text{arb.u.}$$

However, the Fano fit seems to describe the absorption profile poorly. This can be explained by the broad spectrum of the strong embedding laser. For the used 20 fs pulse,the spectrum has a width of $\sigma = 54.8\,\text{meV}$ and the position of the resonance has a width as well. To take this effect into account the fitted Fano profile is convolved with a Gaussian of width σ. As the width is fixed, the fit has no additional free parameter, but Figure 2.13 b) shows a nearly perfect agreement with the simulation data. The new fit parameters are:

$$\Gamma = 0.20\,\text{meV} \qquad q = 1.20 \qquad E_0 = 25.756\,\text{eV} \qquad A_0^* = 6700\,\text{arb.u.}$$

A_0^* is not the absorption far away from the resonance but a scaling factor which describes the strength of the resonance. It can be expected, that this method will not accurately describe the absorption spectra for very high laser intensities, because at some intensity the photon picture describing the emergence of the LISs/LICS should break down.

Let's have a look at the intensity dependence of the LICS in the moderate intensity regime, where the ponderomotive shift is still smaller than the laser bandwidth and central energy. Figure 2.14 a) shows the absorption changes at the 3+ LIS for different intensities together with Fano $*$ Gaussian fits. Figure 2.14 b) depicts the central photon energy of the resonance and its q values as they have been found by fits versus laser intensity. The position of the resonance shifts linear with the intensity, which makes sense as the ponderomotive energy scales linear with intensity. Fitting the positions linearly gives us a zero intensity value, which is in very good agreement with the theoretical prediction (energy of the third dark state plus the central photon energy) indicated with a black diamond. The q value shows a small systematic dependence on the laser intensity as well as it decreases with maximum intensity. This could be a hint on phase shifts which are introduced by the laser [31]. However, the standard deviation of the fit errors are much larger than the changes. [1]

2.6 Interpretation of LICS in the Time Domain

Following the reasoning of Section 1.9, it is possible to reconstruct the time dependent dipole moment out of an absorption spectrum. Thereby, it is crucial which part of the

[1] One has to keep in mind as well, that simulated numbers do not show noise as experimental data. Thus, the standard deviations of the fit parameters are due to systematic errors.

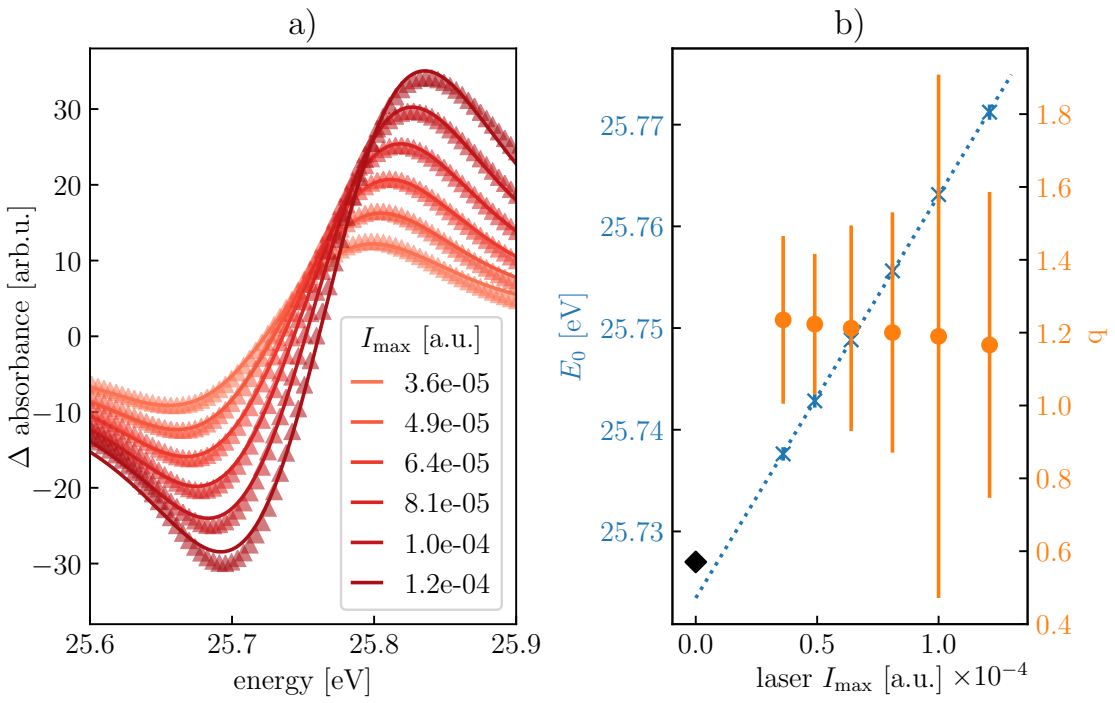

Figure 2.14: Intensity dependence of the laser induced continuum structure
a) Field induced changes of the absorption spectrum at the 3+ LIS for the same pulse configuration as in Figure 2.13 b) for different laser intensities. The markers show the simulation results, the solid lines are fits to a Fano line convolved with a Gaussian with $\sigma = 54.8\,\text{meV}$ width. All fit parameters are in appendix B.4. **b)** Blue crosses show the center energy of the fits (σ error bars have the size of the markers) dependent on the peak laser intensity. Orange circles mark the fitted q parameter with fit σ error bars. The dotted line is a linear fit to the center energies. The black diamond marks the position of the 3+ LIS without ponderomotive shift.

absorption spectrum is chosen by a window function.

Figure 2.15 shows the reconstructed dipole for two choices. 2.15 a) and b) use a Gaussian window to concentrate on the 3+ LIS and 2.15 c) and d) take an asymmetric cos^2_{window} function, like it is defined in Appendix A.1 starting at 24.3 eV rising for 0.3 eV and falling for 12 eV. The upper panel which is based on the use of a Gaussion window does offer a clear interpretation. Without a strong field the dipole moment decays rapidly, as the atom is ionized quickly. If there is an additional strong field, the continuum wave packet is coupled to the dark 3-state and the dipole moment can survive longer without ionization. This effect is known as population trapping and has been studied together with LICS [35]. The small oscillation, which is visible for the pulse with $FWHM = 20\,\text{fs}$ at a period of 4.8 fs, corresponds to the energy difference between the 3+ and 4+ states, as the window does not cut out the 3+ state perfectly. The dipole response of the full continuum in the lower panel is harder to interpret. Even without a field the dipole decays slower, as the part of the wave function which has an energy directly at the continuum threshold does not ionize fast. The field induces oscillations in the dipole response which are due to all LISs in the continuum and the modulations directly at the ionization potential.

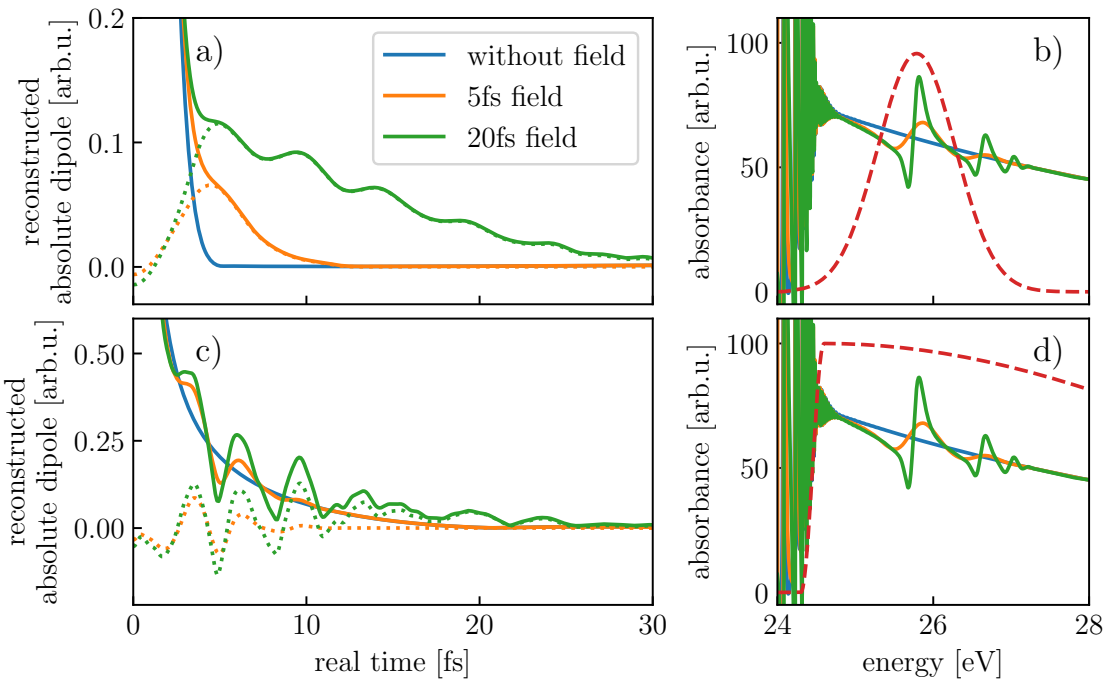

Figure 2.15: Reconstructed dipole response of LICS
a) (c) The absolute value of the reconstructed dipole moment for different field lengths (in *FWHM*). The dotted lines show the value of the reconstructed dipole minus the dipole without a strong field (blue). **b) (d)** The absorption spectra of the 3+ LIS for the different pulse parameters and the window function (red dashed), which was used to retrieve a) (c). The pulse parameters are the same as in Figure 2.13 at a delay of 2.6 fs.

2.7 Absorption Signatures for High Intensities

In the previous sections, we have looked at intensities smaller than $5 \times 10^{12}\,\mathrm{W/cm^2}$. Now, Figure 2.16 shows the delay dependent absorption in the continuum for an intensity of $3.2 \times 10^{13}\,\mathrm{W/cm^2}$ using light with $\omega_0 = 3\,\mathrm{eV}$. This corresponds to a ponderomotive energy of 500 meV. The asymmetric shape of the excitation XUV pulse ensures that there are no couplings to LISs or bright states which are bound. The LISs 3+ and 4+ are clearly visible and ponderomotively shifted. Additionally, there is a clear absorption feature directly at the continuum edge, whose origin cannot be explained by LISs. In the temporal overlap of the two pulses the absorption at 24.6 eV is strongly enhanced and at 25.2 eV there is a slight decrease of the absorption for a delay of 3 fs. For even longer time delays a hyperbolic structure becomes visible at the continuum edge. This is either due to perturbed free induction decay of the Rydberg states or caused by the ponderomotive shift of the free electrons [17]. An exact discrimination does not make sense, as for this intensity the ponderomotive energy is much higher than the binding energies of Rydberg states. Thus, electrons occupying Rydberg states are hardly distinguishable from free electrons. The feature in the pulse overlap is harder to interpret. It might be seen as an absorption signal from the Rydberg states which are pushed into the continuum by the ponderomotive energy. However, at this intensity the transition from Rydberg to continuum states is smooth as the electrons are not bound anyway.

There is a small $2\,\omega_0$ oscillation on all features in the temporal overlap. For the light induces states, this can be explained by 2 photon couplings to the 3^{3+} and 4^{3+} states (which are three photons away from the dark state). The oscillation in the Rydberg states and at the edge is either an intrinsic property of the continuum feature or an artifact of the simulation. As the intensity is very high, some small part of the wave function is reflected at the absorbing boundary leading to an oscillation for equal Fourier and spectral energies. This is filtered out in Figure 2.16 but there might be more artifacts due to this numerical issue.

It is interesting to look at the wave function evolution for the case of a strong field. Figure 2.17 b) shows the identical case as Figure 2.7 but with a 50 times higher intensity, which corresponds to a ponderomotive energy of $U_p = 2.1\,\mathrm{eV}$. Here, $U_p \approx \omega_0$, such that even stronger effects can be expected than for Figure 2.16 with $\omega_0 = 3\,\mathrm{eV}$ ($U_p = 0.5\,\mathrm{eV}$). The wave function is now strongly driven by the field and there are contributions which are pushed back to the nucleus. This wavy motion of the wave function is very similar to the trajectories, which electrons would follow in a classical sense. To illustrate this statement, the trajectories for two different starting parameters (see figure caption) are shown. One is calculated using the strong-field approximation (SFA), i.e. neglecting the atomic potential, and one corresponds to the classical motion with the soft-core potential. The absorption spectrum displayed in 2.17 d) shows very strong dynamics which cannot be explained in the picture of LISs. Applying the reconstruction of the dipole moment (1.9) results in Figure 2.17 a). At first look the reconstructed absolute dipole moment seems to be asystematic but the maxima of the curve fit very well to the times which can be interpreted as zero-crossings of the wave function evolution.

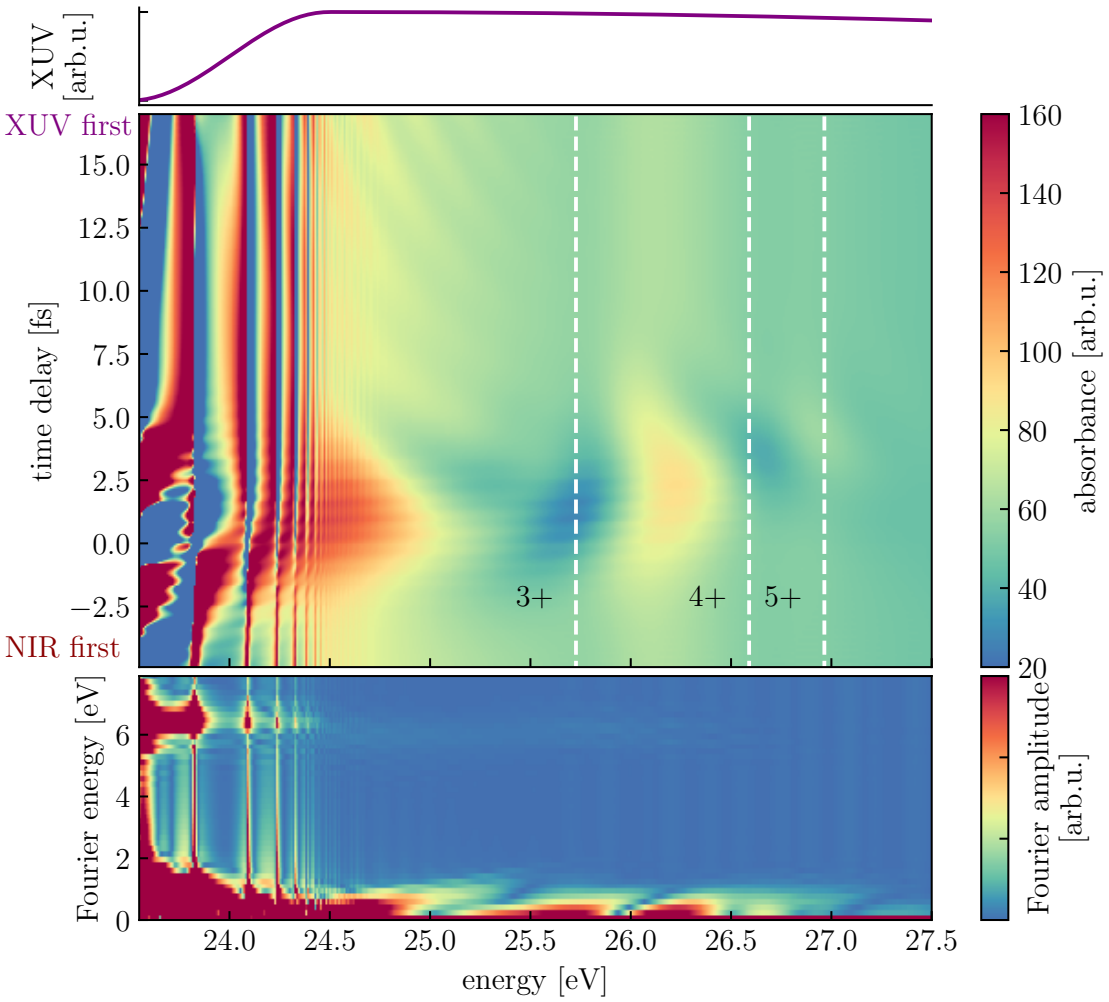

Figure 2.16: Absorption spectrum at high intensity
Absorption spectra dependent on the time delay at the continuum edge (in the middle) and the corresponding Fourier transform along the delay axis (in the bottom). The pulse parameters are the following. XUV: asymmetric with 1 eV rising edge, maximum at $\omega_{\mathrm{XUV}} = 24.5\,\mathrm{eV}$ and 15 eV falling edge; VIS: Gaussian with $FWHM = 5\,\mathrm{fs}$, central frequency $\omega_0 = 3\,\mathrm{eV}$, maximum intensity $I_{\mathrm{max}} = 3.2 \times 10^{13}\,\mathrm{Wcm}^{-2}$. The XUV spectrum is plotted in the top. The white dashed lines indicate the positions of the LISs, without the ponderomotive shift. To get rid of an artifact due to reflection on the boundaries, the data is lowpass filtered at 15 eV Fourier energy.

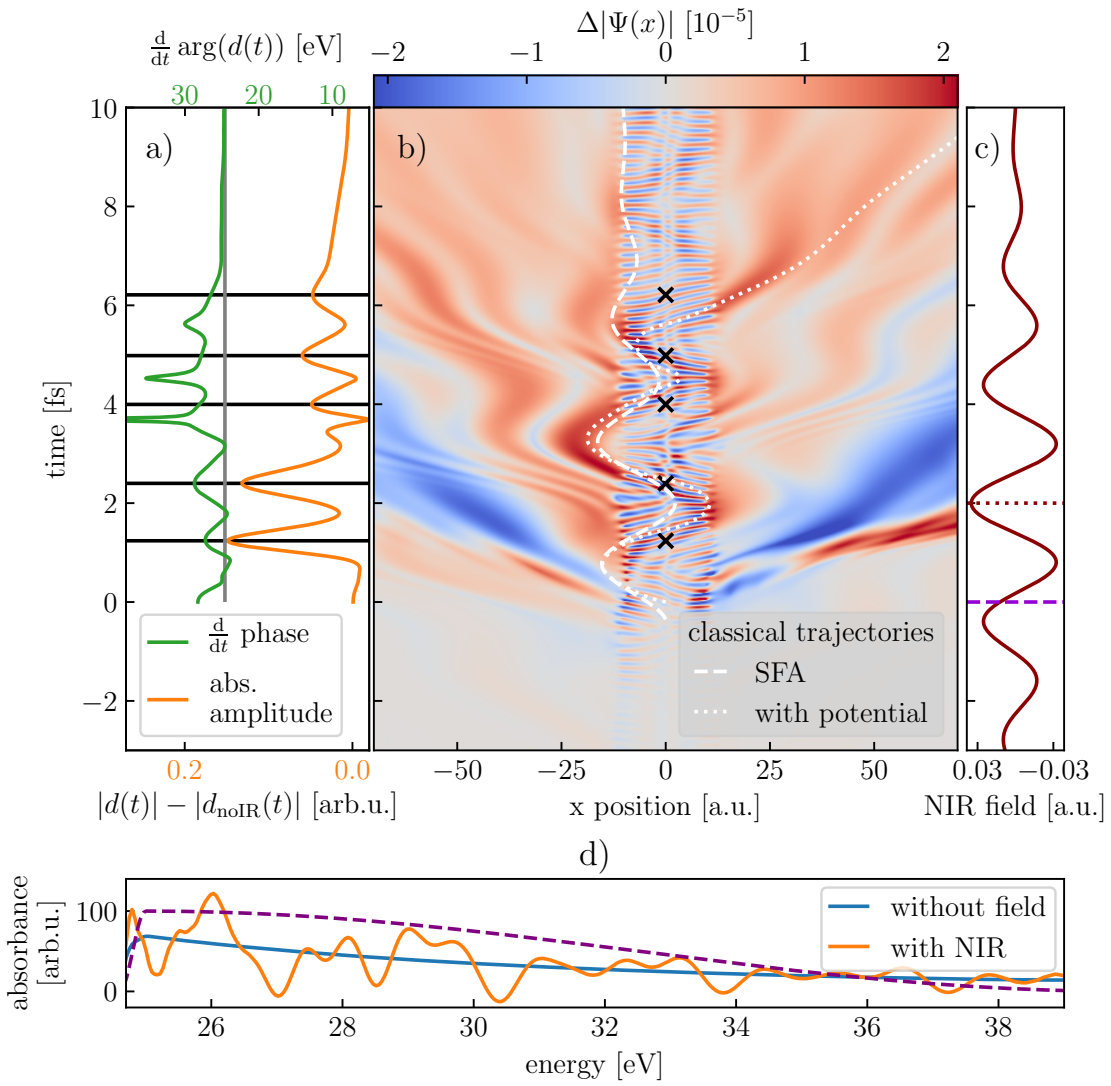

Figure 2.17: Wave function evolution at high intensity
This figure shows the dynamics, triggered by an asymmetric XUV pulse (2.4c,d), which only excites the continuum, preceded by a $FWHM = 5\,\mathrm{fs}$ NIR pulse at a delay of 2 fs and $\omega_0 = 1.7\,\mathrm{eV}$ with maximal intensity $4.4 \times 10^{13}\,\mathrm{W/cm^2}$. **a)** The reconstructed absolute dipole moment minus the dipole moment without NIR field (orange, lower axis) and the time derivative of the dipole phase (green, upper axis), using a spectral window, which is the same as the XUV spectrum. The black lines indicate the local maxima, the vertical gray line marks the ionization potential in the axis of the phase derivative. **b)** The propagating field induced differences in the wave function calculated with (2.12). The black crosses point out the positions of the maxima in a). The white dashed (dotted) line shows an example of an electron classical trajectory calculated in SFA (with the potential) for ionization at $-0.35\,\mathrm{fs}$ ($0\,\mathrm{fs}$) at $x = 0$ with $0.53\,\mathrm{eV}$ ($0.80\,\mathrm{eV}$) kinetic energy. **c)** Field of the NIR, the dashed purple line marks the XUV excitation and the dotted red the maximum of the NIR. **d)** The absorption spectrum of the continuum with (without) NIR in orange (blue). The dashed purple line shows the spectrum of the XUV and the window used for the reconstruction in a).

This is an exciting finding and it underlines the power of the reconstruction method. While the information in the spectrum is very hard to decipher, the reconstructed dipole moment offers an easy interpretation as zero-crossings ('recollision') of the wave function. In principle, one single measurement of the absorption spectrum in the continuum offers attosecond information about the evolution of the wave function.

The classical picture of electron trajectories seems to be suitable to describe the system in this intensity regime. Looking at the time derivative of the reconstructed dipole phase in Figure 2.17 a) supports this statement. If we think of the phase as e^{iS} with the quasi classical action $S = \int_0^t \frac{v^2(t')}{2} + I_p \mathrm{d}t'$, its derivative becomes

$$\frac{\mathrm{d}}{\mathrm{d}t} \arg(d(t)) = \frac{\mathrm{d}}{\mathrm{d}t} S \tag{2.18}$$

$$= \frac{v^2(t)}{2} + I_p, \tag{2.19}$$

where $v(t)$ denotes the velocity of the electron. For the first maxima of the absolute dipole moment the phase derivative shows maxima as well because at a zero-crossing the velocity becomes highest too. For the later maxima 'the' trajectory becomes less unambiguous and the interpretation of the phase complicates.

This motivates to look closer at classical trajectories. It might even be possible to calculate spectra by simulating trajectories. In the next chapter this option will be studied in detail.

Key Results of the Chapter

Within this chapter a one-dimensional time dependent Schrödinger equation simulation was set up to model the helium atom in single active electron approximation at the first ionization threshold. For this model, the influence of a moderate or strong NIR pulse on the wave function evolution was studied. Depending on the intensity, two distinct regimes were found:

- Moderate intensity, $U_p \ll \omega_0$:
  Looking at the wave function evolution: if the NIR overlaps temporally with the excitation pulse, the continuum wave packet displays a spatial asymmetry, as the electric field favors one direction. Additionally, bound states are excited for overlapping pulses and the outwards moving continuum wave packet is forced to show a small wiggling structure when interacting with a consecutive NIR pulse.

  Calculating the time delay dependent spectra, produces a figure which is comparable to experimental observations. The main features which have been described in literature as coupling to bright states, change of absorption line shape and light induced states (LISs) can be reproduced. All structures above ionization threshold can be traced back to LISs, which are the same as laser induced continuum structures (LICS) in the continuum. Due to the broad spectrum of the short pulses, the LISs have the shape of a Fano line (as predicted for LICS) convolved with a Gaussian. In the time domain, the LICS correspond to a retardation of the time dependent dipole decay, which can be explained by impeded ionization (population trapping).

- High intensity, $U_p \approx \omega_0$:
  Raising the field intensity leads to additional absorption features at the continuum edge in the temporal time overlap. For $U_p \approx \omega_0$ the continuum absorption spectrum can no longer be described by LICS since the photon picture breaks down. The wave function propagation plot shows, that the excited wave packet is now clearly driven back and forth over the nucleus. It resembles classical trajectories of ionized electrons. The reconstructed dipole moment out of the full continuum absorption spectrum exhibits peaks when a bigger part of the wave packet is driven over the nucleus. This could be interpreted as 'recollisions'. The phase of the reconstructed dipole moment shows similarities to the quasi-classical action.

Chapter 3

Classical Trajectories

Solving the TDSE numerically can reproduce experimental observations if the used approximations are reasonable. However, often it does not allow to explain an observation intuitively. A demonstrative model can much better link cause and result. In the last chapter, we have seen that the propagating wave function is reminiscent of classical electron trajectories. This motivates to examine the possibility of using classical trajectories to explain spectral field-induced features at the continuum edge.

3.1 Method

We calculate a one-dimensional trajectory $x(t)$ for an electron which has been instantaneously ionized at $t = 0$. The electron starts at the nucleus $x(0) = 0$ with the initial velocity $v(0) = v_0$. The equation of motion in atomic units is given by

$$\dot{x}(t) = v(t), \tag{3.1}$$

$$\dot{v}(t) = -\mathcal{E}(t) - \frac{\partial V(x)}{\partial x}, \tag{3.2}$$

for a linear polarized electric field $\mathcal{E}(t)$ and a potential $V(x)$. In the following, we employ the Strong Field Approximation (SFA) [37], which states that the atomic field is negligible compared to the laser field, thus we can set $V(x) = 0$. Additionally, we compute the quasi-classical action $S = \int_0^t \left(\frac{v(t')^2}{2} + I_p\right) \mathrm{d}t'$, with the ionization potential I_p, by setting $S(0) = 0$ and

$$\dot{S}(t) = \frac{v(t)^2}{2} + I_p. \tag{3.3}$$

The above set of differential equations is solved using a Runge-Kutta method of order 5(4)[38]. The electric field is modeled with a Gaussian envelope, see Appendix A.2 for details.

Our aim is to calculate the spectral response $\Im(\mathcal{F}(d(t)))$ according to equation (1.23), because it is proportional to the absorption cross section and the optical density. This makes it necessary to define a measure for the dipole moment $d(t)$.

In the presented approach, the trajectory is convolved with a Gaussian. That means,

the position of the electron $x(t)$ is taken as the center of a Gaussian wave packet Ψ. The center of this Gaussian wave packet is then driven classically by the laser field. The absolute value squared of the wave function at the origin $|d(t)| = |\Psi(0,t)|^2$ determines the absolute value of the dipole moment. This is a rough approximation of solving the three dimensional integral of the wave packet and the ground state wave function $|d(t)| = |\langle\Psi_0|x|\Psi(t)\rangle|$. We use the Gaussian wave packet of eq. (1.7), which is dispersive with time. The dispersion reflects, that the wave packet is in momentum space a distribution with finite width. The normalization of the wave function sets $d(0) = 1$ to achieve better comparability for different initial variances σ^2 of the wave packet. In total the absolute value of the dipole moment for a trajectory $x(t)$ calculates by:

$$|d(t)| = \left(\frac{\sigma^2}{\sqrt{(\sigma^4 + t^2)}}\right)^3 \cdot \exp\left(\frac{-\sigma^2 x(t)^2}{\sigma^4 + t^2}\right) \tag{3.4}$$

There are different options to choose the phase of the dipole and the normalization of the Gaussian. In the next sections several will be discussed.

3.2 Classical Trajectories with a Model Continuum

The continuum absorption spectrum shows an edge structure at the threshold. The absorption is sharply rising at the ionization potential and is then slowly decaying. As we are only interested in a change of its shape, the exact expression for the absorption $A(\omega)$ is of small importance. In this section the absorption spectrum without field is modeled by $A_{\text{model}}(\omega) = cos^2_{\text{window}}(\omega)$ function, see A.1 for the definition and Figure 3.2a) for a lineout. The absorbance of the continuum is centered at 24.6 eV, it raises for 0.2 eV and falls then for 15 eV.

As shown in[6], the dipole response $d_{\text{model}}(t)$ can be reconstructed directly from the absorption spectrum:

$$d_{\text{model}}(t) \propto \mathcal{F}^{-1}[iA_{\text{model}}(\omega)](t). \tag{3.5}$$

To take the laser field into account, we modulate the absolute value $|d_{\text{model}}(t)|$ by

$$|d(t)| = |d_{\text{model}}(t)| \cdot \exp\left(\frac{-\sigma^2 x(t)^2}{\sigma^4 + t^2}\right). \tag{3.6}$$

This means, that we have chosen a different normalization of the Gaussian wave packet compared to (3.4). It is not any more normalized to be constant in time, but in such a way, that a field-free trajectory ($x(t) = 0\ \forall t$) results in $|d_{\text{model}}(t)|$, because $\exp(0) = 1$. For a non-zero laser field the trajectories depart from the origin, which leads to a smaller value of the absolute dipole moment. In this approach the phase of the dipole moment is not changed by the field

$$\arg(d(t)) = \arg(d_{\text{model}}(t)). \tag{3.7}$$

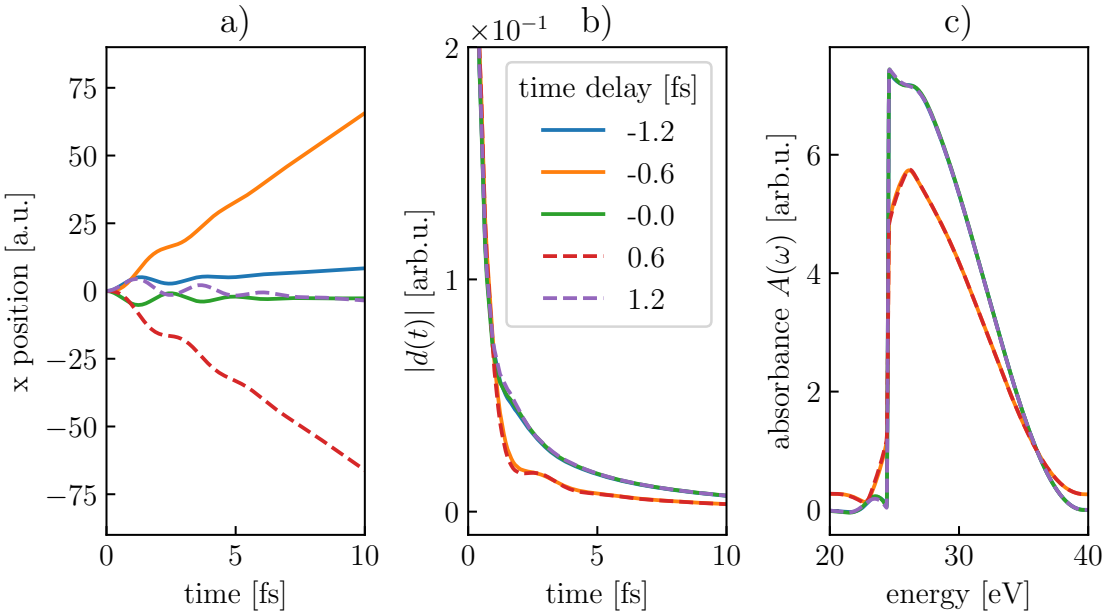

Figure 3.1: Simulation of classical trajectories using a model continuum.
a) Classical trajectories of the electrons for different time delays of the laser pulse. Positive delays are plotted dashed to make lines distinguishable. **b)** Absolute value of the dipole moment for the respective trajectory, computed with eq. (3.6). **c)** Reconstructed spectra for the different time delays, computed with eq. (3.8).

Finally, we can reconstruct the strong-field perturbed absorption spectrum using eq. (1.23)

$$A(\omega) \propto \Im\left[\mathcal{F}(|d(t)|\mathrm{e}^{i\arg(d(t))})\right]. \tag{3.8}$$

If no strong laser field acts on the system, we obtain the absorption spectrum, which we put in as a model: $A(\omega) \propto A_{\mathrm{model}}(\omega)$.

Figure 3.1 shows the trajectories, the resulting value for the absolute dipole moment and the reconstructed absorption spectrum in the case that we have a strong laser field for different time delays. Positive delays signify that the maximum field occurs after the electron has been ionized, for negative delays the maximum was before $t = 0$. A Gaussian pulse (see A.2) with $FWHM = 5\,\mathrm{fs}$, central frequency $\omega_0 = 1.7\,\mathrm{eV}$ and maximum intensity $I_{\mathrm{max}} = 3.5 \times 10^{12}\,\mathrm{Wcm}^{-2}$ acts on the electron. The Gaussian has an initial variance of $\sigma^2 = 30\,\mathrm{a.u.}^2$ and the electron starts at rest, $v_0 = 0$. The period of a light field oscillating with $\omega_0 = 1.7\,\mathrm{eV}$ equals $T = 2.43\,\mathrm{fs}$, thus for a change in time delay of $2.4\,\mathrm{fs}$ the electron trajectories are similar. As the sign of the field and the trajectories do not matter for the calculation of $|d(t)|$ and the absorption spectrum, they show a $2\,\omega_0$ modulation with time delay. If the electric field is zero at the time of the ionization $t = 0$, which is approximately the case for delay $= \pm 0.6\,\mathrm{fs}$, the electron does not return to the origin but is rapidly driven away. This leads to a stronger decay of the absolute value of the dipole moment. The spectrum is in principle the Fourier transformed dipole moment. It is a property of the Fourier transform, that for a sharp edge in $\mathcal{F}(d(t))$, contributions of $d(t)$ over a broad range in t are necessary. Thus a faster decay of the absolute dipole moment causes a

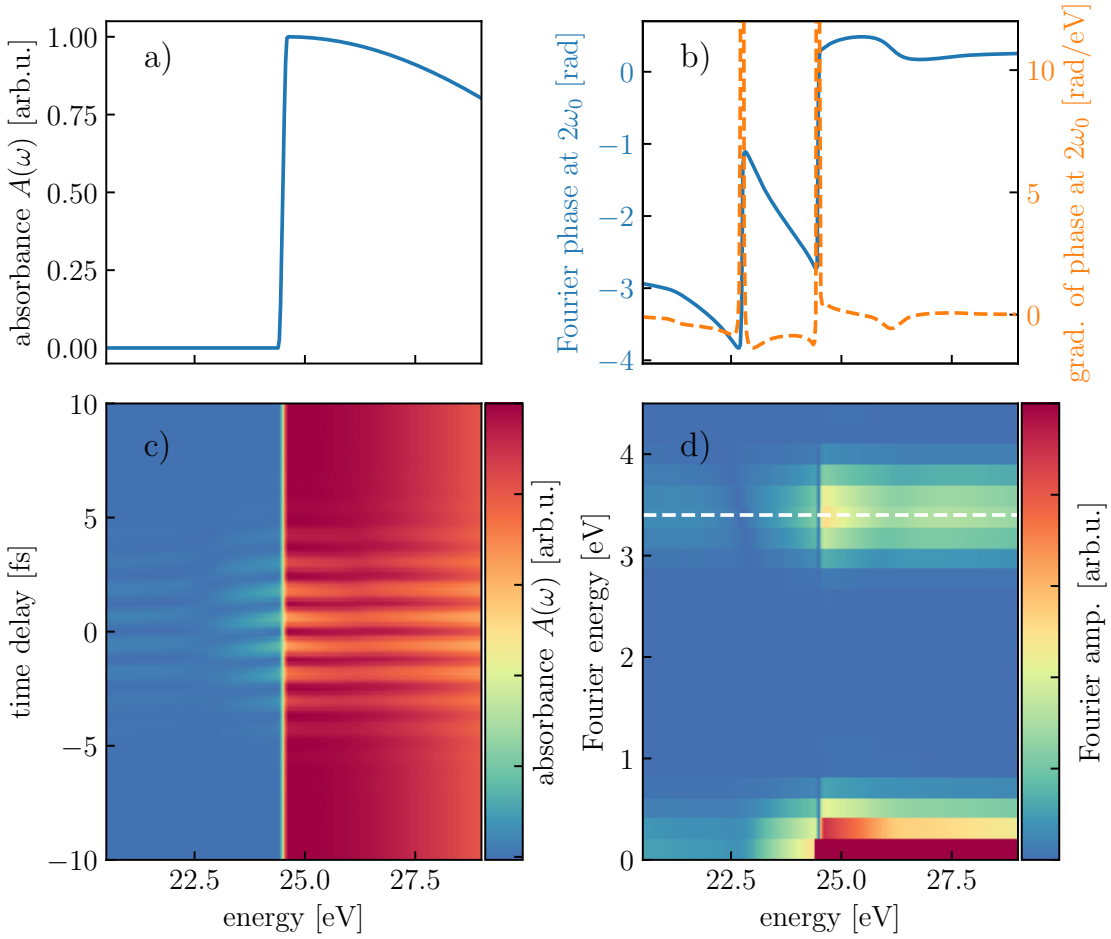

Figure 3.2: Time dependent dynamics using a model continuum.
a)The continuum edge without a strong field. This is our model input. **b)** The Fourier phase of the $2\,\omega_0$ oscillations and its gradient (dashed). **c)** Time-delay scan of the absorption spectrum at the continuum edge and **d)** its Fourier amplitude calculated by using classical trajectories with the model continuum. The DC component of the Fourier amplitude saturates to enhance the visibility of the other features. The white dashed line in d) marks the position of the $2\,\omega_0$ oscillations, for which the phase is displayed in b).

smoothing of the continuum edge, i.e. the spectrum rises before the threshold and lowers afterwards.

Figure 3.2c) shows a time delay scan of the absorption spectrum. Fourier transforming 3.2c) along the time delay axis results in 3.2d). There is a strong $2\,\omega_0$ oscillation, which amplitude does stay constant in the continuum. Recent measurements have shown a phase jump of sub-cycle absorption features at the ionization potential (see Appendix E.3). To see whether this can be explained by classical trajectories, figure 3.2b) depicts the phase of the $2\,\omega_0$ oscillation. It jumps two times. Once at $I_\mathrm{p} - \omega_0$ by $\sim 2.5\,\mathrm{rad}$ and at the ionization potential by $\sim \pi$. In the continuum there is a small shift at $I_\mathrm{p} + \omega_0$, otherwise it stays constant. The π-jump at the threshold can be explained by the smoothing of the edge. If periodically with $\frac{1}{2\,\omega_0}$ in delay time the spectrum is increased before the ionization potential and lowered after the edge, this corresponds to a π-shift of the modulation.

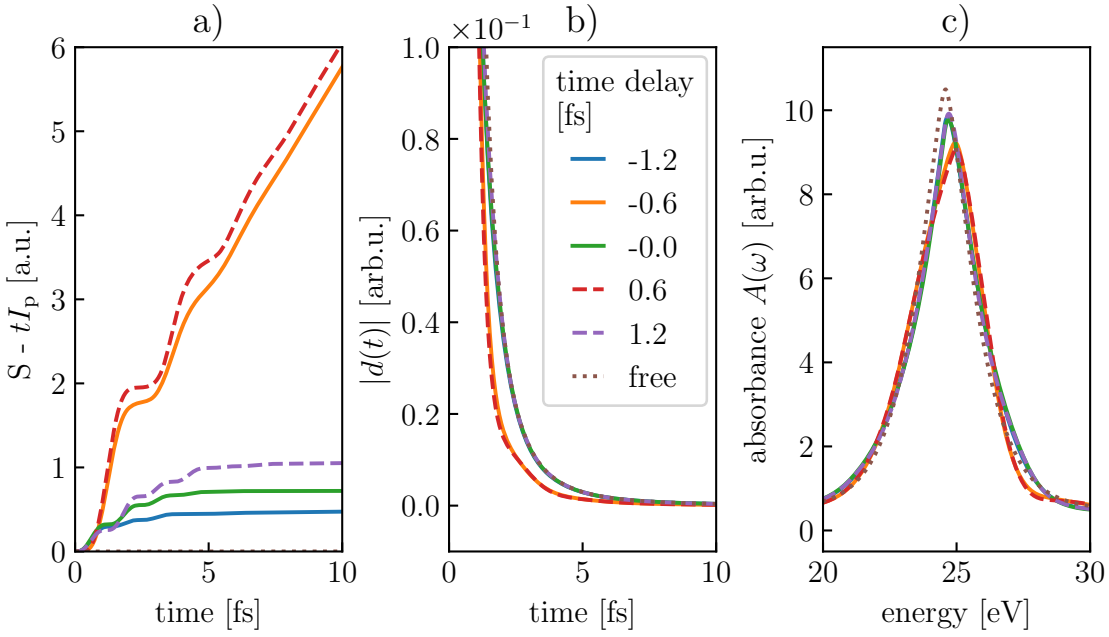

Figure 3.3: Simulation of classical trajectories without model continuum.
a) Quasi-classical action of the electrons for different time delays of the laser pulse. The linear part is subtracted. Positive delays are plotted dashed, the field-free solution is dotted. **b)** Absolute value of the dipole moment for the respective trajectory, computed with eq. (3.9). **c)** Reconstructed spectra for the different time delays, computed with eq. (3.11).

3.3 Classical Trajectories without a Model Continuum

In this section we do not use a model continuum. This has two effects. First, the Gaussian is normalized in its natural way, i.e. integration over the three dimensions in space is constant over time. Second, we need to define a phase for the dipole moment $\arg(d(t))$, for which we choose to use the above defined quasi-classical action S, see eq. (3.3). Therewith, the absorption spectrum $A(\omega)$ is reconstructed by:

$$|d(t)| = |\Psi|^2(x,t;\sigma) = \left(\frac{\sigma^2}{\sqrt{\sigma^4+t^2}}\right)^3 \cdot \exp\left(\frac{\sigma^2 x^2}{\sigma^4+t^2}\right) \tag{3.9}$$

$$\arg(d(t)) = S \tag{3.10}$$

$$A(\omega) \propto \Im\left[\mathcal{F}(i|d(t)|\mathrm{e}^{i\arg(d(t))})\right]. \tag{3.11}$$

Compared to the previous section, the laser field does, in this case, not only modulate the amplitude of the dipole moment but the phase as well. However, without a field, the action is only linear $S(t) = I_p t$. With this linear behavior, it is impossible to achieve an asymmetric absorption spectrum for the field-free case.

Figure 3.3 displays the classical action of the trajectories, the absolute dipole moment and the reconstructed absorption spectrum for different time delays. The laser parameters are the same as in the previous section and thus the trajectories itself are the same, too. The initial variance of the Gaussian is $30\,\mathrm{a.u.}^2$, which is the same as above, as well. The

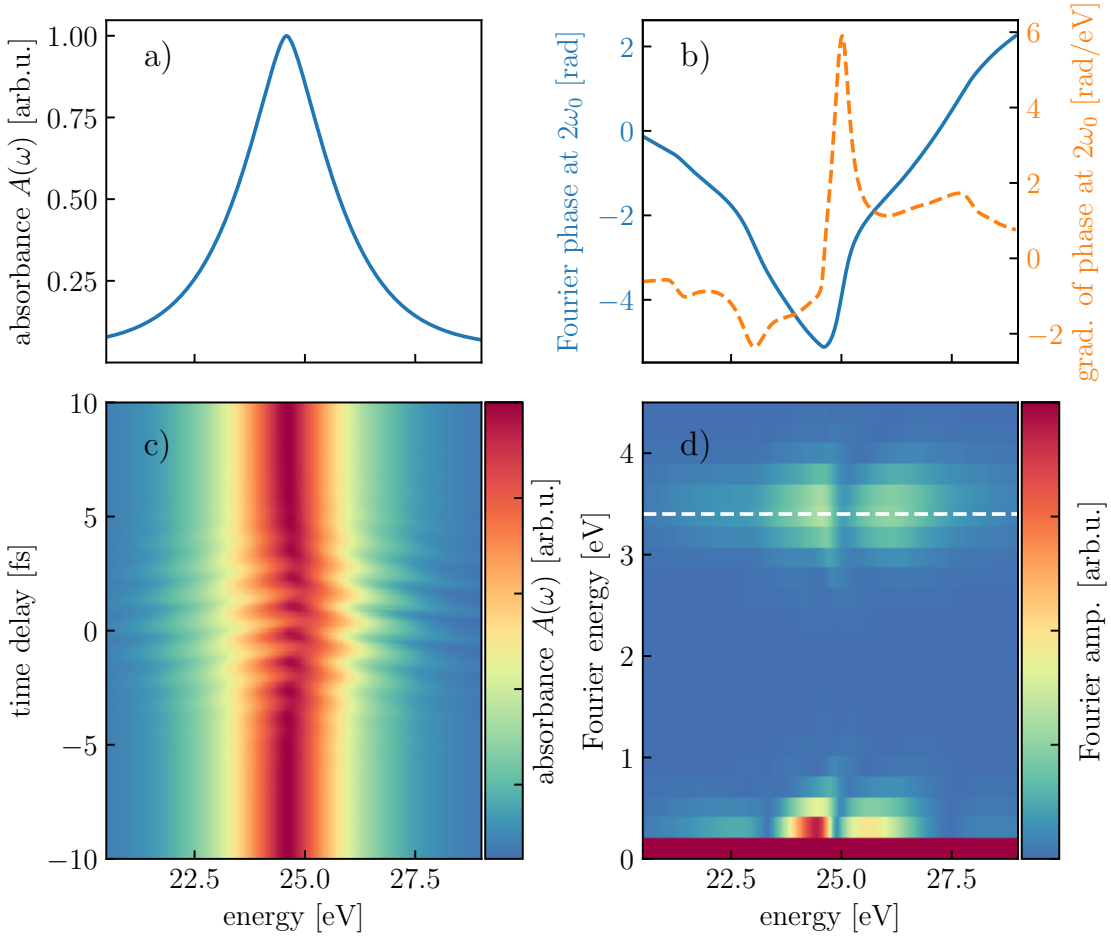

Figure 3.4: Time-dependent dynamics using classical trajectories with zero initial velocity without a model continuum.
a)The spectrum at ionization potential without a strong-field. **b)** The Fourier phase of the $2\,\omega_0$ oscillations and its gradient (dashed). **c)** Time delay scan of the absorption spectrum at the continuum edge and **d)** its Fourier amplitude calculated by using classical trajectories and the equation (3.11). The DC component of the Fourier amplitude saturates to enhance the visibility of the other features. The white dashed line in d) marks the position of the $2\,\omega_0$ oscillations, for which the phase is displayed in b).

trajectories driven away from the nucleus, at delay $= \pm 0.6$ fs, gain more action due to their higher momenta. And again, their absolute dipole moments diminish faster than for the trajectories which stay longer at the origin. However, all absolute dipole moments decrease much faster than for the model continuum case (in both models $|d(0)| = 1$). This induces the much smoother form of the spectrum, as high Fourier components are missing. Field induced changes in the spectrum are visible. The trajectories driven away lead to an absorption spectrum which is weaker and slightly shifted to higher energies.

A full time-delay scan, as in Figure 3.4 c), reveals, additionally to the $2\,\omega_0$-modulation, a slight shift to higher energies for the spectra around delay $= 0$. This shift is provoked by the ponderomotive energy (see section 1.8), which calculates for the used pulse parameters to 170 meV. The phase of the $2\,\omega_0$ oscillations depicted in 3.4b) shifts by $\sim \pm 1$ rad/eV, thus the $2\,\omega_0$-lines in the time scan 3.4c) are not horizontal as it has been the case in the

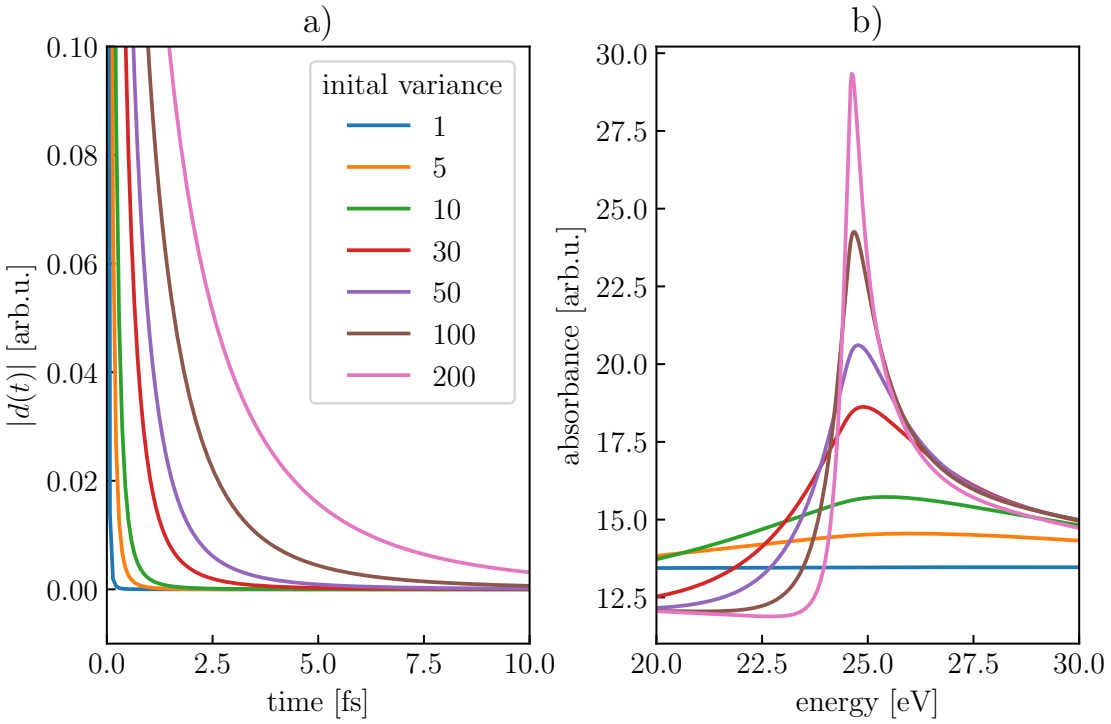

Figure 3.5: a) The absolute value of the dipole moment and b) the reconstructed absorption spectrum without a laser field for different values of the initial variance (units in a.u.^{2}) of the Gaussian used to convolve the classical trajectories. By a Monte Carlo method the dipole was calculated as an integral over all possible initial velocities, see (3.13).

previous section. Additionally, the phase jumps at I_p by nearly π, but not as sharply as for the model continuum, which can be a consequence of the ponderomotive shift.

3.4 Classical Trajectories with Initial Velocity without a Model Continuum

Following the reasoning of section 1.7 the dipole moment computes by the integral (1.28). The presented model sets

$$d_x(v(t)) = |\Psi|^2(x,t) \tag{3.12}$$

where x is the position of the classical trajectory. The trajectory completely determines the velocity $v(t)$ and therefore an integration over it is not feasible. The dipole moment then equals $d(t) = i|\Psi|^2(x,t)\ \mathrm{e}^{iS(t)}$, which reproduces the formula of the previous section. However, there are different trajectories possible for one set of laser parameters depending on the initial velocity v_0. To account for all possible trajectories, an integration over all initial velocities is necessary, i.e.

$$d(t) = i \int \mathrm{d}v_0\ |\Psi|^2(x,t;v_0)\ \mathrm{e}^{iS(t;v_0)}. \tag{3.13}$$

This integration can be carried out by the Monte Carlo method, which is described in A.3.

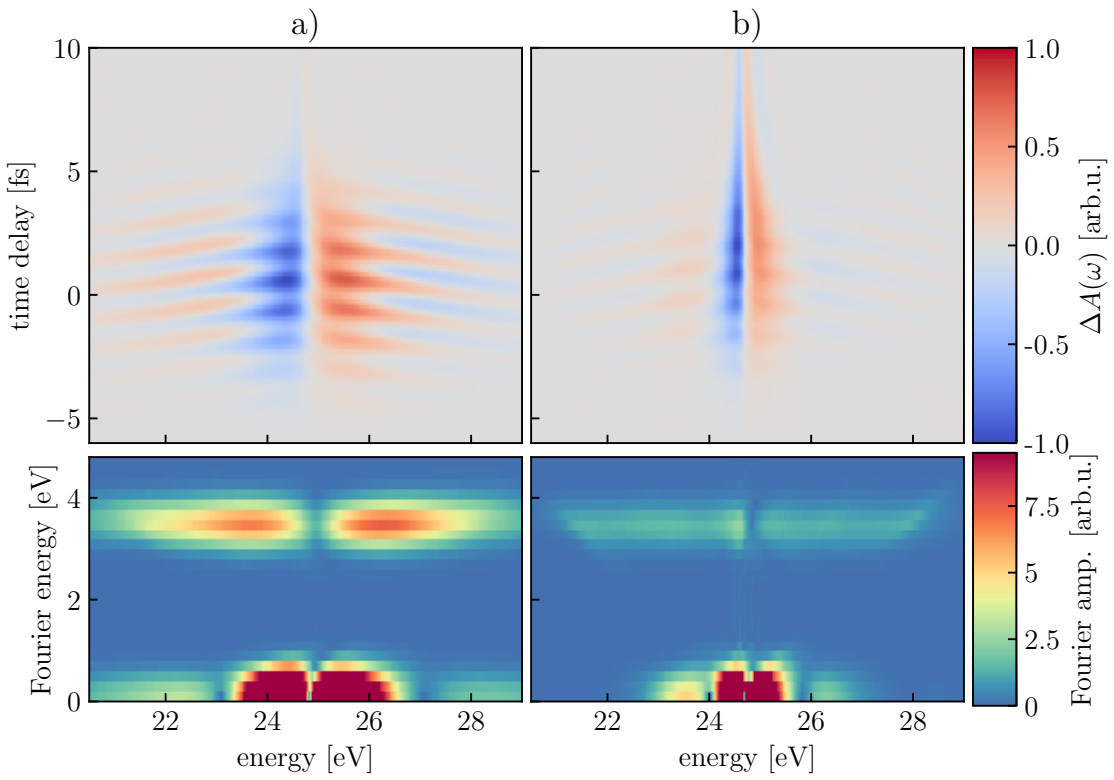

Figure 3.6: The field-induced difference of the absorption spectrum for an initial Gaussian variance of **a)** 30 a.u.^{2} and **b)** 200 a.u.^{2} using classical trajectories with different initial velocities. The figures on the top display the difference in absorption spectrum with and without a field, dependent on the NIR time delay. The ones on the bottom show for the same data the absolute value of the Fourier transformation along the time-delay axis.

Figure 3.5 shows the dipole moment and the reconstructed spectrum using this method for different initial values of the Gaussian variance without a strong laser field. For the Monte Carlo method 10000 trajectories are computed, with initial velocities sampled from a Gaussian shaped probability density function with 1.5 width. With this approach, the absorption spectra are not symmetric any more, because the phase of the dipole is not linear. The higher the width of the Gaussian, the sharper the edge. This is due to the fact, that an initially small Gaussian spreads considerably fast. The normalization causes a strong decrease of its value around the origin, and therefore, there are no high Fourier components left to build up an edge. This is a first hint, that the SFA might in this context not be appropriate, because free wave packets spread too fast. The initial variance needed to reduce the dispersion is clearly bigger than the atomic size. This decreases 'recollision' effects, because the light field induced dipole changes are less pronounced.

Figure 3.6 depicts the value of the absorption spectrum with a NIR field minus the absorption spectrum without a field $\Delta A(\omega) = A_{\mathrm{NIR}}(\omega) - A_{\mathrm{free}}(\omega)$. The pulse parameters are the same as in the previous sections. The subfigures 3.6 a) and b) compare two different values of the initial variance of the Gaussian, 20 a.u.^{2} and 300 a.u.^{2} respectively. Although the continuum edge looks different (compare Figure 3.5), the features in the time delay scan are similar. There is a strong sub-cycle modulation at $2\,\omega_0 = 3.4\,\mathrm{eV}$ Fourier energy.

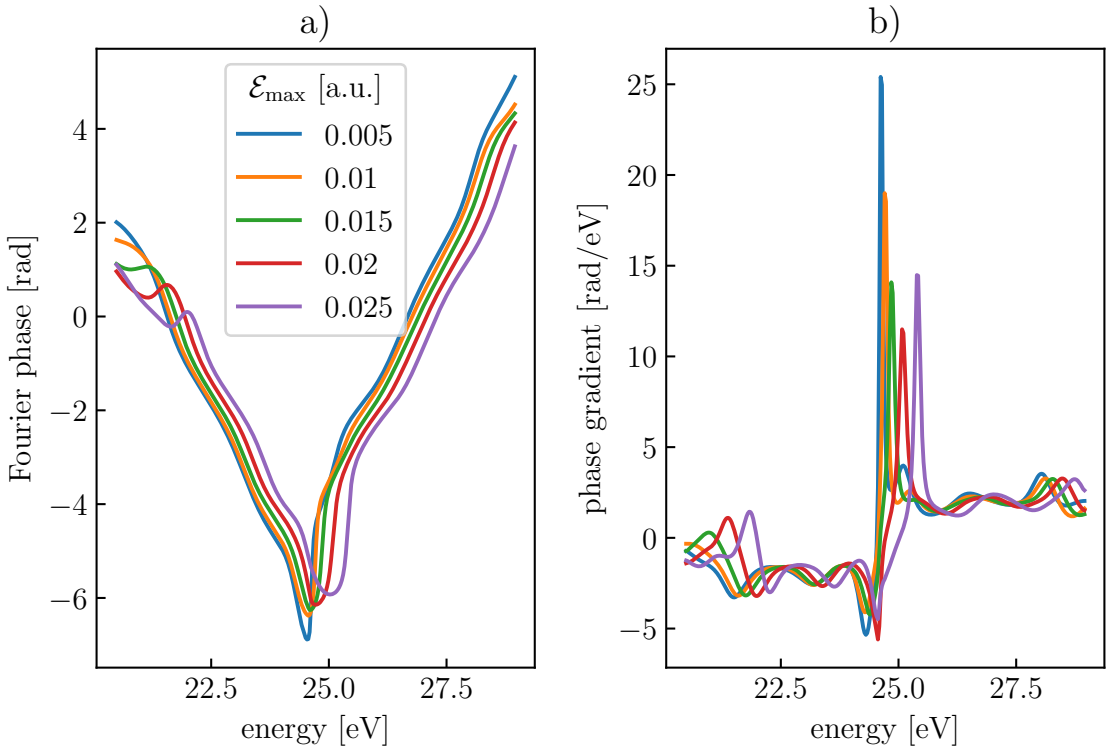

Figure 3.7: **a)** Phase and **b)** its gradient of the $2\,\omega_0$ oscillations in the time delay scans for different strength of the NIR field. The initial variance of the Gaussian is $200\,\text{a.u.}^2$ and only the phase is influenced by the NIR field (GBR).

This modulation exists within $I_\text{p} \pm 2\,\omega_0$ and its phase shifts slowly with energy, thus the stripes in the time-delay spectrum are not parallel to the energy axis. Additionally, the ponderomotive energy shifts the edge towards higher energies during the pulse overlap. For time delays bigger than the pulse width, it is still influencing the shape of the edge. This is more significant for the case b) of a broad Gaussian. This change of shape results in hyperbolic features in a time-delay scan, which are in our case overlapped by the $2\,\omega_0$ modulation around time delay zero. These features remind of a change in the line shape in experimental time dependent absorption spectra. It can there be explained by perturbed free indcuction decay or NIR-induced depletion of the states in the dipole-control model [39].

It is interesting to note, that for a broad Gaussian the quasi-classical action is essentially the only reason for modulations of the spectrum. Figueira de Morisson Faria et al. define in reference [40] the broad Gaussian approximation (GBR) as the case when $d_x(p + A(t)) = \text{const}$. This means, that the light has no influence on the dipole matrix element. In the classical trajectories model this condition translates to

$$d_x(v(t)) = |\Psi|^2(x, t) \tag{3.14}$$

Thus, it is possible to replace the absolute value of the dipole moment with the corresponding field-free value without a significant change in the spectra. Only the dipole phase is modulated in this case.

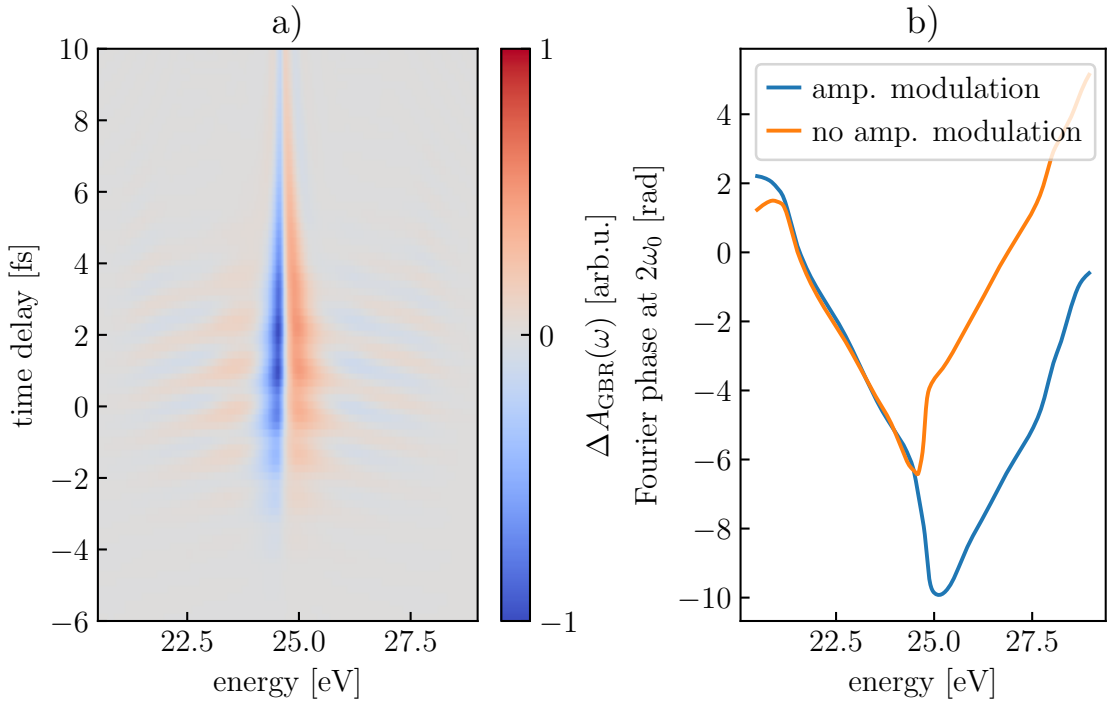

Figure 3.8: Broad Gaussian approximation
a) The field induced difference of the absorption spectrum for an initial Gaussian variance of 200 a.u.^{2} using classical trajectories with different initial velocities using the absolute dipole moment of the unperturbed trajectories. **b)** The Fourier phase of the $2\,\omega_0$ oscillation for the complete calculation with amplitude modulation (see Figure 3.6 b)) and without as in this figure a)

.

The phase of the $2\,\omega_0$ oscillations in time delay scans using the above defined broad Gaussian approximation and the phase's gradient are shown in Figure 3.7 for different NIR field strengths. There is a phase jump of $\sim \pi$ around I_p. For stronger fields, the phase jump moves to higher energies which supports the observation, that the continuum edge is shifted by the ponderomotive energy. The plot of the gradient of the phase shows, that smaller structures in the region of 26 eV to 29 eV exist and shift as well with higher field strengths. The shape of the curves is very similar. Thus, we can deduce that using the broad Gaussian approximation reduces the strong-field dynamics at the ionization potential to a ponderomotive effect. Increasing the NIR intensity, the features shift due to the ponderomotive energy but they stay similar.

Figure 3.8a) shows a time-delay scan of the absorption spectrum minus the spectrum without NIR using GBR. By eye, it can hardly be discriminated from the calculation with amplitude modulation in 3.6b). A closer look at the phase of the $2\,\omega_0$ oscillation reveals that there are important differences, mainly at the ionization potential.

To illustrate the change clearer, Figure 3.9 a) displays the difference of the two time delay scans 3.6b) and 3.8a). These are the strong-field effects, which do not originate from a ponderomotive shift, but which are due to changes in the electron's trajectory. They are one order of magnitude smaller than the features of the ponderomotive effect.

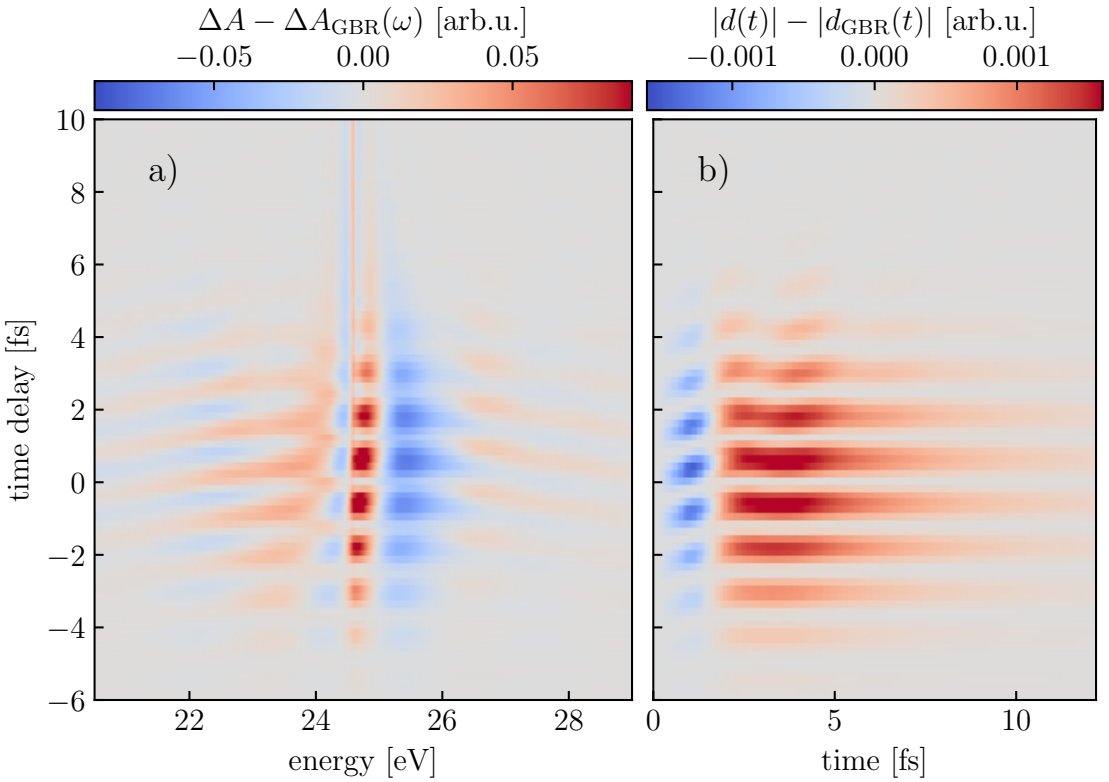

Figure 3.9: Impact of amplitude modulation
a) The difference of the absorption spectra with and without amplitude modulation depending on time delay (Figure 3.6 b) minus 3.8a)) **b)** The difference of the absolute dipole moment with and without amplitude modulation depending on time delay.

For time delays which correspond to a weak NIR field at the instance of the XUV pulse, the absorption spectrum is alternately lowered and increased at the ionization threshold without a distinct periodicity.

Figure 3.9b) shows the absolute dipole moment of the full calculation minus the absolute dipole moment without an NIR field, which is the same as the GBR case. The difference in dipole moment is negative around 1 fs and positive at 2 fs to 5 fs. This means, on average over all initial velocities the electron is first faster driven away and then pushed back in such a way, that it is closer to the nucleus than for the field-free trajectory. This can be seen as field-induced recollision of the electron wave packet. The time delays which show the strongest modulation are those, for which the ionization happens at a zero crossing of the NIR electric field.

3.5 Influence of the Light Polarization and Dimensionality

The polarization of the light has a huge influence on the classical trajectory of a free electron. In the experimental setup it is possible to change from linear to circularly polarized light, thus these two cases shall be considered here, as well. To simulate circularly polarized light, it is necessary to add a second dimension. The following changes are therefore applied to the simulation:

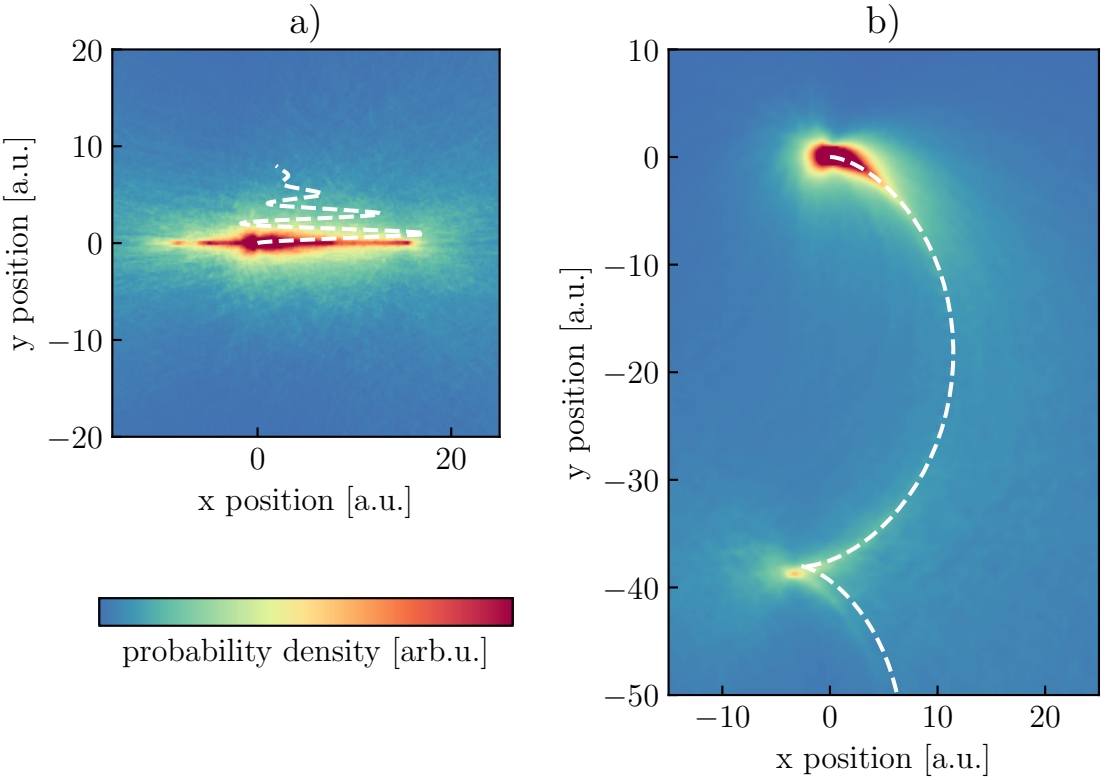

Figure 3.10: Classical electron trajectories dependent on the light polarization
a), **b)** Spatial probability density of the electron's position for $t < 10\,\text{fs}$ for linear and circularly polarized light calculated out of 20000 classical trajectories. The angular distribution $P(\theta) \propto \cos^2(\theta)$ and the absolute velocity is Gaussian distributed with a width of 0.4 a.u., which corresponds to 4 eV. The NIR parameters are given in the text. The white dashed lines indicate a trajectory for initial velocity $v_\text{x} = 0.009\,\text{a.u.}$, $v_\text{y} = 0.005\,\text{a.u.}$

- The electron position is described by $\boldsymbol{r} = (x, y)$.
- x and y are propagated independently using the equation of motion (3.1). In the circular case the light for both dimensions has an electric-field amplitude which is by a factor of $\frac{1}{\sqrt{2}}$ smaller than for the linear case. Additionally, for circularly polarized light the x-component of the light has a carrier envelope phase (CEP) of zero and for the y-component CEP $= \pi/2$.
- The Gaussian wave packet is 2-dimensional, which is equivalent to replace in the formulas of the previous sections x by $|\boldsymbol{r}| = \sqrt{x^2 + y^2}$.
- The quasi-classical action calculates to $S = \int_0^t \frac{v_x(t')^2 + v_y(t')^2}{2} + I_p \mathrm{d}t'$.
- The initial velocity distribution is 2-dimensional. As we assume the electronic ground state to be an s-wave, we expect the ionized electrons to be in a p-orbital. The angular distribution of the electrons thus follows $P(\theta) = \frac{2}{\pi}\cos^2(\theta)$ for $-\pi/2 \leq \theta \leq \pi/2$. $\theta = 0$ points in the x direction.

To get an understanding of the disparity between linear and circularly polarized NIR light, Figure 3.10 shows the qualitatively different trajectories for electrons driven in these

fields. The NIR pulse has the width $FWHM = 5\,\text{fs}$, the central photon energy $\omega_0 = 1.7\,\text{eV}$, the peak intensity $I_{\text{max}} = 4.4 \times 10^{13}\,\text{W/cm}^2$ and is centered at 1.2 fs. In the linear case, 3.10 a), many trajectories stay in the vicinity of the nucleus (which is at the origin), as the electrons are driven back by the light field. For circularly polarized light, 3.10 b), there is no return for the electrons. They are spiraling away.

These different trajectories result in different time-delay dependent absorption spectra. Their changes relative to the unperturbed case are compared in Figure 3.11 together with the corresponding reconstructed dipole response. The figure shows three cases, namely calculation in 1D as in the previous paragraph (3.11a), calculation with linear light in 2D (3.11b) and calculation with circularly polarized light in 2D (3.11c). Adding a second spatial dimension for linear polarized light, does not alter the spectrum strongly. For circularly polarized light the main additional effect seems to be a reduced $2\omega_0$ modulation. The subfigures 3.11 2) and 3) show the normalized absolute reconstructed dipole moment and they differ only in the used window. The window of all subfigures 2) is wide and contains all spectral information of the continuum up to an energy of 37 eV. For subfigures 3) the window is limited to energies until 28 eV. This corresponds to the energy range which is in the helium continuum accessible experimentally without strong noise. In principle, it is, of course, possible to take the dipole moment directly out from the simulation, but this figure should be comparable to what we can see in experimental data. By using the dipole reconstruction method, we also concentrate on the energies above the threshold, as the window cuts out lower energies. This would not be the case, if we directly look at the dipole moment. In all subfigures 2), the first two femtoseconds show clear sub-cycle features, which are not visible for the smaller window as used in the subfigures 3). Otherwise the difference is negligible.

The most interesting feature, which separates the different polarizations, is highlighted with arrows. At $\sim 3\,\text{fs}$ the reconstructed dipole moment peaks for some time delays. Most dominant is the peak for the 1-dimensional calculation, weaker for the 2-dimensional case with linear polarized light and vanishing for the circularly polarized NIR. This feature can be explained in the 'recollision' picture. In one dimension all returning trajectories are exactly driven over the nucleus, in two dimensions most trajectories will only be in the vicinity of the parent ion because of the initial velocity component orthogonal to the light polarization. And, it is very unlikely that circularly polarized light pushes an electron back to the nucleus. This can be explained by the fact, that the trajectories are more easily driven away from the nucleus in two dimensions and with circularly polarized light it is even more unlikely for an electron to be pushed back to the nucleus.

3.6 Comparison to TDSE Results

The reconstructed dipole moment of Figure 3.11 a.3) at delay $\tau = 2\,\text{fs}$ delay can be compared to the TDSE result in Figure 2.17 a). Figure 3.12 shows the respective lineouts. The two peaks below 3 fs reproduce qualitatively. For later times, the light-induced dipole features diminish to zero for the classical trajectory method, because the wave packet is dispersed, whereas the TDSE result still shows peaks for following 'recollisions'. Thus,

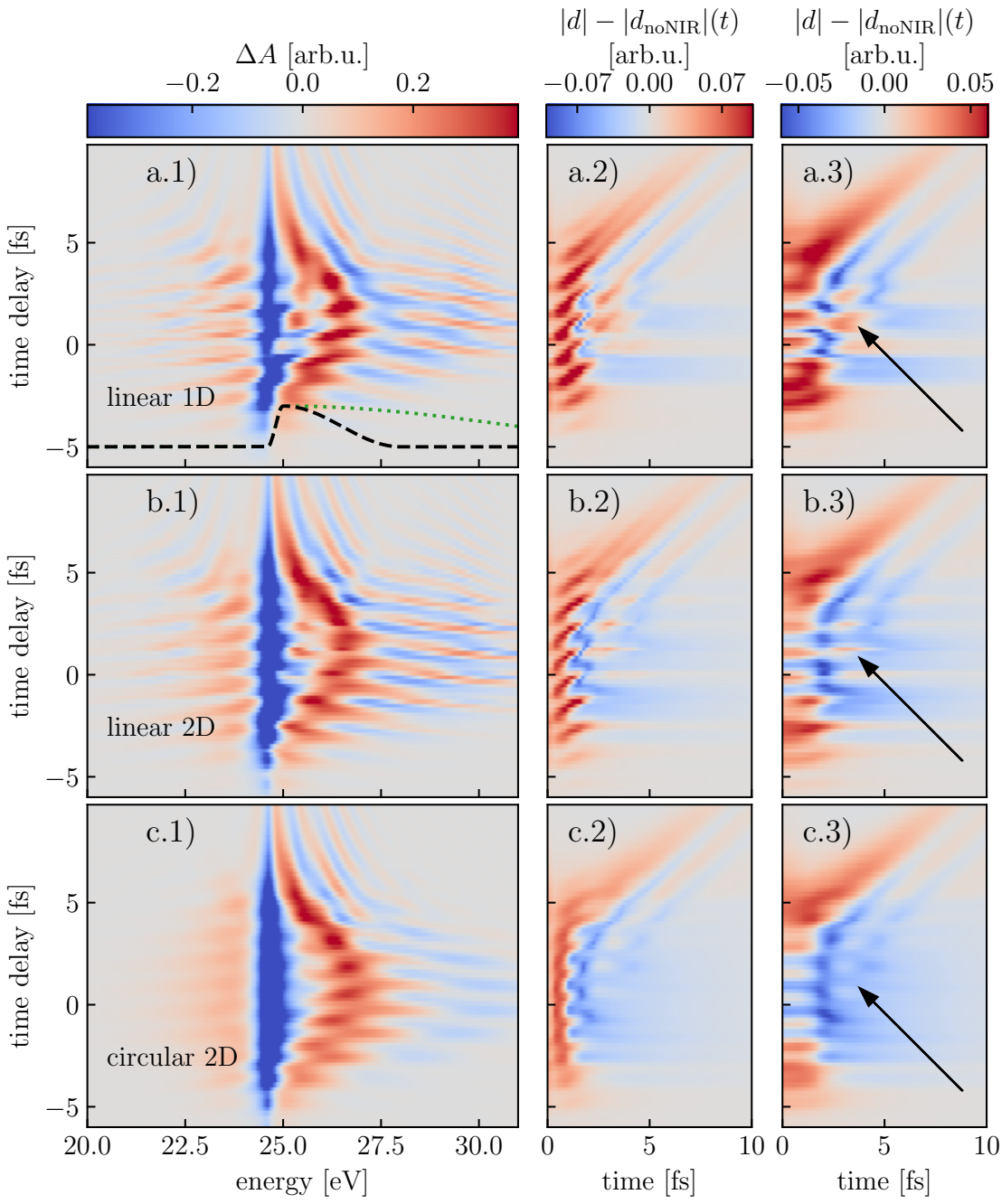

Figure 3.11: Time-delay dependent changes in the absorption spectra and the reconstructed dipole for different polarizations.
a Linear polarized light, propagation in one dimension **b** Linear polarized light with 2-dimensional trajectories. **c** Circular polarized light with 2-dimensional trajectories. The subfigures 1) on the left-hand side illustrate the absorption spectrum minus the absorption spectrum without a strong field. Subfigures 2) and 3) show the absolute value of the reconstructed dipole moment with field minus the value without a field . The used window function is $cos^2_{\text{window}}(\omega)$, centered at 24.6 eV, with a rising edge of 0.1 eV and a falling edge of 12 eV for 2) and 3 eV for 3). The window function is shown in a.1) green dotted and black dashed, respectively. The arrows highlight features which relate to 'recollision'.

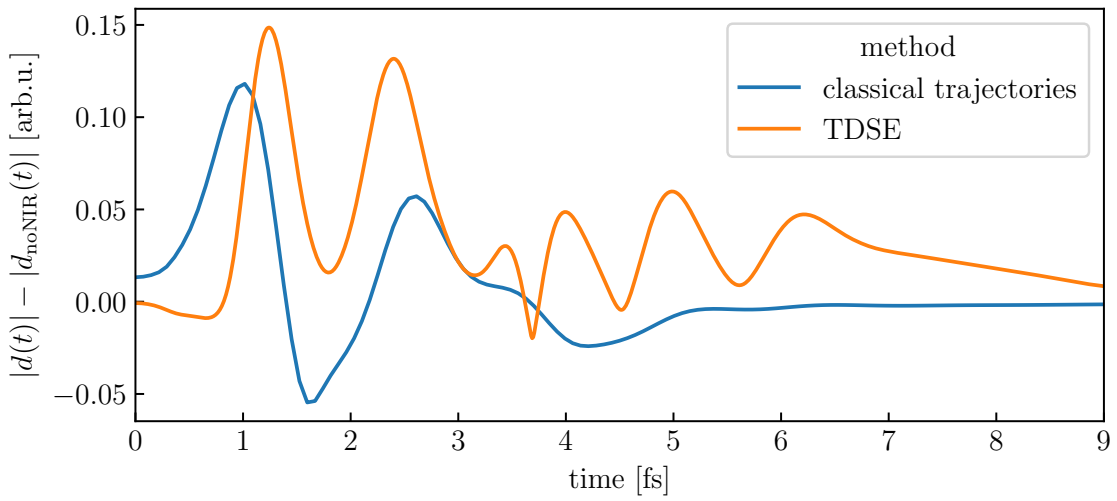

Figure 3.12: Comparison between the changes in the reconstructed dipole moment, which are strong-field induced, for the classical trajectory method (data from Figure 3.11 a.3) and the TDSE simulation (compare Figure 2.17 a).

aiming for an even higher agreement could be possible by reducing the wave packet dispersion for the classical trajectories. This means going away from the SFA and taking into account the atomic field. One can also model the ionization step more precisely and include a non-zero initial electron position.

Key Results of the Chapter

In this chapter different methods to calculate the spectral strong-field response of a continuum by means of classical trajectories were developed and compared. The established methods (e.g. analysis of the Fourier phase of $2\,\omega_0$ oscillation) allow for a comparison between the different approaches. Several statements deduce from this chapter:

- All presented methods show a change of the absorption spectrum at the ionization threshold that is modulated by $2\,\omega_0$ in time delay.
- A phase jump of $\sim \pi$ of the $2\,\omega_0$ modulation phase leads to a periodic *softenting* of the continuum edge.
- If the quasi-classical action is taken into account, the $2\,\omega_0$ modulation phase decreases nearly linear before the ionization potential and increases with the same inclination afterwards, which leads to tilted absorption features. Additionally, the edge is shifted by the ponderomotive energy.
- The ponderomotive effect dominates for moderate intensities, but for higher intensities ($U_\mathrm{p} \approx \omega_0$) some features due to the driven trajectories ('recollision') can be carved out.
- The observed 'recollision' features depend on the light polarization and the dimensionality in which the trajectories are calculated.
- The simulation results for strong fields agree qualitatively with the TDSE simulation. To enhance the agreement it might be useful to go beyond SFA.
- The original motivation for this chapter to find a demonstrative model could not completely be satisfied, as integration over the initial velocities was used. This makes it impossible to assign a single trajectory to one spectrum. Without integration the continuum is a symmetric line (using no model) and an NIR field always lowers the absolute dipole moment.

For further comparison to other methods, Appendix C introduces additionally two other techniques to look at continuum dynamics in SFA. They are based on numeric integration of the Lewenstein integral and on an adapted TDSE calculation and both show similar results for moderate field strengths.

The qualitative agreement between the results from this chapter using classical trajectories and the TDSE simulations for high intensities is promising. The principal question is now: What do we observe in the experiment? Can we interpret the measurement with this classical model?

Chapter 4

Experimental Setup and Methods

The experimental technique which is used in this work is known as attosecond transient-absorption spectroscopy (ATAS). It reveals ultrafast atomic dynamics on the intrinsic electron time scale [41–43]. In the presented experiment a weak XUV pulse, which is a few hundred attoseconds long, excites helium atoms to energies around the ionization potential. This excitation triggers an oscillation of the atom's electric dipole moment, which is then modified by a time delayed strong, femtosecond NIR pulse. An XUV spectrometer transfers this dynamics into the spectral domain.
As the XUV is produced by high-harmonic generation (see 1.7), it is intrinsically locked to the generating NIR pulse. In the scope of this thesis, the setup was upgraded to split the NIR before the HHG. One part of the pulse generates the XUV and is dumped afterwards, the second part can be altered in intensity, time delay and polarization and is then coupled into the vacuum chambers to overlay with the XUV.
In the next sections the single constituent parts of the experiment will be described following the light propagation. Additionally, the advantages, caveats and properties of the external beam path upgrade are discussed.

4.1 Laser System

The source of the NIR light is the commercial Ti:Sapphire multi-pass amplifier laser system FEMTOPOWER$^{\text{TM}}$ HE/HR CEP4. Therein $\sim 6\,\text{nJ}$ pulses from the oscillator are CEP stabilized and then amplified using chirped pulse amplification (CPA) [2]. For more details refer to [44].
At the exit, the system delivers 20 fs pulses of 3 mJ pulse energy at 3 kHz repetition rate. The light is then guided through a double differentially pumped hollow-core fiber filled with helium. Due to the high intensity inside the fiber, self phase modulation induced by the Kerr effect broadens the spectrum. After the fiber, the light passes seven pairs of chirped mirrors to overcompensate the dispersion resulting from the propagation and the following optical elements (window, beam splitter). A pair of movable fused silica wedges can be controlled to fine tune the dispersion. They can additionally be used to conduct a dispersion scan, which can reconstruct the temporal profile of the pulse [45]. After compression sub-5 fs pulses with 1 mJ can be achieved.

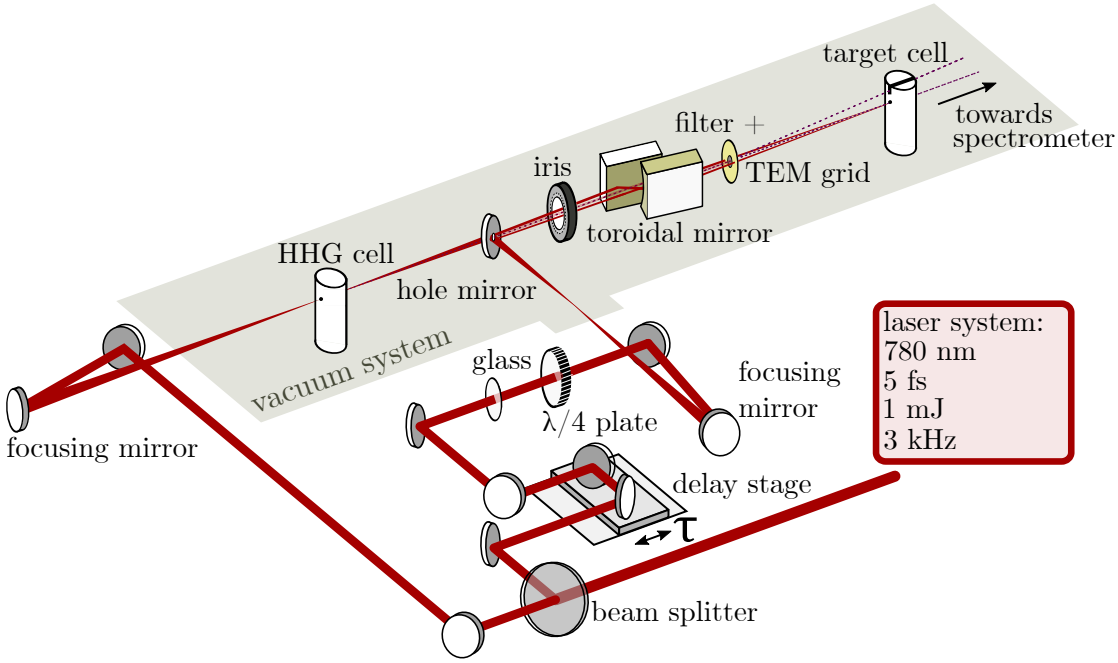

Figure 4.1: Sketch of the experimental setup including the external beam path and the beamline. The NIR (XUV) beam path is depicted by the red (dashed purple) line. All non-labeled elements are flat mirrors.

4.2 External Beam Path and Beamline

Why does it make sense to use a different NIR pulse instead of the one generating the XUV for the experiment? There are mainly two reasons.

- Delay control can be achieved by a retroreflector. This offers the opportunity to tune over a large delay between NIR and XUV without suffering from beam walk-off. The implemented delay stage has a piezo travel range of 260 μm which corresponds to a time delay range of 1.7 ps. If XUV and NIR are split after HHG, the range is limited to $\sim$ 50 fs [46].
  With a picosecond delay range it is e.g. possible to observe vibrational dynamics of molecules.

- The NIR can easily be altered without influencing the XUV. This is especially helpful when changing the NIR polarization. Without complicated schemes [47] the XUV is always linear polarized aligned with the NIR polarization and circular polarized NIR light does not lead to HHG [48]. With an external NIR beam coupled into the experiment, the polarization control is as easy as adding a broadband wave plate.

Figure 4.1 shows a sketch of the setup. The NIR is first split by a broadband 70:30 beam splitter. The more intense transmitted part is focused into the HHG, where the XUV is produced in xenon gas. The reflected light goes on the retroreflector, which controls the time delay. Additional to the piezo actuator, the retroreflector is mounted on a delay stage which a 2.5 cm micrometer screw to simplify alignment. Before focusing in the vacuum chambers, the beam passes extra glass, to compensate for the dispersion of the

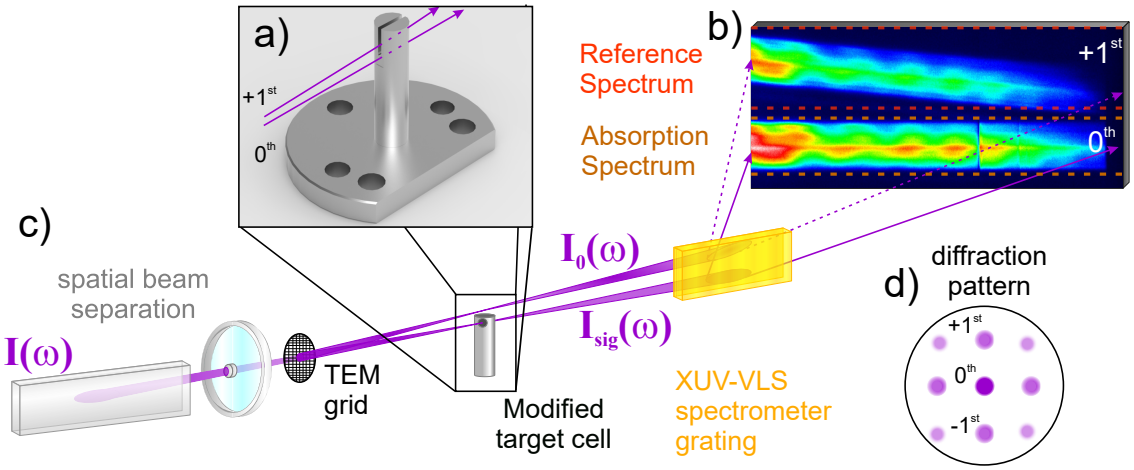

Figure 4.2: Principle of the *in situ* reference, adapted from [46]
a) Target cell with a hole for the transmission of the 0^{th} XUV order through the gas target and a slit, to allow the 1^{st} order propagation in vacuum. All other orders are blocked. **b)** Image of the camera with reference and absorption spectrum spatially separated. **c)** Elements in the beamline important for the measurement scheme. The reference beam is above the signal beam. **d)** Diffraction orders of the TEM grid. Only the 0^{th} and the 1^{st} order are used.

beam splitter in the other arm, and it passes a $\lambda/4$-plate, which can be turned to change the linear NIR polarization into a circular one. In the beamline the two beam paths are rejoined using a mirror with a hole.
The XUV produced in HHG has a much smaller divergence than the NIR. Thus, the Ø=2 mm hole drilled in 45 deg transmits all the XUV while blocking most of the generating NIR. The external NIR exhibits a doughnut mode after reflection from the mirror with the hole and can therefore be weakened by the iris without affecting the central XUV. The iris is motorized to allow for an automatized intensity scan.
A toroidal mirror refocuses the light into the target cell. After it, while the mode is still sufficiently big, a split filter is mounted. The outer part consists of 7 μm thick Kapton foil, which should transmit the NIR. A 200 nm thin aluminum foil covers a 2 mm diameter hole in the center. This foil filters out the remaining NIR from the HHG process.
The filtering does not work perfectly. A small amount of the generating NIR passes through the Kapton. This leads to a leakage effect, i.e. at time delay 0, a weak NIR pulse is always present.

4.3 Measurement of the Absorption Spectrum

Directly behind the aluminum filter (the NIR is not affected), a copper-mesh microgrid transmission grating with a spacing of $d = 16.5\,\mu$m is installed. Such grids are used in transmission electron microscopy (TEM). Here, its purpose is to obtain an exact copy of the XUV pulse, which can be used as a reference for the absorption measurement. Figure 4.2c) shows in detail the XUV beam path. The strongest order of the XUV diffraction pattern is the 0^{th} one, which is going through the gas target together with the NIR. It

probes the system, thus the spectrum, which is diffracted by a variable line spacing grating, shows absorption features on the recording camera chip.
The optical density (OD) is proportional to the absorption of the system $A(\omega)$ and its cross section $\sigma(\omega)$. It is the quantity we want to know and it is calculated by

$$OD(\omega) = -\log_{10}\left[\frac{I_{\text{sig}}(\omega)}{I_0(\omega)}\right] \propto A(\omega) \propto \sigma(\omega). \tag{4.1}$$

Therefore, additionally to the spectrum with absorption features $I_{\text{sig}}(\omega)$, we need to know the original spectrum $I_0(\omega)$. As the HHG is highly non-linear, the spectrum of the XUV changes from shot to shot. Taking the reference spectrum sequentially (alternating measurements of the spectrum with and without target gas), will thus introduce an error, because the measured reference is not precisely correct. There is another method to obtain a reference spectrum, which is often used. Since the HHG spectra are due the short time scales involved at generation very smooth, sharp features must result from the absorption. By filtering out high Fourier frequency components, one can thus reconstruct the reference spectrum. This method works very well for discrete absorption features as lines, if the states are long-lived, but it cannot be used in the presented study as it fails at the ionization edge. The continuum itself is very flat in absorption and has a sharp edge at its beginning. Thus, in Fourier space, the continuum consists of low and high Fourier energies. Hence, using a lowpass filter would alter the absorption features which we want to observe.

The only satisfying solution is to measure absorption and reference spectrum at the same time. This is possible with the presented setup. As Figure 4.2 shows, the 1^{st} order of the TEM diffraction order can pass through a slit in the target cell, which is not filled with target gas. The unaltered $I_0(\omega)$ diffracts at the same grating and is recorded on the same camera chip as the probe beam with absorption signal. They are only separated spatially. Since the diffraction of the TEM grid is energy dependent as well, the absorption spectrum of the reference is diagonal on the chip. By appropriate binning, $I_{\text{sig}}(\omega)$ and $I_0(\omega)$ can be read out from the camera signal and one can calculate the $OD(\omega)$.
More technical details on the beamline in operation without the external beam path can be found in [44, 46].

4.4 Stability Analysis

Physically, the two beam paths for the NIR are nothing else than two arms of an interferometer. Interferometers are sensitive tools, which can very precisely measure length differences in the two arms. The sensitivity can even be raised to a level which is enough to record signal from gravitational waves [49].
In the ATAS setup, no length differences shall be measured. However, the length difference corresponds to the time delay of the NIR and XUV pulse in the experiment. Thus, there are two requirements:

- To obtain a temporal pulse overlap, the two arms of the interferometer must have

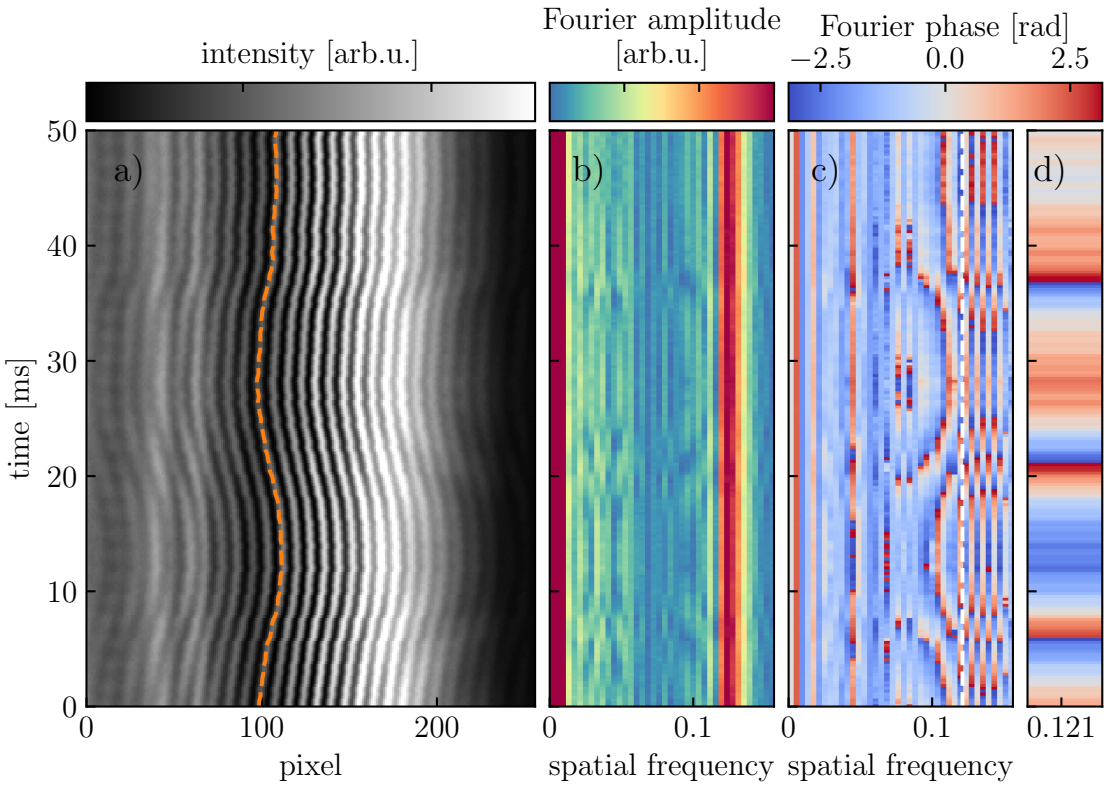

Figure 4.3: Reconstruction of the interference pattern phase
a) One line of the camera picture stacked for 200 consecutive images (4000 fps). The orange dashed line corresponds to the phase of d). **b)** and **c)** The Fourier transform amplitude and phase of a) along the pixel axis. The white dashed line marks the position of the strongest amplitude. **d)** Phase of the strongest Fourier component.

exactly the same absolute length. The next section discusses details about this issue.

- The length difference must be stable. If one arm changes its length by 300 nm, this would already be a temporal displacement of 1 fs.

To measure the latter, the beam path of the NIR was overlaid by a continuous wave helium neon laser (HeNe). This has the advantages, that the first requirement has not to be fulfilled and for monitoring with a camera arbitrary integration times can be used independent of the repetition rate. Additionally, the wavelength is well-defined, which produces more distinct interference fringes. After the toroidal mirror, the beamline allows to outcouple the recombined NIR or HeNe beams. A fast camera is in this case able to monitor the interference pattern. To obtain straight interference fringes, the angle of the external beam can be slightly misaligned.

Figure 4.3a) shows the measured interference pattern changing with time. 4.3b) displays the amplitude of the Fourier transform along the spatial axis. Except for the DC peak, there is a clear maximum at $f_{\max} = 0.12 \frac{1}{\text{pixel}}$. The Fourier phase $\phi(t)$ at this frequency, shown in 4.3d), is equivalent to the phase difference introduced in the two arms. The wavelength of the HeNe is $\lambda_{\mathbf{HeNe}} = 632.8\,\text{fs}$, which corresponds to an optical period of $T_{\mathbf{HeNe}} = 2.111\,\text{fs}$. Hence, the phase evolution can easily be translated to an effective

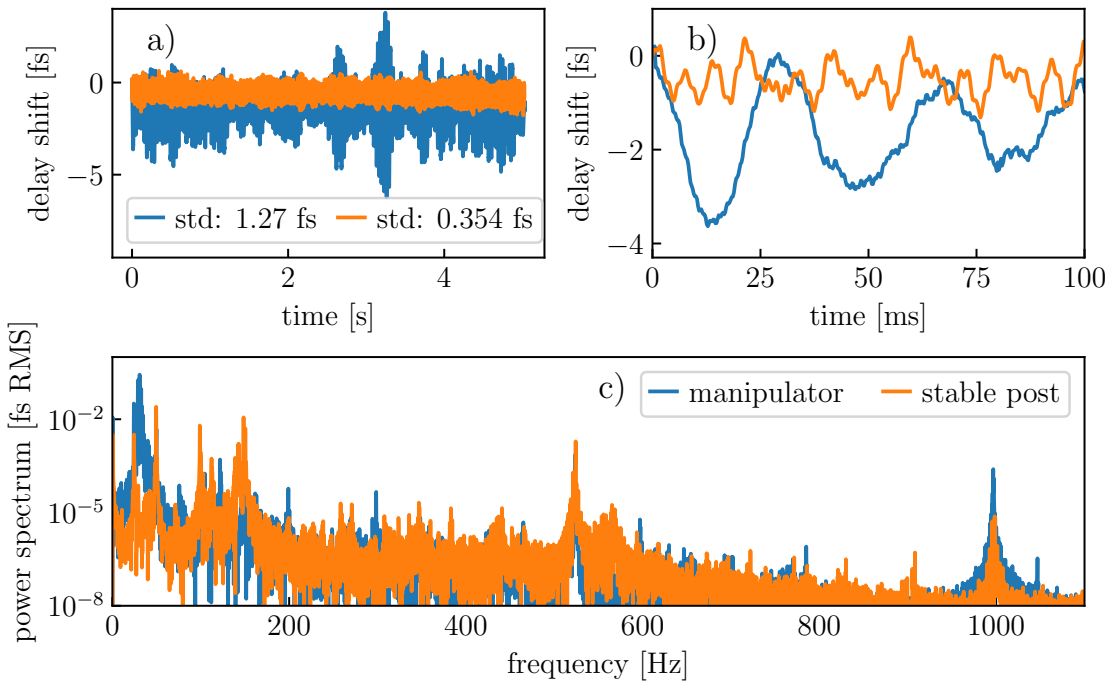

Figure 4.4: Delay jitter of the external beam path for two methods to mount the hole mirror
a) The change in delay monitored for 5 seconds with 4000 fps. The legend shows the standard deviation for all data points. **b)** Magnification of a) to the timescale of the oscillation. **c)** Power spectrum of a). For all figures the blue (orange) data denotes the case for mounting the hole mirror on a 3-axis manipulator (stable post).

time delay jitter

$$\text{delay}(t) = \phi(t)\frac{T_{\mathbf{HeNe}}}{2\pi}. \tag{4.2}$$

It should be noted, that for an unambiguous reconstruction of the jitter, the camera has to sample sufficiently fast. If there is a phase jump bigger than π between two images $\Delta\phi > |\pi|$, the phase unwraping algorithm will interpret it as $\Delta\phi_{\text{reconstruct}} = -\text{sign}(\Delta\phi)\,(2\pi - \Delta\phi)$.

Figure 4.4 shows the resulting delay jitter traces for two configurations of the mirror installation. The first design consists of a 3-axes manipulator (see Figure 4.5a). It allows to move the mirror in and out of the beam without breaking the vacuum and it supports easy lateral alignment. However, this assembly is not very stable. It leads to strong delay modulations. Measured over 5 seconds, the phase jitters corresponding to a standard deviation in delay of 1.27 fs. The power spectrum reveals, that the main frequency of the noise is at ~ 30 Hz. The peaks at 525 Hz and 1000 Hz correspond to the frequencies of the turbopumps which validates the reliability of the measurement and reconstruction method. The strong fluctuations would make it impossible to see any sub-cycle oscillation, which is expected to be mainly present at twice the NIR frequency, which corresponds to a period of ~ 1.2 fs.
Hence, a different design was implemented with focus on improving the stability, displayed

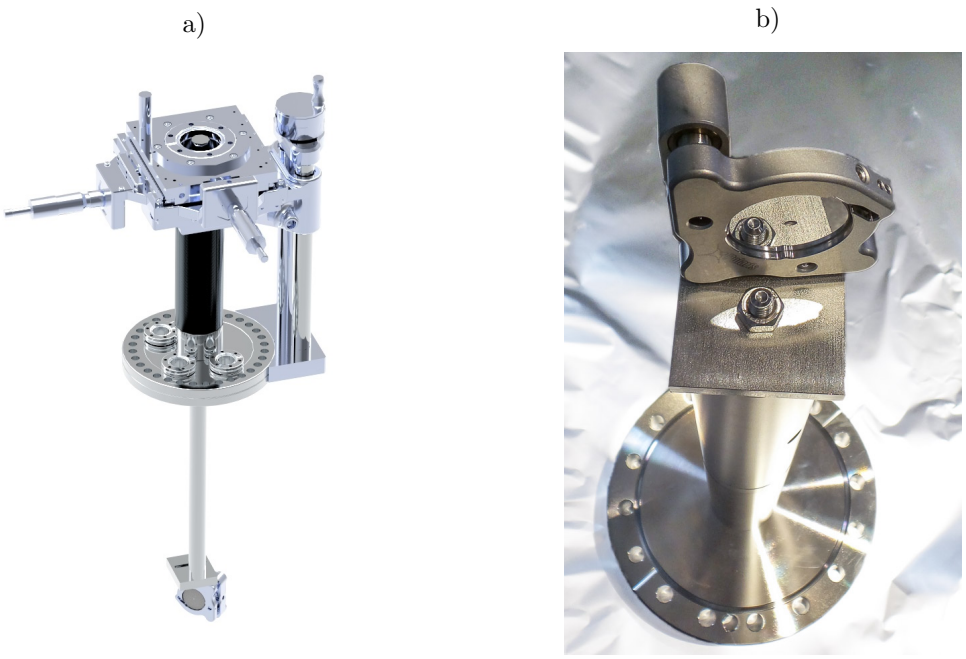

Figure 4.5: Two methods to install the hole mirror
a) A 3-axes manipulator. **b)** Picture of the mirror mounted on a stable post which is fixed to the flange.

in Figure 4.5b). The main changes are getting rid of all three manipulators, shortening the main rod by nearly 50 % and doubling the diameter of the rod to 1 inch. The delay jitter trace reflects this improved stability. The standard deviation over 5 seconds decreased to 0.354 fs. The strongest frequency components are now at 50 Hz and 150 Hz. One should bear in mind, that between the stability measurements of the two assemblies one month has passed. Some parts of the noise might have been changed due to different operation of other lab equipment. But the disappearance of the ~ 30 Hz noise can most likely be attributed to the different mirror mount.
Of course this enhancement in stability comes with a price, which is less flexibility and much harder alignment of the hole mirror [1]. The stability is better for the single post, but it is far away from being perfect.

Figure 4.6 shows an estimation how the instability effects the $2\omega_0$ feature. Therefore, an oscillation with period $T = 1.2$ fs is convolved with a Gaussian with the measured standard deviations. For the manipulator mounting instability the oscillation averages out completely. The single post installation reduces the amplitude of the oscillation to 18 %. Although, the modulation is still visible in this figure, it might not be enough to register the $2\omega_0$ feature in the measurement. The delay distribution is not perfectly Gaussian, no long term drift was taken into account and the signal to noise ratio might be too bad, to observe the oscillation.

[1] The alignment procedure is described in Appendix D.

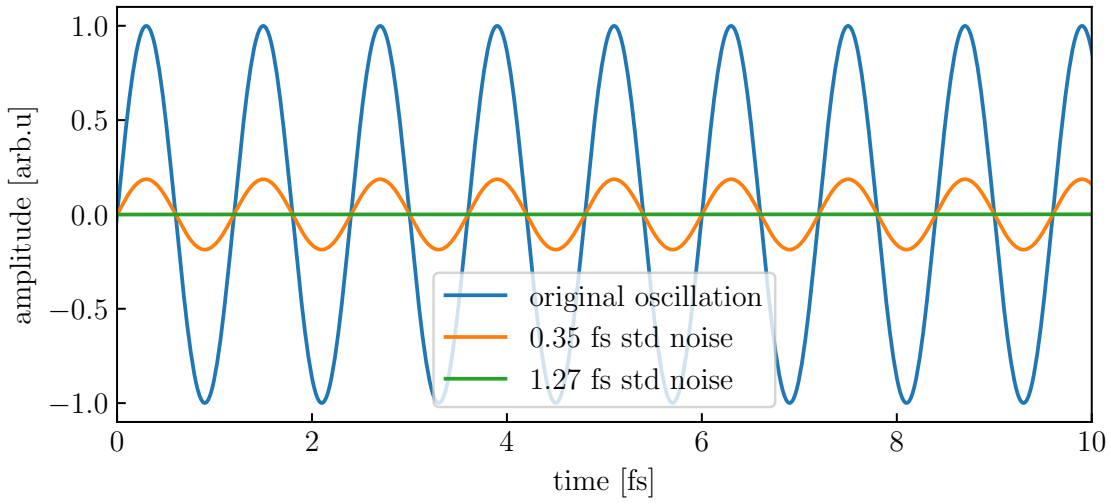

Figure 4.6: Suppression of a $T = 1.2\,\text{fs}$ oscillation with noise
The orange (green) curve shows the blue oscillation convolved with a Gaussian with width 0.35 fs (1.27 fs)

4.5 Temporal Overlap of XUV and NIR

One of the biggest challenges, working with the external NIR beampath, is to achieve an overlap of NIR and XUV in the target in all three spatial and the temporal dimension. Section D gives a procedure to obtain the spatial alignment. Here, three techniques to determine the temporal overlap are discussed.

4.5.1 NIR-NIR Interference Pattern

The basic idea of the first method is to monitor the two NIR beams after recombination on a camera. Only if the temporal delay is within the pulse length, interference fringes can be observed. The interference pattern can be quantified using a Fourier transform. By scanning the delay with the piezo driven delay stage the position with the strongest interference pattern can be found and interpreted as zero time delay. Figure 4.7 gives an overview of the technique. In the trace of 4.7c), the strength of the interference pattern does not only show one peak, but one dominant peak and two side peaks. Probably this is due to a post or prepulse 30 fs away from the main peak. The dominant frequency of the interference pattern shifts during the main peak. This can be an indication, that at least one pulse is chirped. Thus, in principle this method does not only allow to determine the zero time delay position of the piezo but pulse characterization, as well. One has to note, that the technique works best if there are many fringes, hence when the two NIR beams overlap with an angle. Correcting the angle for the measurement will change the time delay again. However, this is a good technique to get a coarse idea of the temporal overlap.

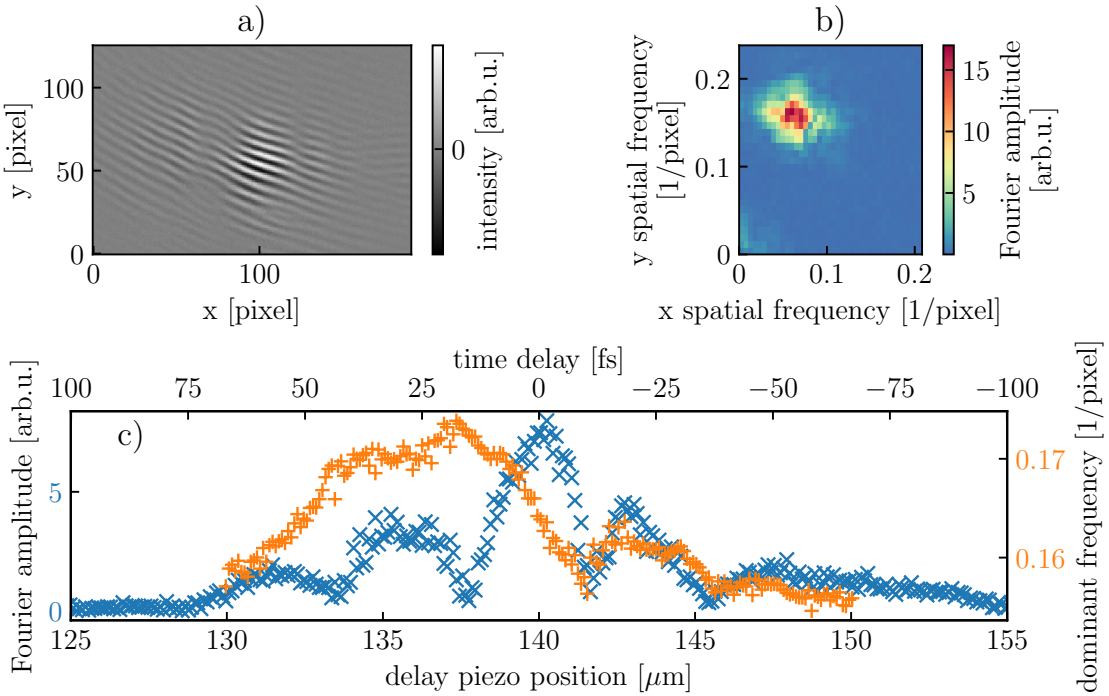

Figure 4.7: Technique to determine temporal overlap
a) Camera picture with the background subtracted at zero time delay. **b)** Amplitude of the 2-dimensional Fourier transformation of the camera picture. **c)** Delay dependent Fourier amplitude at $f_x = 0.042\,\frac{1}{\text{pixel}}$, $f_y = 0.151\,\frac{1}{\text{pixel}}$ (blue crosses) and position of the dominant absolute frequency (orange pluses). It was calculated as center of mass of the peak in b). Zero time delay is set to 140 μm piezo position.

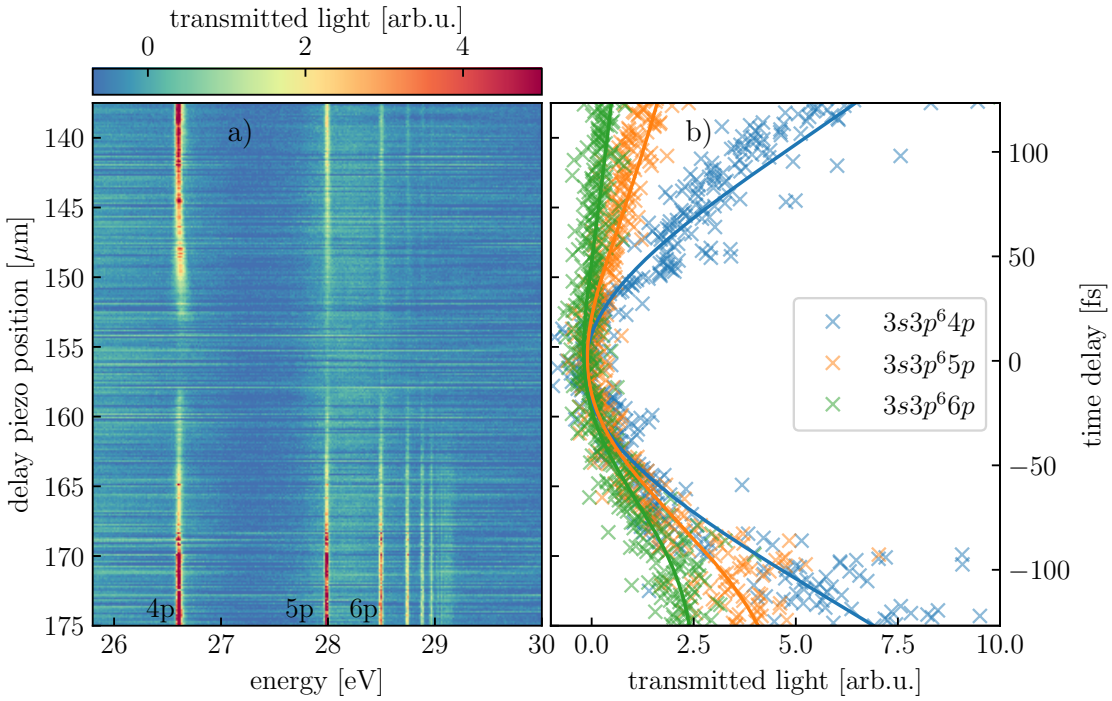

Figure 4.8: Time delay dependent transmitted light in argon
a) Transmitted light of the autoionizing states in argon dependent on the delay piezo position. **b)** Lineouts of the 4p, 5p and 5p states marked in a) (crosses). The solid lines are fitted Gaussian functions convolved with an exponential. Zero time delay is set to 156 μm piezo position.

4.5.2 Vanishing Argon Lines

To determine the exact temporal overlap of NIR and XUV in the target, the absorption of the argon autoionizing states can be studied as in [43].
Figure 4.8 displays a time delay scan of the transmitted light through argon. In the temporal overlap the resonances resulting from the autoionizing states disappear, because the states are immediately ionized by the NIR after excitation. Figure 4.8b) displays the lineouts of the transmitted light for three different states together with a Gaussian $*$ exponential fit as guide to the eye. For the presented data the maximal NIR intensity is in the order of 10^{14} W/cm^2 and therefore two orders of magnitude higher than in [43]. This is the reason, why the transmitted light is diminishing to zero for a large delay range, which makes it not possible to determine the pulse width and the lifetime of the states. By taking the data with a reduced intensity (closing the iris), this can be achieved, as well. Here, the main interest is on the absolute minimum of the transmission curves, which determines the best temporal overlap of NIR and XUV.

4.5.3 Fitting of the Reconstructed Dipole's Phase

The third option is the most unconventional one. It uses the phase of the reconstructed dipole response of a bright state to determine the absolute time overlap out of an absorp-

tion spectrum delay scan. Its principle is the following:
Let's look at the state $\Psi_\mathrm{a}(t)$ with the energy ω_a. Its time evolution is given by $\Psi_\mathrm{a}(t) = \Psi_\mathrm{a}(0) \cdot e^{i\omega_\mathrm{a} t}$, thus the dipole moment to the ground state Ψ_0 without any NIR pulse is:

$$d_\mathrm{noNIR}(t) = \langle \Psi_\mathrm{a}(t)|x|\Psi_0\rangle \tag{4.3}$$

$$= \langle \Psi_\mathrm{a}(0)|x|\Psi_0\rangle \cdot e^{i\omega_\mathrm{a} t}. \tag{4.4}$$

Now, we consider a short, strong laser pulse with the intensity envelope $I(t)$ interacting after excitation, which can alter the energy of state Ψ_a to:

$$\omega(t) = \omega_\mathrm{a} + \Delta\omega(t). \tag{4.5}$$

In general $\Delta\omega(t)$ is known as AC stark shift. For a high-lying Rydberg state it can be approximated by the ponderomotive energy U_p [31]. The dipole moment to the ground state, which itself is not affected significantly by the pulse, changes to:

$$d(t) = \langle \Psi_\mathrm{a}(0)|x|\Psi_0\rangle \cdot e^{i\int_0^t \omega_\mathrm{a} + \Delta\omega(t')\mathrm{d}t'}. \tag{4.6}$$

We focus then on the difference of the dipoles' phases, more precisely on its time derivative:

$$\arg(d(t)) - \arg(d_\mathrm{noNIR}(t)) = \int_0^t \Delta\omega(t')\mathrm{d}t' \tag{4.7}$$

$$\frac{\mathrm{d}}{\mathrm{d}t}\left(\arg(d(t)) - \arg(d_\mathrm{noNIR}(t))\right) = \Delta\omega(t) \tag{4.8}$$

If we assume, that maximal intensity will lead to a maximal energy shift, we can thus read out the center of the pulse. This is a reasonable assumption. In the case of a pure ponderomotive shift $\Delta\omega(t)$ is even proportional to $I(t)$.

Figure 4.9 shows the realization of this technique with experimental data. The alignment differs from the one used for the argon absorption scan, thus the absolute piezo positions are not comparable. Subfigure a) displays the optical densities of helium's Rydberg series, which was measured with the above described setup for different NIR intensities. The experimental retrieval does not work if the absorption spectrum without any external NIR light is used. Instead the spectrum with the weakest NIR intensity measured ($\sim 10^{11} W/cm^2$) is taken as a reference. There are two possible reasons why the technique fails for the reference completely without external NIR light. Firstly, the finite spectrometer resolution does not allow to resolve the peak sufficiently if it is not broadened by NIR light. Secondly, without any NIR light, which is delayed in the external path, the leakage of the NIR that has generated the high-harmonics dominates and can change the dipole. The window, which determines for which part of the spectrum the dipole is reconstructed is set on the 1s4p peak. It is a super-Gaussian of order 4 centered at 23.73 eV with 0.1 eV width. The reconstructed dipole's phase difference of the moderate and the weakest NIR is shown in Figure 4.9 b). The validity of the phase reconstruction has been shown in [6]. The behavior of the phase changes around piezo position 193 μm differ significantly from the rest of the delays which already indicate, that this is the region of the temporal

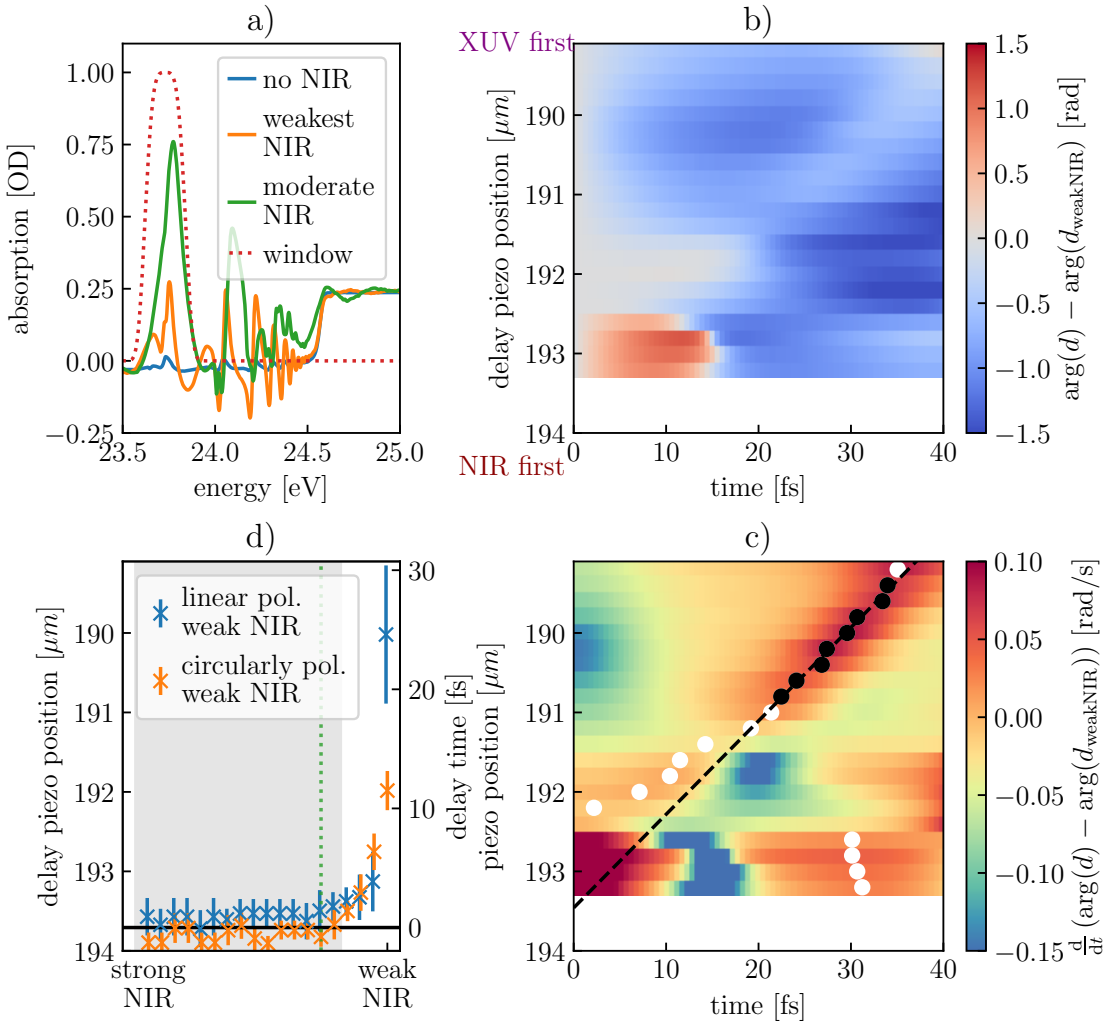

Figure 4.9: Reconstructing the absolute time delay with the dipole phase
a) The absorption spectrum of helium perturbed with a NIR at 18 fs delay. The window cuts out the 1s4p peak, whose dipole moment is reconstructed. **b)** The dipole phase of the absorption spectra with moderate NIR minus the phase of the spectra with the weakest NIR for different delays. **c)** The derivative of the quantity of b) with respect to time. The local maxima are marked. The black markers indicate the values which are taken for a linear fit (dashed line). **d)** Fit values of the intercept for different NIR intensities (scale is not linear). The technique was carried out for two different weak NIR fields as reference (linear and circularly polarized). The gray area indicates the region which was taken to calculate the weighted average (black line at 193.7 μm) over all intercept fit values. The green dotted line displays the NIR intensity shown in b) and c).

overlap. When XUV and NIR act simultaneously on the atoms, the excitation itself is modified and the simple picture presented above, that the NIR only introduces a phase shift breaks down.
Figure 4.9c) shows the time derivative of the phase difference, which should be proportional to $\Delta\omega(t)$. The position of the peak values is marked by white and black circles. After the time overlap these maxima seem to converge to an asymptote. The maxima shown as black markers are used for a linear fit. The fit's intercept value will be defined as the temporal overlap.
This procedure is repeated for each NIR intensity measured whereby the piezo positions used for the fit are always the same. Figure 4.9d) shows the resulting fit values for the intercept. Two different sets of reference absorption spectra were used for the calculation. Once the NIR was linear polarized and once circularly at the same intensity. The polarization of the NIR light for the spectra which are not the reference doesn't matter, the same fit values are reproduced. Only the choice of the reference is important. For weak intensities, which do not differ a lot from the reference, the technique seems not to give an accurate result. But all other intensities (up to $2 \times 10^{14}\,\mathrm{W/cm^2}$) give a similar value. The weighted average over all intercepts of both reference spectra except for the weakest four intensities is $193.7\,\mu$m.
This value does not only depend on the reference spectrum, but it is as well sensitive on the choice of the exact window function. For slightly different window parameters the value changes in the range of $\pm 0.3\,\mu$m which corresponds to an uncertainty in time of ± 2 fs. For all results presented in the next chapter, this calibration of the absolute time delay zero is used.

4.6 Long Term Drifts in Delay

The data shown in the next chapter was measured over a time of 10 h. During this time, the temporal overlap was slightly shifting because of thermalization of the optics. The absorption spectra were measured for different time delays with an integration time of 3 s. One time delay scan took about 1.5 min. They were done for 20 different NIR intensities, thus a full scan took ~ 30 min. To compensate for possible systematic drifts other than time delay, circular and linear NIR polarization was switched several times. Additionally, in the analysis it has been checked that the features which will be discussed in the next chapter do not change significantly for different scan numbers.
The method to determine the long term drift is to compare a reference time delay scan with delay shifted versions of the time delay scan in question. Each examined intensity has its own reference time delay scan for each NIR polarization. The comparison is done with the euclidean norm. To find the best agreement the mean square error (MSE) has to be minimized

$$MSE(\text{shift}) = |OD(\omega, \tau, \text{shift}) - OD_{ref}(\omega, \tau)| \tag{4.9}$$

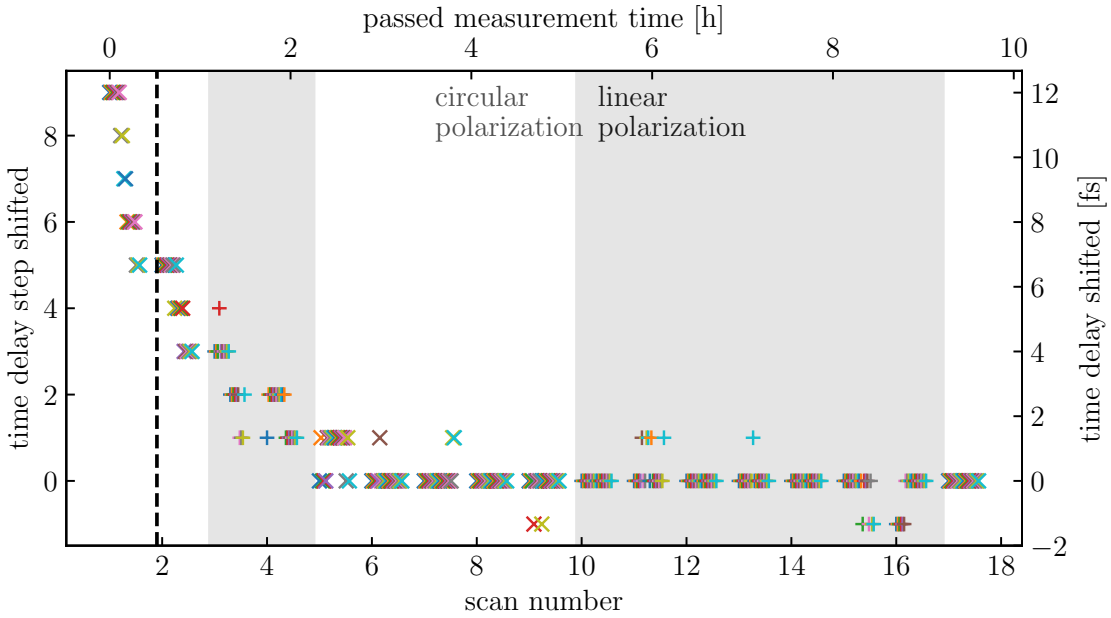

Figure 4.10: Long term drifts of the time delay
Each marker (crosses for circular NIR polarization in white area, pluses for linear NIR polarization in gray area) corresponds to one time delay scan. The color represents different NIR intensities. The time delay drift was registered by minimizing the mean square error between shifted time delay scans of same intensity. The reference is scan number 8 and 14 for circular and linear polarization respectively. The scan number 1 left of the dashed line was excluded from the further analysis.

This method seems to be robust. Using a different norm to compare the images (the structural similarities index [50]) reproduces the results excellently. A cross-correlation method has been tried as well, but was found to yield unsatisfying results. As a caveat of this method, the delay shift can only be determined in units of the scanned time step, which is 1.33 fs. For a further, more exact investigation of the long term drifts, this time step size should be decreased.

Figure 4.10 shows the the calculated drift for each time delay scan correlated with the passed measurement time. In the first hour of measurement the shift was about 8 fs, after three hours the equilibrium was reached with a total drift of $\sim$ 12 fs. Due to the strong drift in the beginning, the first scan is not taken into account. All other scans are shifted to overlay correctly and averaged for the analysis.

Chapter 5

Experimental Results

This chapter presents the absorption data in helium measured with the previously described experimental setup. In addition, possible explanations, interpretations and comparisons to the simulations are discussed.

5.1 Bound States and Sub-Cycle Effects

After the thermalization of the experimental setup, the transient-absorption spectrum in helium with linearly polarized, strong NIR light was measured, as shown in Figure 5.1. It was measured subsequently to the intensity-dependent scans described in section 4.6, with a longer delay range and a better time-delay resolution (step size 0.33 fs). The dashed lines in the figure indicate the time delays, for which the intensity-dependent absorption spectra, discussed in the next sections, are measured. Since the NIR is intense, there are many time-delay dependent dynamics visible. The most prominent is the disappearance of the bound state absorption lines around time delay zero, i.e., when XUV and NIR light is present at the same time. This is due to the fact, that the NIR hinders the population of the excited states, which are immediately ionized because of the strong field.

A Fourier analysis of the recorded delay-dependent spectra is displayed in Figure 5.1 b). In previous measurements, there have been many features showing a modulation with $2\,\omega_0$ (ω_0 is the central NIR frequency) in Fourier energy [17]. This can be explained by 2-photon processes in the multi-photon regime [25]. For high intensities, all field-dependent effects should exhibit the same periodicity. However, there is no clear feature visible in Figure 5.1b). The inset 5.1c) shows the lineouts of the Fourier amplitude for the 1s3p and 1s4p state. At 3.2 eV, (corresponding to $2\,\omega_0$, see Figure E.1 for a spectrum of the NIR) there is a small peak for both states, which nearly perishes in the noise. This could be a signal of sub-cycle effects. As studied in Figure 4.6, the instabilities of the setup lead to a strong decrease in the visibility of these $2\,\omega_0$ modulations. One can conclude now, that even under the best conditions (no averaging over several scans, thermalization over 10h to avoid delay shifts), the stability is only good enough to barely scratch the sub-cycle resolved regime. This means, that for the intensity-dependent data, which is averaged over several scans, no sub-cycle effects are visible.

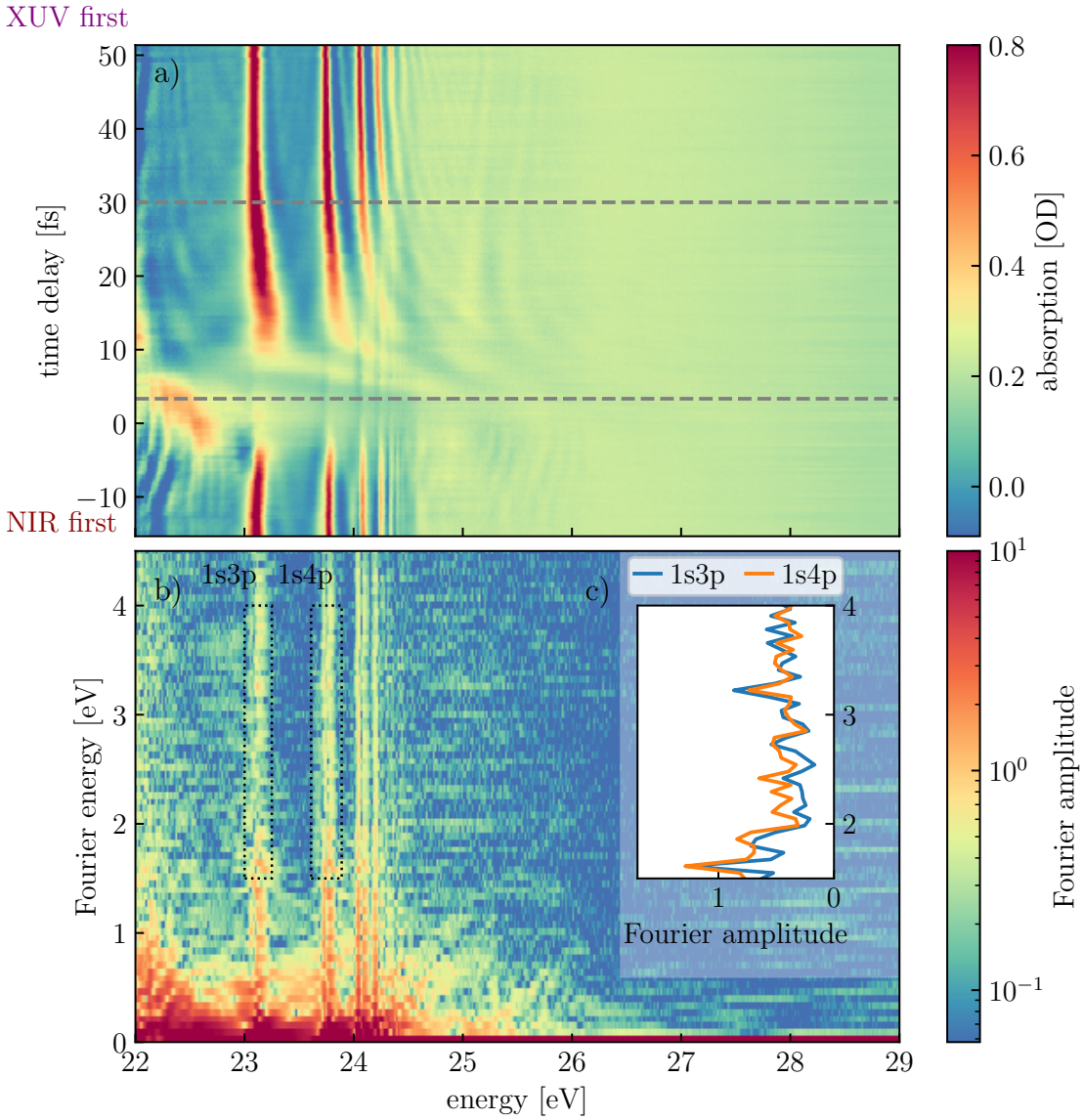

Figure 5.1: Helium absorption spectra with fine delay steps and Fourier analysis
a) Optical density of helium for a varying time delay between XUV and NIR pulses with NIR peak intensity $I_{\max} \sim 10^{14}\mathrm{W/cm^2}$. The gray dashed lines correspond to the delay range which was studied more closely (see next sections). **b)** Amplitude of a Fourier transform along the time delay axis. The black dotted boxes indicate the 1s3p and 1s4p states with lineouts of the data along the Fourier energy shown in the inset. **c)** The inset shows the Fourier amplitude of the highlighted states (integrated over a width of 50 meV at the peaks).

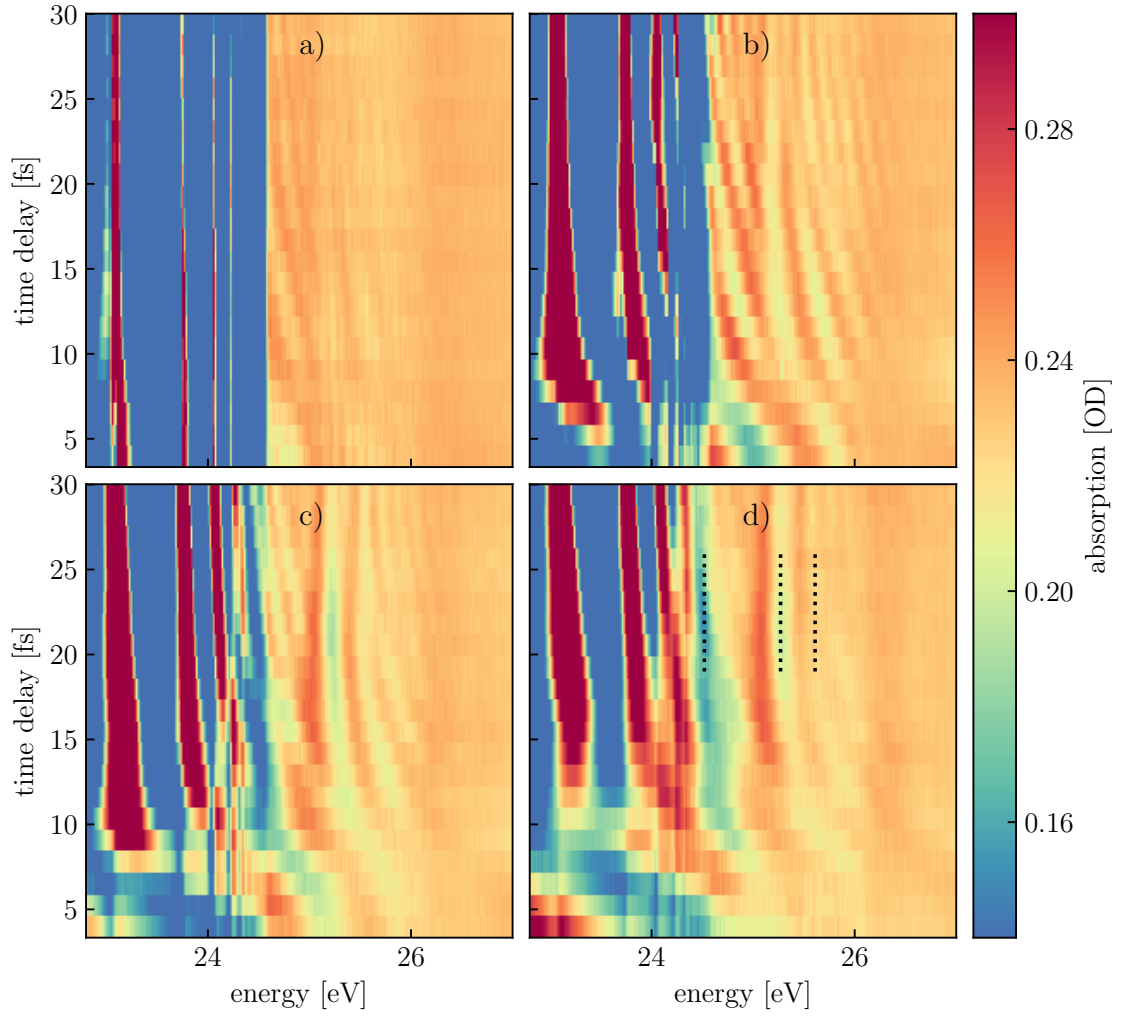

Figure 5.2: Helium absorption spectra at the first ionization potential for different NIR intensities
a), **b)**, **c)**, **d)** Optical densities for a weak to strong NIR pulse (iris positions 64, 59, 53 and 30, see Appendix E.2 for an intensity calibration) at different time delays. The dashed lines correspond to the expected energy positions of the 3s+, 4s+ and 5s+ LISs using data from [12] and assuming a light frequency of $\omega_0 = 1.6\,\mathrm{eV}$.

5.2 Intensity Dependent Structure in the Helium Continuum

The features visible at the ionization threshold and in the continuum are examined for the rest of this chapter. For different NIR intensities, the time-delay-dependent absorption spectra of helium are depicted in Figure 5.2. Subfigure a) corresponds to the weakest peak intensity measured ($I_{\max}$ is on the order of $1 \times 10^{12}\,\mathrm{W/cm^2}$) and d) to the highest ($I_{\max} \sim 3 \times 10^{14}\,\mathrm{W/cm^2}$). The observed signatures in the continuum change dramatically for the different intensity regimes. In subfigure a) there is a distinct continuum edge, which dissolves completely for higher intensities. The structure in the absorption of the continuum is faint and can best be described by hyperbolic lines. They can be understood as a result of the ponderomotive energy, which the electrons experience in the NIR light

field [17]. In Figure 5.2 b) these lines are the dominant feature, but for even higher intensities they cease again. In d) there are even peaks in the continuum which do not change significantly any more for a large time-delay range. This is an indication, that for time delays bigger than 15 fs it is not anymore the XUV which triggers the dynamics, and the NIR that perturbs it. Rather, the strong NIR pulse ionizes the Rydberg states, which have been populated before by the XUV. Thus, the NIR is probing and modulating the continuum at the same time.

Without offering a satisfying explanation, it shall be marked that the energies of the strongest features are close to those of the 3s+, 4s+ and 5s+ LISs. The nomenclature stands for light-induced states, which are one photon energy above the 3s, 4s and 5s state. Since in the continuum the LISs can be described as laser-induced continuum structure (LICS, compare section 2.5), they exhibit a Fano profile. The dotted lines in Figure 5.2c), d) mark the positions of these states assuming a central NIR energy of 1.6 eV. These lines are approximately in the center of a maximum and a minimum of absorption, especially the first two at 24.52 eV and 25.27 eV. Light-induced states have so far [25] only been observed in the pulse overlap. If the NIR itself triggers the ionization, this might be different. However, a coincidental similarity cannot be excluded. A detailed explanation of these features requires more work in theory, which goes beyond the scope of this thesis. The most interesting spectra for this work are during the temporal overlap of XUV and NIR, thus for time delays under 5 fs. This regime is studied in the next section in dependence of the light polarization.

5.3 Polarization-Dependent Spectral Features in the Helium Continuum During Temporal Overlap

To analyze spectral features in the temporal overlap, the measured spectra for a delay of 3.3 fs and 4.7 fs are averaged. This enhances statistics and potential errors of the long-term drift reconstruction (compare Figure 4.10) are averaged out.

Figure 5.3 shows intensity scans of this averaged spectrum in the temporal overlap for different NIR polarizations[1]. Both subplots are to a large extent very similar. The main feature is an apparently periodic modulation of the absorption for low NIR intensity, which shifts to higher energies for higher intensities, while becoming stronger. For the highest intensities, the modulation disappears. A possible explanation for this modulation are the LISs from the 3s, 4s and 5s states. They exhibit a Fano-like profile in the continuum (LICS) and they experience a ponderomotive shift [25]. In Figure 5.3, the expected energy positions of the relevant LISs with estimated ponderomotive shifts are marked with black lines. An attribution of the absorption features to the states is possible, especially the energy difference of the 3s+ and 4s+ state fits the observed variation period.

[1] In the beamline a 7 μm thick Kapton foil, which can be birefringent, was used as a filter. See Figure 4.1 for its position. The polarization was tuned with the $\lambda/4$ waveplate to maximize the high-harmonic generation in an argon target for the linear polarization. Circular polarization was achieved by adding 45° to the waveplate. Due to the Kapton filter, the linear and circular polarization might not have been perfect.

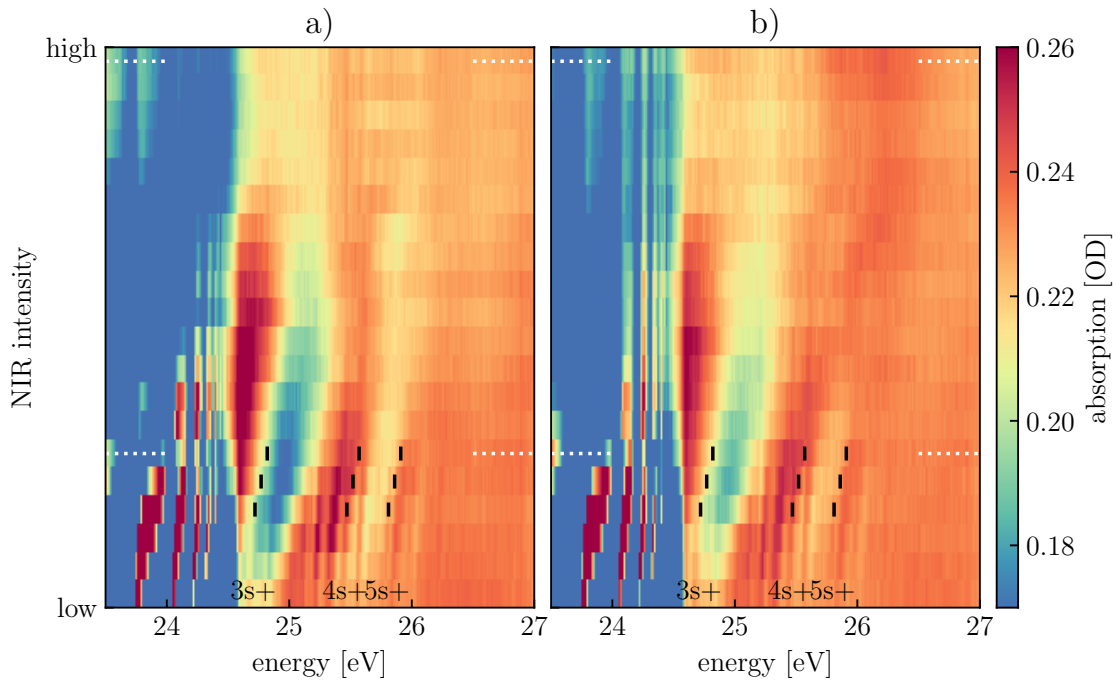

Figure 5.3: NIR intensity scan of the absorption spectrum in the temporal overlap of NIR and XUV
a) (**b**) Optical densities for a linearly (circularly) polarized NIR pulse for different NIR intensities (see Appendix E.2 for an intensity calibration) in the temporal overlap. The black lines correspond to the expected energy positions of the 3s+, 4s+ and 5s+ LISs using data from [12], assuming a light frequency of $\omega_0 = 1.6\,\text{eV}$ and a ponderomotive shift of 0.2, 0.25 and 0.3 eV with increasing intensity. The white dotted lines mark the intensities at which lineouts are plotted in Figure 5.4.

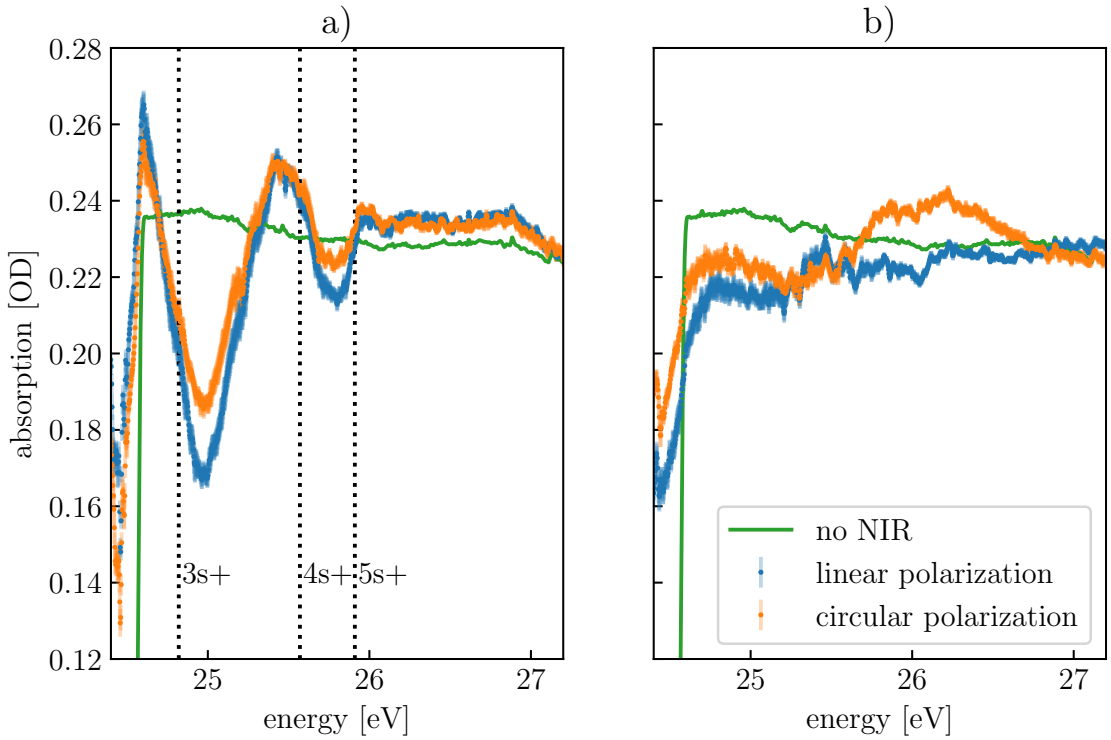

Figure 5.4: Difference of absorption spectra with linear and circular NIR polarization in the temporal overlap of NIR and XUV
a) and **b)** Optical densities for a moderate (peak intensity $\sim 4 \times 10^{13}\,\mathrm{W/cm^2}$) and a strong ($\sim 3 \times 10^{14}\,\mathrm{W/cm^2}$) NIR pulse for different polarizations. The errors show the standard deviation of the average. The black dotted lines correspond to the expected energy positions of the 3s+, 4s+ and 5s+ LISs, assuming a light frequency of $\omega_0 = 1.6\,\mathrm{eV}$ and a ponderomotive shift of 0.3 eV.

The LISs are modulated with a very fast frequency along the energy axis. This behavior is retrieved with the TDSE model for a simulation with an NIR post-pulse at 40 fs and with a fraction of the peak intensity subsequent to the main pulse. A possible explanation is, that the main NIR pulse populates the dark states during the overlap with the XUV. The delayed post pulse can afterwards ionize these states with a single photon. Thus, there are two quantum-mechanical pathways into the continuum, which interfere and produce the observed fast oscillation.

We have found an explanation for the absorption features at moderate intensity. To confirm, that the light-induced states are a proper model to describe the data in this intensity regime, it makes sense to look at the polarization dependence. There are two main differences between linear (Figure 5.3 a) and circular (5.3 b) polarization:

- The modulation at moderate intensities is stronger for linear polarization. This means higher peaks and lower minima in absorption.

- For high NIR intensities, the absorption spectra look qualitatively different. The most dominant signature is an increased absorption for circular polarization at 26 eV, while linear polarized light exhibits no peak in absorbance.

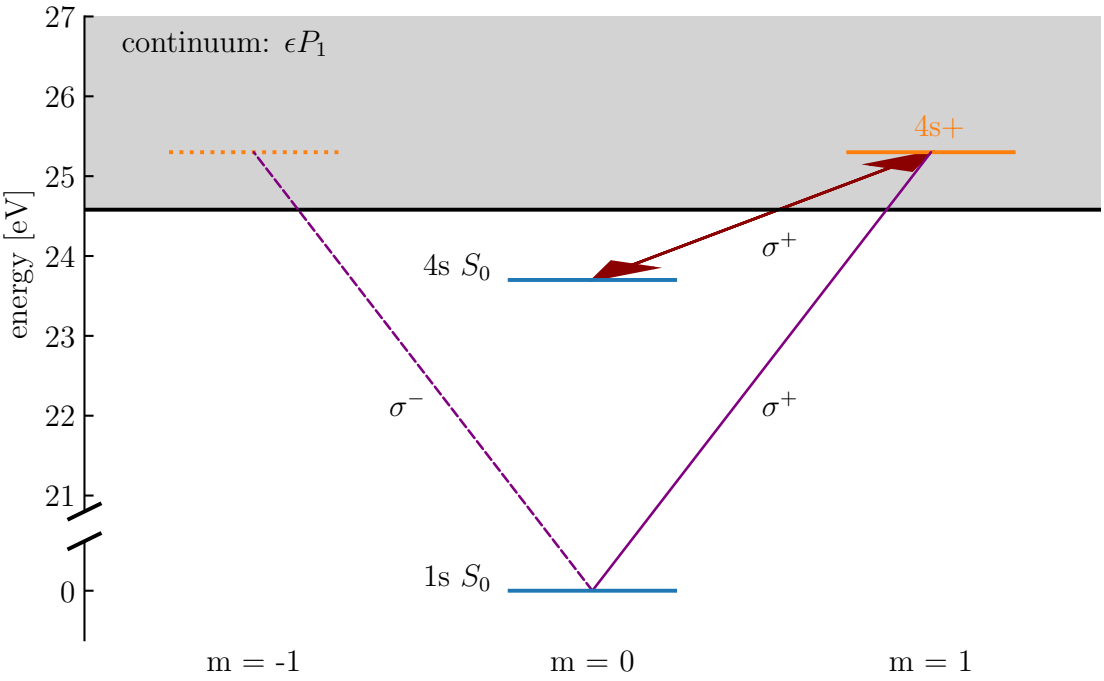

Figure 5.5: Scheme of LISs for circularly polarized NIR light
The ground and the 4s state are shown in blue. Purple lines represent the XUV excitation and the dark red arrow corresponds to the NIR interaction that embeds the light-induced state in the continuum.

These two points are emphasized in Figure 5.4 for the moderate intensity regime in subplot a) and for high intensities in b). Additionally, the energies of the LISs, assuming a light frequency of $\omega_0 = 1.6\,\text{eV}$ and a ponderomotive shift of $0.3\,\text{eV}$, are depicted with dotted lines. One has to keep in mind, that the light spectrum is not Gaussian (see Figure E.1), the shape of a Fano line depends on its q parameter and that the states will experience slightly different AC Stark shifts. Furthermore, the states are due to the broad spectrum overlapping. Thus, the data does not show distinct Fano lines. The estimated energy positions of the 4s+ and 5s+ LISs are on the falling edge of the absorption spectrum, which would correspond to a q parameter of approximately -1.

How to explain these different amplitudes of modulation for linear and circular polarization? In an experiment of Maurizio Reduzzi et al. [51], the delay-dependent absorption spectra for linear polarized NIR light was studied for parallel and perpendicular NIR polarization with respect to the XUV. They observe, that for a perpendicular polarization, no LISs corresponding to s-states are visible. Although not commented, in their data the 3s+, 4s+ and 5s+ LISs for an NIR polarization parallel to the XUV remind of Fano lines with a negative q parameter, i.e. a minimum follows a maximum. This is comparable to the presented data in this chapter.

To get a better understanding of the strength of the LISs for circularly polarized NIR light, Figure 5.5 displays a scheme of the emergence of the 4s+ (3s+ and 5s+ are alike). The linear XUV pulse can be seen as a superposition of σ^+ and σ^- light. The circularly polarized NIR (assumed to be σ^+ without loss of generality) embeds the 4s state ($m = 0$)

into the ϵp continuum with $m = 1$. If the XUV probes the continuum at $m = \pm 1$, only the σ^+ part of the light sees a structured continuum. Since the absorbance for σ^+ light is modulated but not for σ^-, the transmitted XUV will no longer be linear but slightly elliptically polarized. In the visible and ultraviolet regime this change of the polarization has been measured for LICS, e.g. in sodium [52], CsI [33] or helium [35]. To stay in this picture: in the case of linear polarized NIR light, the σ^- part of the XUV probes a structured continuum as well. Thus, the absorption structure caused by the 3s+, 4s+ and 5s+ light-induced states is stronger for linear than for circularly polarized NIR.

This explains the continuum absorption spectra in the temporal overlap for moderate intensities, corresponding to the lower half of Figure 5.3. Therefore, the concept of light-induced states is suitable to describe the absorption features in this intensity regime. The next section will discuss the data measured at high intensities.

5.4 Reconstructed Dipole Response in the Temporal Overlap for High NIR Intensities

The absorption spectra for linear and circular NIR polarization are qualitatively different in the high-intensity regime. The most distinct increased absorbance at 26 eV for circularly polarized light is an energetically broad feature from 25.5 eV to 26.5 eV. This is a hint, that the change of the dipole moment which is responsible for this absorption feature happened on short timescales. As introduced in Section 1.9, the dipole response of the atomic system can be reconstructed solely with the measured absorption spectrum, if the excitation can be treated as instantaneous. Due to the short XUV pulse length ($\ll \frac{1}{\omega_0}$), this approximation is justified and the system can be studied in the time domain. For the absorbance data from Figure 5.3 the reconstruction is done in Figure 5.6. It shows the influence of the NIR light on the absolute reconstructed dipole moment. The used spectral window (depicted in subfigure a) is an asymmetric $\cos^2$ function (definition in Appendix A.1). It opens at 24.6 eV, peaks at 25 eV and closes until 28 eV. Its form assures, that the sharp edge at the ionization threshold itself is not part of the analysis. The reconstructed dipole moment of the absorption spectrum without NIR (subfigure b) is subtracted from the reconstructed dipoles with NIR light to enhance the visibility of the features. For moderate intensities (lower half of subplots 5.6 c and d), the difference of linear and circular polarization is mainly quantitative. On the other hand, for high intensities qualitative changes arise (emphasized by the dashed rectangles). The most interesting features are those which appear below 6 fs. Since time 0 fs depicts the time of the XUV pulse, the first six femtoseconds are the instants directly after ionization, when the electron is still in the vicinity of the atom.

To get a more quantitative idea of the differences for linear and circular polarization, Figure 5.7 shows lineouts at the marked intensities. In subfigure a), depicting the case of moderate intensity, the differences for circular and linear polarization are only quantitative. There is no obvious interpretation of the observed shape, but the features could already be well explained in the spectral domain with LICS in the previous section. For the higher

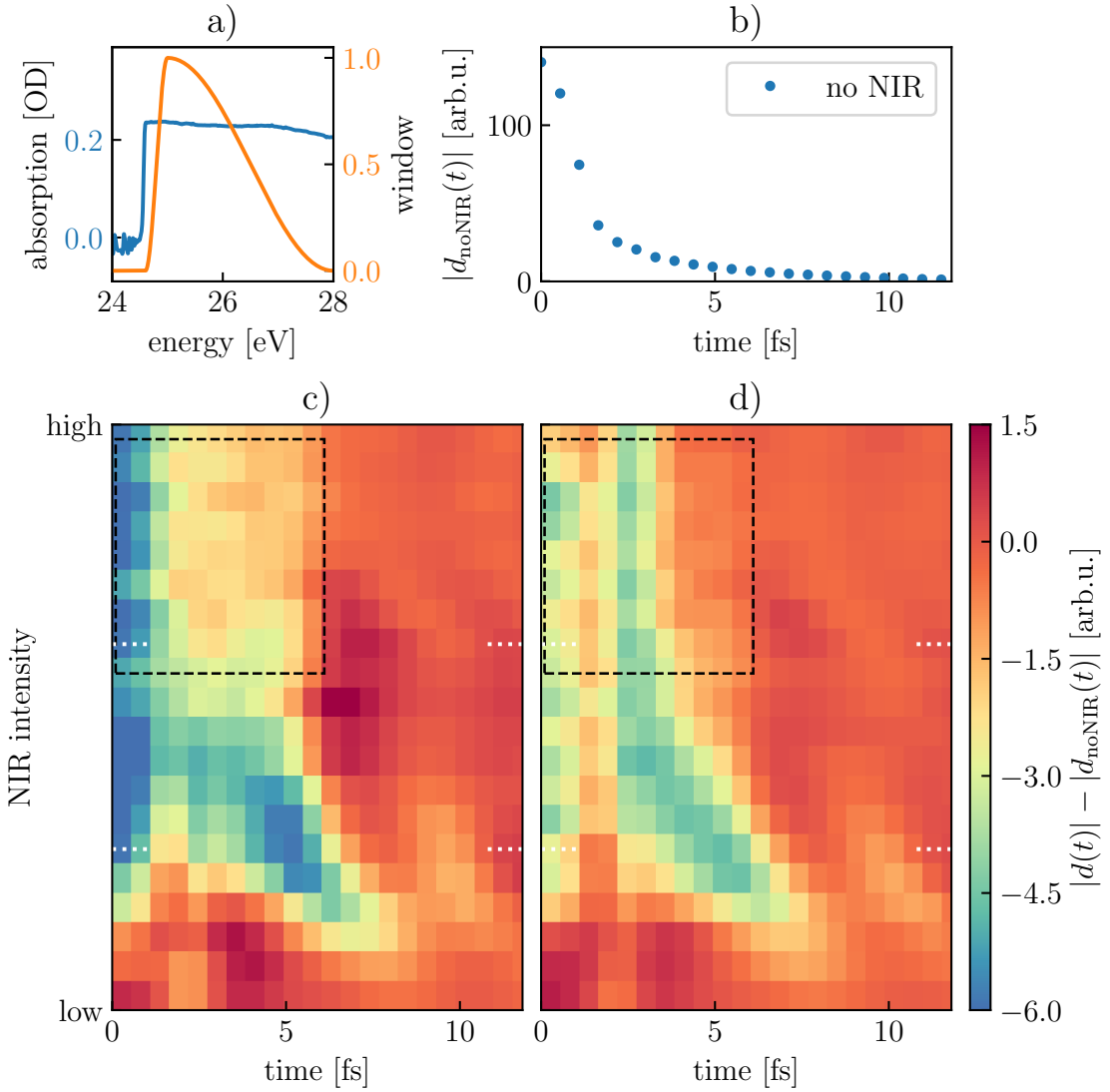

Figure 5.6: Reconstructed dipole moment of the continuum response dressed with linear and circularly polarized NIR with different intensities
a) The absorption spectrum without NIR light (blue) and the spectral window (orange), which selects the energy range studied in the time domain. **b)** The reconstructed dipole moment of the continuum without any NIR light. **c)** Difference of the absolute value of the reconstructed dipole moment for linearly polarized NIR light and without any NIR for different NIR intensities in the temporal overlap. **d)** Same as c) but with circularly polarized NIR light. The black dashed rectangles indicate the region with qualitatively different behavior for circular and linear polarization in the high-intensity regime. The white dotted lines mark the intensities plotted in Figure 5.7.

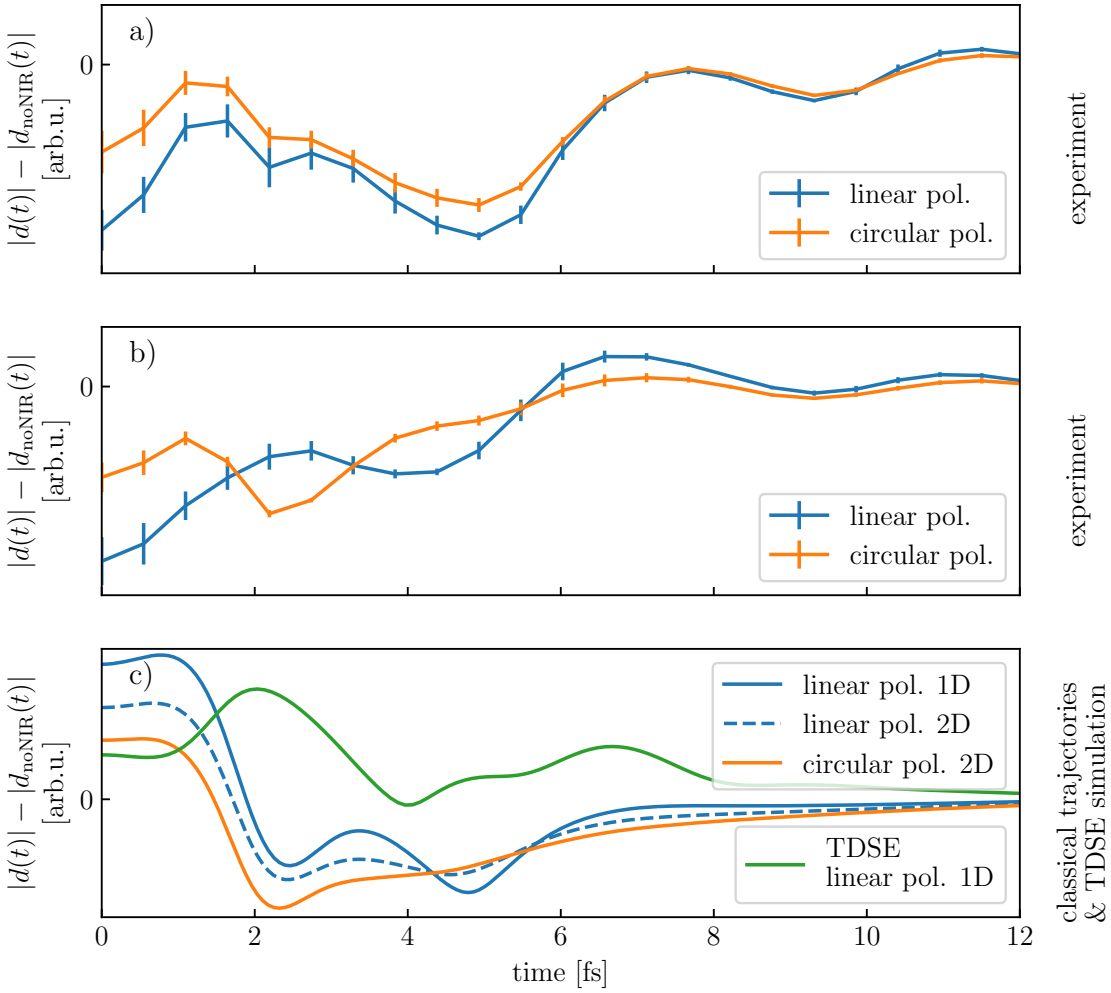

Figure 5.7: Polarization differences of the continuum dipole response for experiment and simulation
a) Difference of the absolute value of the reconstructed dipole moment with and without NIR light for moderate NIR intensity in the temporal overlap. The peak intensity is approximately $4 \times 10^{13}\,\mathrm{W/cm^2}$ (iris positions 59 in Appendix E.2). The window used for the reconstruction is given in Figure 5.6 a). The errors are standard deviations of the mean, neglecting the error on the dipole moment without NIR. **b)** Same as a), but higher NIR peak intensity of $\sim 1 \times 10^{14}\,\mathrm{W/cm^2}$ (iris positions 52). **c)** Difference of the absolute value of the reconstructed dipole moment with and without NIR light for a simulation with classical trajectories and the TDSE result. For the classical trajectories, the data is taken from Figure 3.11 part 3), thus the reconstruction window is the same as for the experimental data. The intensity is set to $4.4 \times 10^{13}\,\mathrm{W/cm^2}$. To account for the missing sub-cycle stability in the experiment, the spectra from the theory were cycle-averaged at time delay 3 fs before calculating the dipole moment. Note that the relative strength of $|d(t)| - |d_{\mathrm{noNIR}}(t)|$ for linear and circular polarization calculated with classical trajectories in c) agrees well with the experimental relative strength in b) for $t > 2.5\,\mathrm{fs}$.

intensity of Subfigure 5.7 b) no interpretation in the spectral domain was found. The influence of the NIR light on the dipole moment in this regime is strongly dependent on the polarization. For circular polarization, there is a clear minimum at ~ 2.5 fs and then the curve raises monotonously until 8 fs. For linear polarized light, one can observe a maximum at 2.5 fs, a minimum at 4 fs and another maximum at 6.5 fs. A satisfying model in this intensity regime should offer an intuitive explanation of this strong polarization dependence in the first few femtoseconds after ionization. In the following, it will be pointed out, why classical electron trajectories are a suitable model, which can fulfill this requirement.

Subfigure 5.7 c) shows simulation results of Chapter 3. With 20000 classical electron trajectories a dipole moment is constructed for different cases (i.e. different NIR polarization and dimension, compare Figure 3.11 3). Using this dipole moment, the absorbance is calculated. Out of the absorption spectrum the displayed dipole moment is reconstructed with the same window as for the experimental data. This ensures that the same quantity is compared for both experiment and theory. Only the inability of the experimental method to detect sub-cycle structure has to be added artificially to the simulated data by taking the average absorption spectrum over half an NIR cycle.

The resulting NIR-induced changes of the absolute dipole moment show a stunning agreement with the experimental data, except for the first two femtoseconds. For circular NIR polarization, there is a minimum at 2.3 fs and then the curve decreases slowly to zero. For linear polarization, a maximum appears at 3.3 fs then the value drops until 4.7 fs and for 7 fs there is again a maximum above the curve for the circular case. The electron trajectories calculated in two dimensions show all these features extenuated in comparison to the one-dimensional simulation. This is a direct consequence of the reduced 'recollision' probability in two dimensions, i.e. the electron wave packet has less overlap with the ground state, when driven back, because the velocity component transversal to the field hinders this 'recollision'.

Of course, experiment (5.7b) and simulation (c) do not agree perfectly, but this is also not expected due to the reduced complexity of the model. For the first two femtoseconds, it is most important how the ionization process is treated. Simply freeing the electron at the origin at $t = 0$ with an arbitrary velocity distribution does not satisfy the quantum-mechanical reality. In addition, for this regime the model is most sensitive to changes in the parameters (dispersion, initial velocity, size of distribution). Another source of error is the calculation of the classical trajectories in SFA, i.e. without any atomic potential included. In Chapter, 2 Figure 2.17 shows, that for the simulated intensity, the classical electron trajectories can differ significantly, whether calculated with or without an atomic potential. Additional error sources are the uncertainties of the time delay and of the experimental field intensities. This makes it even more remarkable, that without tuning of the simulation parameters (the experiment was done afterwards), the data exhibits this degree of similarity to the classical calculations.

For completeness, Figure 5.7 c) includes additionally the calculation with the TDSE model for the same parameters as the classical simulation. The positions of the peaks and

minima agree well with the experimental results, only their relative and absolute height and the data for the first femtosecond differ significantly. Since simulating circular light in one dimension is not feasible, the direct comparison of the dipole for linear and circular polarization is not possible. A two-dimensional TDSE simulation is computationally much more costly because the total grid points are squared.

To sum up, for high intensities, the continuum absorption spectra in the temporal overlap of XUV and NIR could be explained in the time domain. The evolution of the electron wave packet is sufficiently modeled as a classical trajectory, which depends strongly on the NIR polarization. When this trajectory comes close to the nucleus again ('recollision'), the overlap of the electron wave packet and the atomic ground state increases, which leads to an enhanced electric dipole moment. This change of the electric dipole moment modifies the measurable absorption spectrum.

Conclusion

Within this thesis, the strong-field dynamics at the first ionization threshold of helium have been studied. For this reason, a transient absorption beamline has been complemented by an external beam path to separate the near-infrared (NIR) light which generates the harmonics and the part acting on the target. Additional to the intensity and time-delay control, this extension enables to easily change the NIR polarization as a control parameter.

A technique to characterize the stability of the new interferometric setup has been established, which allowed monitoring the stability of different methods to mount the recombination mirror. By this, the passive interferometric stability could be increased to 350 as standard deviation measured over 5 s limited by noise at a frequency of 50 Hz. Despite this improvement, sub-NIR-cycle structures could not be resolved in the absorption spectra. Regarding the long term stability of both interferometer arms, a drift of ~ 10 fs over the first two hours of measurement was found, afterward, the setup is stable within 1 fs.

On the theoretical side, two simulations have been developed to study the behavior of an ionized electron wave packet in the vicinity of the residual ion core potential under the presence of a moderate up to strong NIR field:

The first simulation is an *ab initio* calculation based on solving the time-dependent Schrödinger equation (TDSE) with a split-step algorithm. It uses a one-dimensional model atom with soft-core potential to calculate the electronic wave function's propagation of the helium atom in the single active electron approximation. For moderate NIR intensities (ponderomotive energy $U_\mathrm{p} \ll$ photon energy ω_0), within this model, the emergence of light-induced states (LISs), which are well studied [24, 25, 51], could be observed in the temporal overlap of the NIR and XUV. Whereas most previous work has concentrated on the description of their sub-cycle nature, here it has been emphasized, that above the ionization threshold LISs are the same as laser-induced continuum structure (LICS). As a consequence, their spectral shapes are given by a Fano profile convolved with the NIR spectrum.

For moderate NIR intensities, LISs can explain the shape of the absorption above the ionization threshold. This explanation uses the photon picture, as LISs describe the coupling between the ground state and dark states with an XUV plus an NIR photon. For high intensities ($U_\mathrm{p} \gtrsim \omega_0$), LISs cannot explain the absorption shape above the ionization threshold in the temporal overlap. The absorption spectrum is seemingly chaotically modified over a large energy range (see figure 2.17). By using the dipole reconstruction method ([6] or section 1.9) a simple explanation of these absorption spectra can still be

given – not in the energy but in the time domain. This is one key finding of this thesis.

The quantity of interest is the absolute value of the dipole response of the continuum which is perturbed by the strong NIR subtracted by the unperturbed absolute dipole response:

$$\Delta|d|(t) \equiv |d_{\text{withNIR}}(t)| - |d_{\text{noNIR}}(t)|. \tag{5.1}$$

The spatial overlap integral of the excited electron wave packet and the ground state determines the dipole moment in the XUV energy range under study. The absolute dipole moment diminishes when the spatial overlap decreases. Thus, by measuring the increase or decrease of $\Delta|d|$ over time, one is sensitive whether the ionized electron wave packet is pushed back or away from the parent ion by the NIR field. By comparing the NIR driven wave function evolution with $\Delta|d|$, one can see that each peak of the latter corresponds to increased amplitude of the wave function at the origin. Furthermore, the electron wave function evolution resembles classical trajectories of electrons in a strong field. This has motivated another theoretical study.

The second simulation was aiming at constructing absorption spectra using classical electron trajectories in strong-field approximation (SFA), which neglects the Coulomb field. This is possible by defining the absolute dipole moment as a measure depending on the distance of the classical electron position to the nucleus and the dipole's phase as the quasi-classical action. The advantage of this model is that it can give a more descriptive explanation of the electron dynamics than the *ab initio* TDSE simulation. Additionally, it is with low computational costs possible to implement a second spatial dimension, allowing for comparison of absorption spectra between linear and circular NIR polarization. A qualitative agreement of $\Delta|d|$ for times $< 4\,\text{fs}$ could be found between the classical trajectories and the TDSE simulation (compare figure 3.12).

The simulations were compared to data measured with the above described external beam path. The transient absorption spectra in the vicinity of the first ionization threshold of helium have been recorded depending on the NIR intensity and polarization (linear and circular). In the temporal overlap of NIR and XUV pulse the both described simulation approaches were able to explain the measured data.

For moderate intensities, all modulations of the absorption spectrum above the ionization potential can be attributed to the 3s+, 4s+ and 5s+ LISs, as supposed by the TDSE. Not only fit the energetic positions of these features the expected values, but the polarization dependence is the same as predicted. This means, for circular polarization the absorption features are the same in shape but smaller in amplitude than for linear light (see figure 5.5).

For high intensities, the absorption spectra cannot be explained by LISs. However, it is possible to interpret the data in the time domain, as for the TDSE simulations. The ionized electron wave packet is driven by the NIR field in the vicinity of the ionic core. This induces changes of the dipole moment, which alter the absorption spectrum. Since the trajectories fundamentally differ for linear and circularly polarized NIR (the latter hardly provokes 'recollision'), the absorption features are different for each polarization.

Out of the measured spectra, the influence of the NIR on the dipole moment $\Delta|d|$ can be reconstructed. It is in qualitative agreement with the one calculated by classical trajectories for $t > 2.5\,\mathrm{fs}$ (see Figure 5.7). The resemblance of the experimental $\Delta|d|$ with linear light to the TDSE simulation is even a bit stronger, but for the TDSE the circular polarization could not be calculated caused by the one-dimensionality of the model.

For each polarization alone, the theoretical models might only coarsely describe the experimental data. However, it is the different behavior of $\Delta|d|$ for the two polarizations which is in stunning agreement with the predictions from classical trajectories.

The next experimental challenge on this topic will definitely be to enhance the stability of the interferometric setup. If the main noise source is found and neutralized or at least attenuated, sub-NIR-cycle stability is possible. As the 'recollision' effects are strongly dependent on the field's phase, all absorption features and thus the modulation of $\Delta|d|$ will be much more distinct. It would even be possible to implement active stabilization in a closed-loop scheme. With such an improvement the long term drift could completely be compensated for.

In further theoretical studies, the TDSE simulation can be extended to two or even three dimensions. This would allow comparing the difference between circular and linear polarization for the *ab initio* calculation, as well.

Additionally, it is very interesting to go beyond SFA for the classical trajectories calculation. Then, one could compare the predictions of both simulations with and without Coulomb potential and observe the breakdown of the SFA, when the field intensity lowers. Furthermore, the classical simulation can be adapted to study different dispersion relations. This would be interesting, as it allows to relate to other continua of states, e.g. in solid-state physics.

The possibility of studying the atoms' dipole response in time by measuring a single absorption spectrum enables a fascinating new approach to electron dynamics. This opens the opportunity to investigate the quantum-to-classical transition in many systems. The future might be quantum, but the power and simplicity of classical models will persist.

Appendix A

Definitions

A.1 Asymmetric $\cos^2$ Function

$$cos^2_{\text{window}}(x, max, left, right) \equiv \begin{cases} 0 & x < max - left \text{ or } x > max + right \\ \cos^2(\frac{(x-max)\pi}{2\, left}) & x > max - left \text{ and } x < max \\ \cos^2(\frac{(x-max)\pi}{2\, right}) & x > max \text{ and } x < max + right \end{cases} \tag{A.1}$$

A.2 Pulse Model

The pulse is centered *delay* after $t = 0$ with the central angular frequency ω_0 and the width τ, which describes the full width half maximum of the pulse intensity profile $I = \mathcal{E}^2$. The maximum electric field is denoted by $\mathcal{E}_{\text{max}}$.

$$\mathcal{E}(t, delay, \omega_0, \tau, \mathcal{E}_{\text{max}}) = \mathcal{E}_{\text{max}} \cdot \cos\left((t - delay)\,\omega_0\right) \cdot \exp\left(\frac{-(t - delay)^2 \cdot 2\ln(2)}{\tau^2}\right) \tag{A.2}$$

A.3 Monte Carlo Estimator

To evaluate the integral over a function $f(x)$

$$I = \int \mathrm{d}x f(x) \tag{A.3}$$

Monte Carlo integration with importance sampling can be used. To compute the integral, N random variables X_i are drawn from an arbitrary probability density function $p(x) > 0\ \forall x$ with $|f(x)| > 0$. The Monte Carlo estimator

$$I_N = \frac{1}{N} \sum_{i=1}^{N} \frac{f(X_i)}{p(X_i)} \tag{A.4}$$

approximates the integral I with an error of $\mathcal{O}(\sqrt{N})$. For details refer to [53, 54].

Appendix B

Supplementary Information on the TDSE Simulations

B.1 Condensing the Ground State

Condensation of the ground state can be achieved by negative imaginary time propagation. Setting $\mathrm{d}t = -i|\mathrm{d}t|$ converts the soft core potential into the absorbing boundary, thus excited states, which have a stronger contribution away from the origin, are suppressed. To avoid numerical problems the wave function is normalized at each step.

For this work it was not sufficient to use only the negative imaginary time propagation method. After switching to real time propagation the wave function had always an excited fraction, that spread over the grid. This is due to the fact, that the absorbing soft core potential disturbs the wave function.

Therefore, an alternative condensing scheme was implemented. The pre-condensed wave function is propagated in real time and the absorbing boundaries with $\cos^2$ shape, are slowly moved away from the origin (similar to Figure 2.10 but starting from $x_d = 5\,\mathrm{a.u.}$) until they reach their usual position. Using this method only higher excited states are damped, the ground state is less and less perturbed as it lives mainly at the origin. This procedure produced the pure ground state down to a precision of 10^{-10}.

B.2 Determine the Ionization Energy

To see which states are present in the model system, the wave function can be projected on the initial state:

$$P(t) = \langle \Psi_0 | \Psi(t) \rangle \,. \tag{B.1}$$

By a simple Fourier transform one obtains the noise spectrum of the wave function. Figure B.1 shows this noise spectrum for a propagation of 4 million steps until $t \approx 5000\,\mathrm{fs}$. One can see all bound states of the system if the initial wave function was random, in case of the condensed ground state, there is only a peak at the ionization energy I_p.

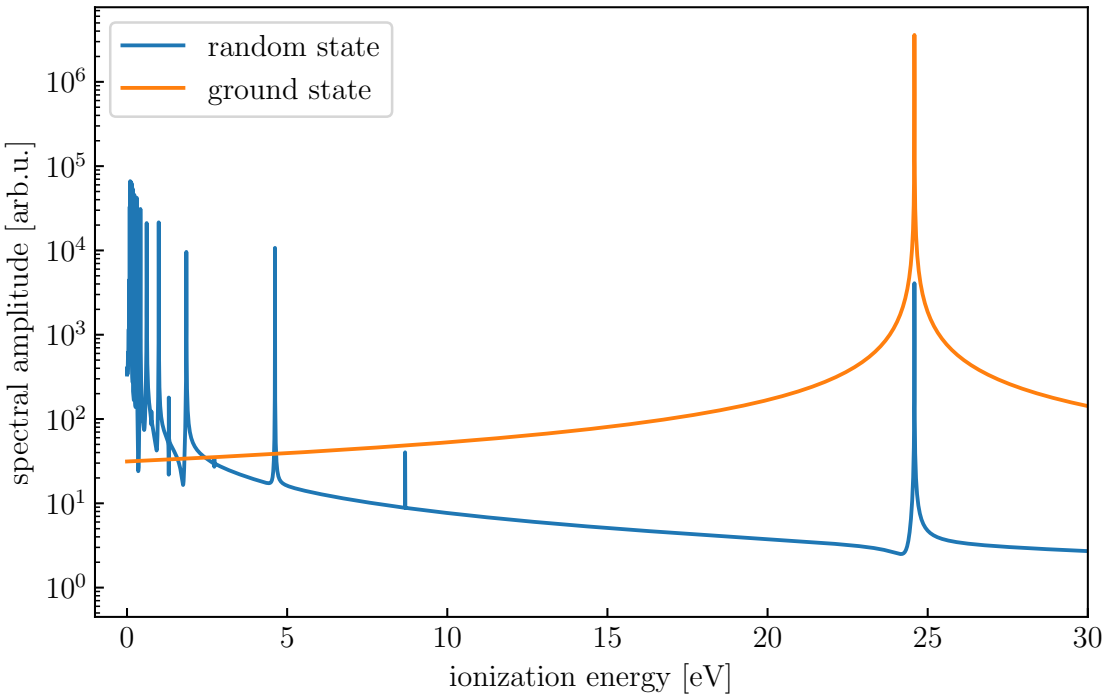

Figure B.1: Noise spectrum of a random state and of the final condensed ground state

B.3 Difference of Length and Velocity Gauge

B.2 shows the difference of length and velocity gauge in the absorption spectra. Comparison by eye reveals no difference except for a small offset in the continuum. Looking on the residuals brings to light small changes, especially of the line shapes. However, in particular in the continuum, there are no substantial differences, i.e. no features are only present for a certain gauge.
One can conclude that the choice of gauge is not important in the scope of this work.

B.4 Fit Parameters for the Intensity Scan

The Fano $*$ Gaussian fits of Figure 2.14 found the following parameters:

Table B.1: Table of the fit parameters for Figure 2.14

$I_{\max}$ [a.u.]	E_0 [eV]	q	Γ [eV]	A_0^* [arb.u.]
3.6e-5	25.738	1.235	2.1e-4	2900
4.9e-5	25.743	1.223	2.0e-4	4000
6.4e-5	25.749	1.212	1.9e-4	5600
8.1e-5	25.756	1.200	2.0e-4	6800
1.0e-4	25.763	1.190	1.7e-4	9400
1.2e-4	25.771	1.166	1.9e-4	10000

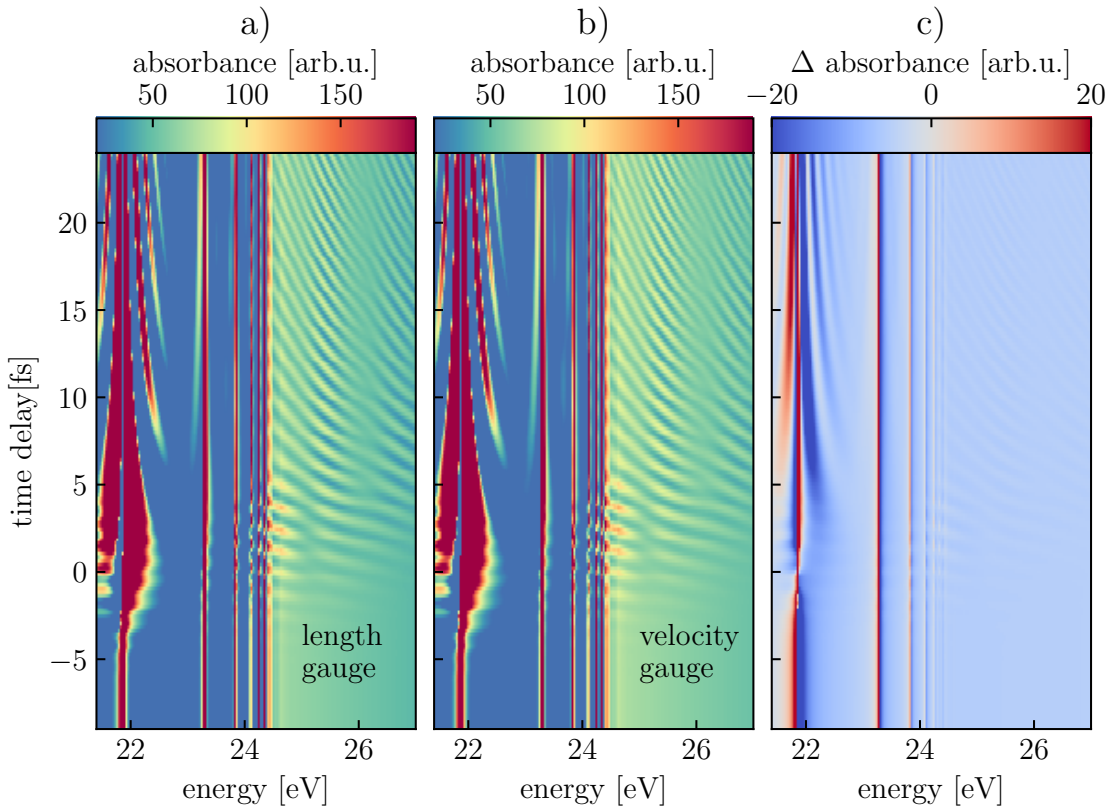

Figure B.2: Comparison of length and velocity gauge
a), **b)** show the time delay dependent absorption spectra for TDSE calculations in length gauge and velocity gauge, respectively. **c)** is the difference of absorption of length and velocity gauge $A_{\text{length gauge}} - A_{\text{velocity gauge}}$. The used parameters are: XUV Gaussian, same as Figure 2.4 a), IR: $FWHM = 5\,\text{fs}$, central frequency $\omega_0 = 1.7\,\text{eV}$, maximum intensity $I_{\text{max}} = 0.9 \times 10^{12}\,\text{Wcm}^{-2}$.

Appendix C

Complementary Methods to Simulate Absorption Spectra in SFA

In this appendix, two additional methods are shown with which absorption spectra can be computed in strong field approximation. The simulation results can be compared to the Chapter 3.

C.1 Numerical Integration

Based on the reasoning of section 1.7, we look at the dipole moment of an ionized electron wave packet. Assuming an ionization at $t = 0$ and considering only the dimension along the laser field turns Lewenstein's integral (1.25) into

$$d(t) = \langle \Psi(t)|x|\Psi(t)\rangle \tag{C.1}$$

$$= i \int \mathrm{d}p \; d_x(p + A(0)) \; d_x^*(p + A(t)) \; e^{i \int_0^t (p+A(t'))^2/2 + I_\mathrm{p} \; \mathrm{d}t'} \tag{C.2}$$

Approximating the continuum states by plane waves with momentum $\boldsymbol{p}$, the expression for the dipole matrix element to a ground state s-wave of a hydrogen-like atom writes [16]:

$$d(\boldsymbol{p}) = i \frac{2^{7/2}(2I_\mathrm{p})^{5/4}}{\pi} \frac{\boldsymbol{p}}{(\boldsymbol{p}^2 + 2I_\mathrm{p})^3}. \tag{C.3}$$

Thus, the problem reduces to solve the integral

$$x(t) \propto i \int \mathrm{d}p \; \frac{p + A(0)}{((p + A(0))^2 + 2I_\mathrm{p})^3} \; \frac{p + A(t)}{((p + A(t))^2 + 2I_\mathrm{p})^3} \; e^{i \int_0^t (p+A(t'))^2/2 + I_\mathrm{p} \; \mathrm{d}t'}. \tag{C.4}$$

For $t \gg 0$ the phase is oscillating fast, which makes it hard to solve the integral. Often the saddle-point method is used to find a solution [16]. But for $t \sim 0$ the stationary phase approximation fails. However, it is for small t possible to evaluate the integral numerically, e.g. by Romberg's method [55].

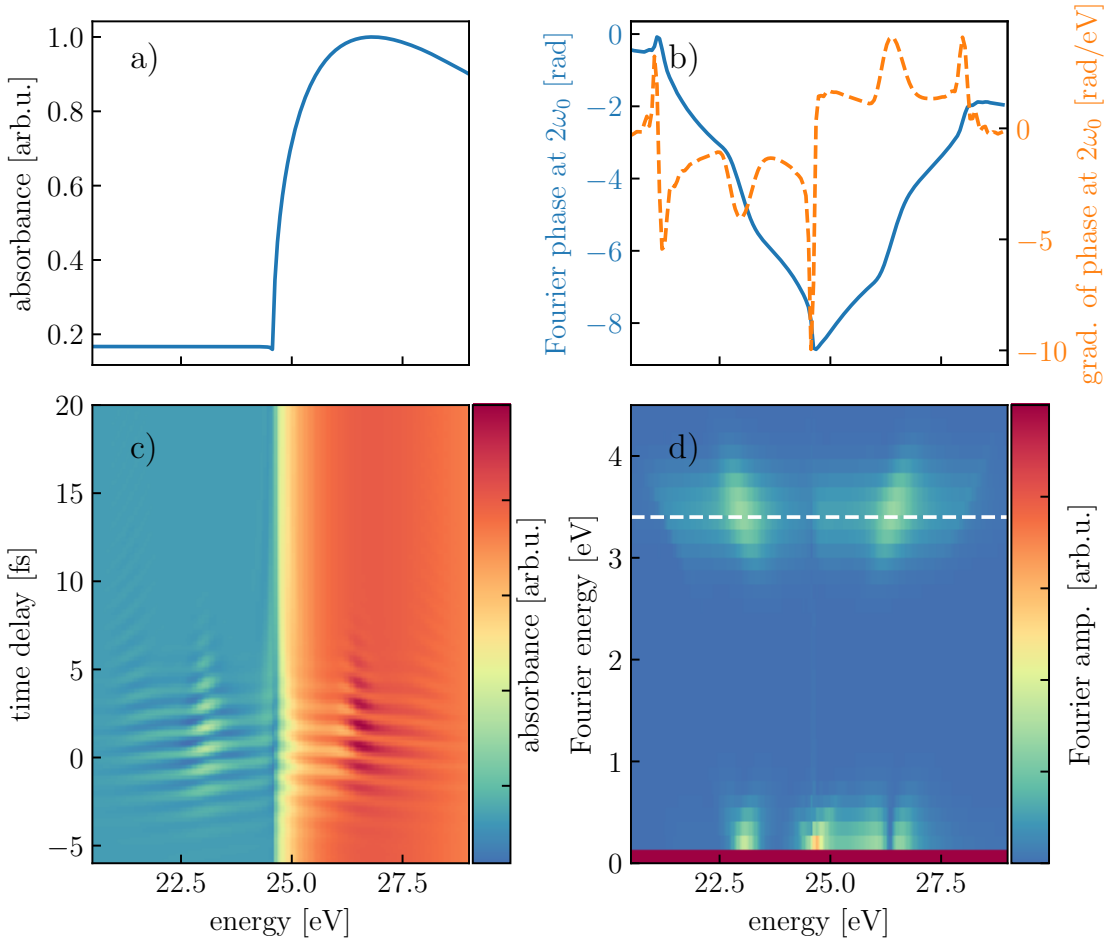

Figure C.1: **a)** The continuum edge without a strong-field, calculated by integrating equation (C.5) numerically. **b)** The Fourier phase of the $2\,\omega_0$ oscillations and its gradient (dashed). **c)** Time delay scan of the absorption spectrum at the continuum edge and **d)** its Fourier amplitude calculated by integrating equation (C.4). The DC component of the Fourier amplitude saturates to enhance the visibility of the other features. The white dashed line in d) marks the position of the $2\,\omega_0$ oscillations, for which the phase is displayed in b)

If we consider the case without a strong field $A = 0$, the integral simplifies further to

$$x(t) \propto 4\pi\, i \int_0^\infty \mathrm{d}p\, \frac{p^2}{(p^2 + 2I_\mathrm{p})^6}\, e^{it(\frac{p^2}{2} + I_\mathrm{p})}. \tag{C.5}$$

Here, the dimensionality reduces naturally by using spherical coordinates because of the isotropy.

Figure C.1 a) shows the spectral continuum edge without a strong field, calculated with the above equation (C.5). The edge is very sharp at the threshold and the absorption is only slowly diminishing for energies further above the ionization potential. Figures C.1 b) to d) display the dynamics which appear on applying a time dependent NIR field with the same parameters as in the above sections. There are features, which appeared as well in the simulations based on classical trajectories. First, a $2\,\omega_0$ oscillation dominates the time overlap of XUV and NIR pulse. Second, the edge moves with the ponderomotive shift,

which leads to a diagonal feature in the Fourier amplitude at the ionization energy. But there are as well 2 dominant differences. At $I_\mathrm{p} \pm \omega_0$ the oscillation is strongly enhanced compared to the other energies. And, as Figure C.1 b) shows, the phase at the ionization potential jumps from $-7.5\,\mathrm{rad}$ to $-9\,\mathrm{rad}$, so by $\sim \pi/2$ instead of π.

C.2 TDSE in SFA

By adapting the Time Dependent Schrödinger Equation simulations, it is possible to get the same approximations as for the classical trajectories calculations. The necessary adaptions are:

- Instantaneous ionization:
  No XUV pulse is used anymore. The propagated wave function represents in this case only the ionized fraction of the atom.

- Strong field approximation:
  The potential is set to be $V(x) = -I_\mathrm{p}$. By choosing this value instead of 0, the phase calculates correctly.

- Calculation of the dipole:
  As $\Psi(t)$ does not any longer represent the full wave function, but the ionized fraction, the dipole moment calculates to the ground state $d(t) = \langle \Psi_0 | x | \Psi(t) \rangle$.

- Initial wave function:
  The ground state wave function Ψ_0, which is approximately a Gaussian, can be used as initial state, but to account for the change in symmetry introduced by the XUV excitation, it has to be antisymmetrized $\Psi(0, x) = \Psi_0(x) \cdot 2(H(x) - \frac{1}{2})$. Here $H(x)$ denotes the Heaviside step function in the half-maximum convention.

Figure C.2 displays the resulting spectra using the above described method to adapt the TDSE. The non-perturbed spectrum exhibits not a sharp edge, but a slowly increasing absorption, that peaks sharply at I_p and diminishes slowly for higher energies. Additionally tiny oscillations arise for energies below the ionization potential, which is probably due to the finite number of states.
The time delay scan C.2 c), d) reveal $2\,\omega_0$ oscillations similar to previous observed ones. Exactly at the ionization potential in the time overlap these oscillations are much stronger than for other energies, which was not the case for the methods described in the above sections. This can be an effect of the sharp peak in the spectrum. For a more detailed analysis of the $2\,\omega_0$ oscillations, their Fourier phase is shown in Figure C.2 b). The phase jumps at the continuum threshold from $-5\,\mathrm{rad}$ to $-8\,\mathrm{rad}$, i.e. by $\sim \pi$. Whereas in the Fourier amplitude no enhancement at $I_\mathrm{p} \pm \omega_0$ is visible, the gradient of the phase shows peaks at this energy like in Figure C.1 b).

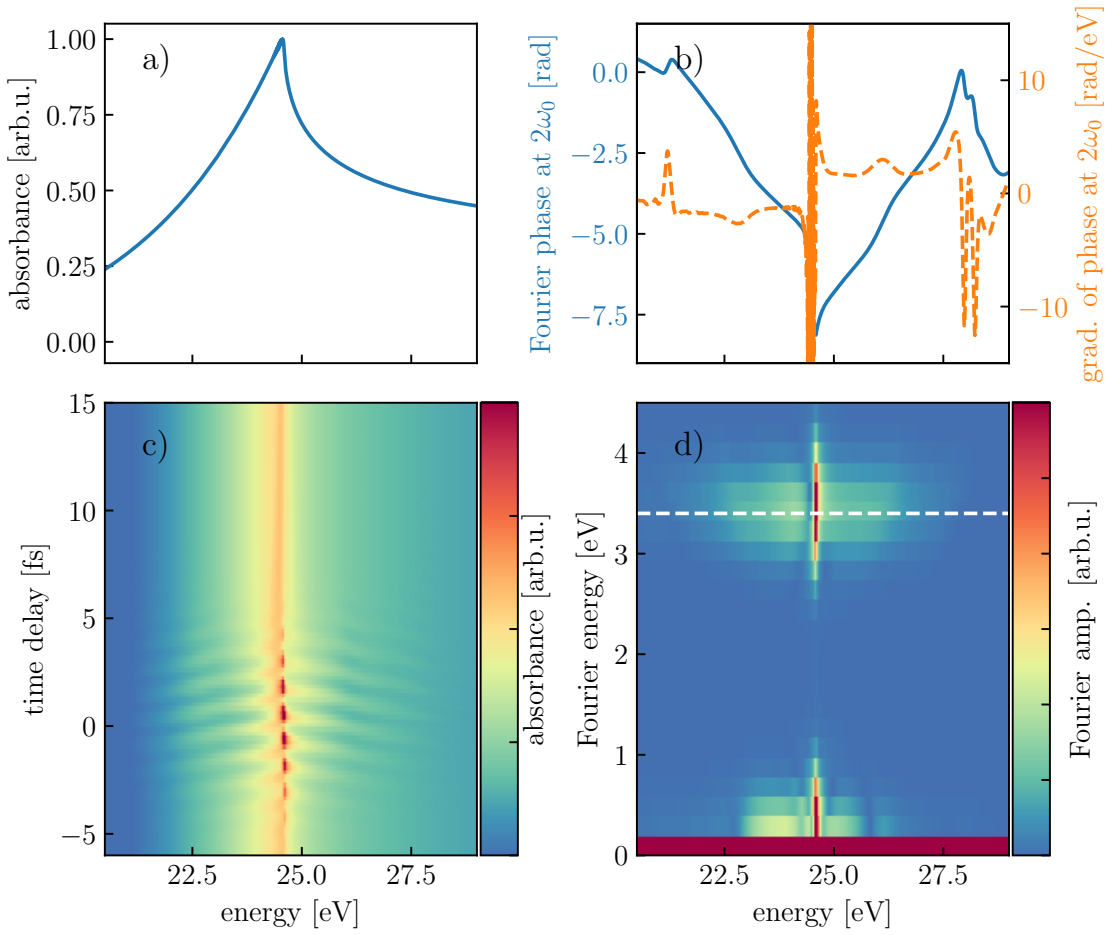

Figure C.2: **a)** The continuum edge without a strong-field, calculated the SFA adapted TDSE calculations described in this section. **b)** The Fourier phase of the $2\,\omega_0$ oscillations and its gradient (dashed). **c)** Time delay scan of the absorption spectrum at the continuum edge and **d)** its Fourier amplitude. The DC component of the Fourier amplitude saturates to enhance the visibility of the other features. The white dashed line in d) marks the position of the $2\,\omega_0$ oscillations, for which the phase is displayed in b)

Appendix D

Alignment Procedure

This chapter should give an overview over the alignment steps which were done in order to set up a measurement with external beam path. It is written in form of a manual for potential future students, who are already familiar with the beamline and who want to work with the external way to couple in.

- Insert the beam splitter into the beam path after the chirped mirrors
- Do a D-scan to check how to correct the wedges for the additional dispersion
- Check that in both arms identical focusing mirrors are used
- Align the NIR which is going through the HHG chamber in the usual manner (central through iris and inner mirror)
- Pre-align the external NIR to the center of the incoupling window
- Build in the mirror with the hole:
  It makes sense to cut out the central mode of the Ti:Sa with an iris after the beam splitter. Then the attenuated, aligned, central Ti:Sa mode can be used to align the hole mirror correctly. The first alignment should be done by turning the flange in such a way, that the hole is central in the beam mode. Additionally in the outcoupled beam it can be checked that the transmitted mode is as round as possible. If the mode is elliptical, the mirror is not hit at 45 degree. Now the external NIR should be unblocked. If the external NIR is far of the HHG NIR (maybe it is even not hitting the outer mirror) the hole mirror can be slightly unscrewed and adjusted in angle. If the difference is small, it might be enough to turn only the micrometer screws of the mirror mount. After changing the angle, the hole will not overlap any more with the central Ti:Sa mode. Thus, one has to iteratively readjust the position by turning the flange and tuning the angle. Find a good spot and tighten the screws of the flange. In all preceding alignments of the Ti:Sa into the beam line, the hole will replace the iris.
- Overlay both NIR beams exactly by tuning the focusing mirror of the external beam path and the flat mirror before. In the outcoupled picture, the external NIR should

have the dark spot in the center (beam hits the hole perfectly) and the HHG NIR should be central in the doughnut mode (both NIR beams are co-propagating)

- Check the focus z-position of the HHG NIR and the external NIR beam with a knife edge scan [56] (only with attenuated Ti:Sa). If the HHG is stable enough, the XUV focus can as well be determined instead of the HHG NIR. If the foci do not match, the focusing mirror of the external beam path has to be adjusted.
- This step is not necessary but it makes it much easier to find a coarse temporal overlap. Install a HeNe which has a reduced coherence length and overlay the beam path of the NIR with it. Overlay the outcoupled external and the HHG beam on a camera. Move the time delay stage with the micrometer screw until interference fringes appear. They should be visible $\pm 70\,\mu$m around the best spot.

The next steps have to be repeated each time the NIR is newly coupled into the beamline.

- Make sure that the HHG NIR is going centrally through the hole of the mirror. Try to overlay it as best as possible with the external beam (procedure as above)
- Achieve HHG e.g. with Xenon
- Find the best position for the target cell to have the highest XUV throughput and note it (x, y)
- Block the HHG NIR beam and try Argon harmonics in the target cell with the external NIR. This step might be a bit tricky. First move the target cell until you are sure that the NIR is going through the hole (high background signal on the Pixis camera). Then play with the wedges and make sure that the polarization is linear. It might also be, that harmonics are produced but an angle of the NIR hinders the XUV to hit the chip. Once a signal is found, optimize the argon harmonics.
- If the wedges are a lot different from the best position for HHG of the main beam, you can adjust the glass insertion in the external beam path.
- Move the target cell slowly to its best position for the XUV and follow with the NIR focus by GENTLY touching one of the last two mirrors of the external beam line. Make sure not to lose the argon harmonics signal.
- 'Switch on' main HHG. Now on the camera the autoionizing states of argon and the argon harmonics should be visible at the same time.
- Move the time delay piezo until the lines disappear (temporal overlap) while Argon harmonics are still visible (spatial overlap given).
- If the temporal overlap is found, you can tune the spatial overlap buy very gently touching the external mirrors to blow away the lines best as possible.
- To determine the temporal overlap a time delay scan can be measured (with an iris position that the lines never disappear completely).
- Now do your experiment. Good luck!

Appendix E

Additional Experimental Information

E.1 NIR Spectrum

The spectrum of the NIR light, which was used in the above described experiments is shown in Figure E.1.

E.2 Intensity Calibration

The intensity of the NIR was regulated by a motorized iris. The approximate mapping of iris position to intensity is shown in table E.1. For this calibration, the power of the outcoupled beam at a given iris position was measured. Additionally, a camera recorded the focus of the beam. The camera has a pixel size of 5.5 * 5.5 μm^2. The maximal intensity can be calculated out of the ratio of the counts of the brightest pixel to the total counts (background subtracted). With a pulse length of 5 fs (value reconstructed by a dispersion scan) and the repetition rate 3 kHz the intensity of the pulse can be estimated. Unfortunately, only pictures of the focus for iris positions 30 and 50 have been captured. The focus size changes for further closed iris positions are taken from a different measurement without external beam path. Since filters cut out the innermost part of the mode for this setup, the foci will be roughly comparable. But especially the lowest intensity values have a huge error, because for these the difference between external NIR and HHG NIR are most dominant. Thus, the intensity values only give the order of magnitude.

E.3 Sub-cycle resolved measurement of the absorption spectra in the continuum of helium

The presented data in Figure E.2 has been measured by Paul Birk before this thesis has started. It motivates the study of the phase of the $2\,\omega$ modulation in time delay, as it was done in Chapter 3. The data shows a phase-jump of ~ 2.2 rad directly at the ionization potential.

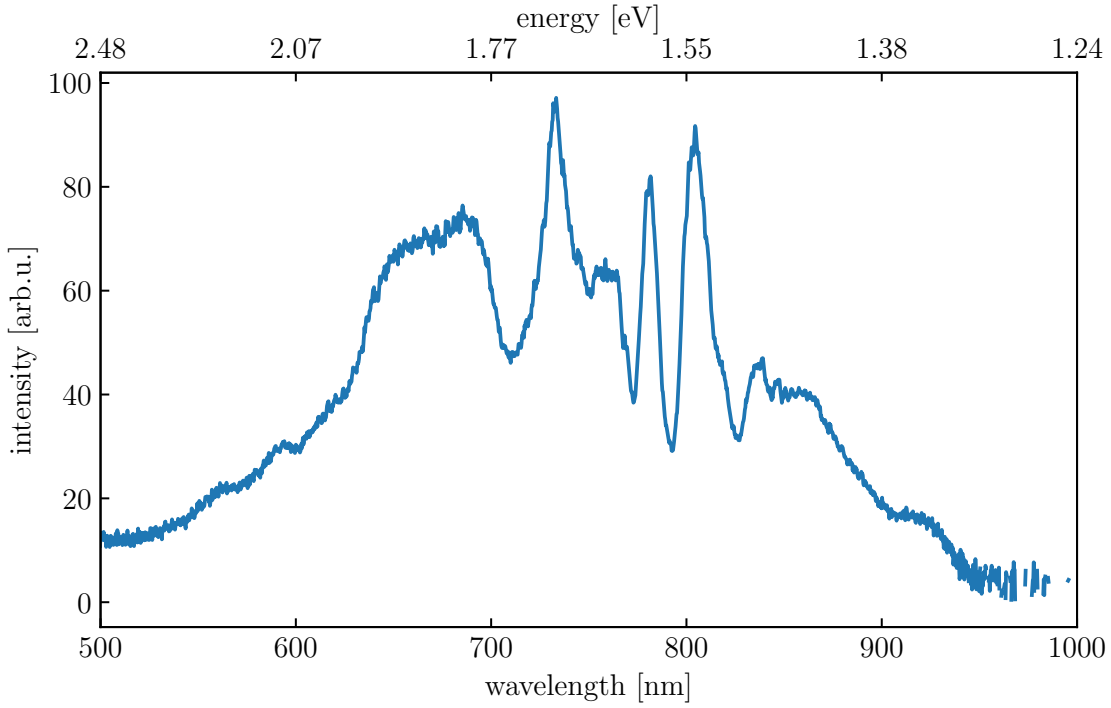

Figure E.1: The spectrum of the external NIR measured before the experiment at the position of the delay stage.

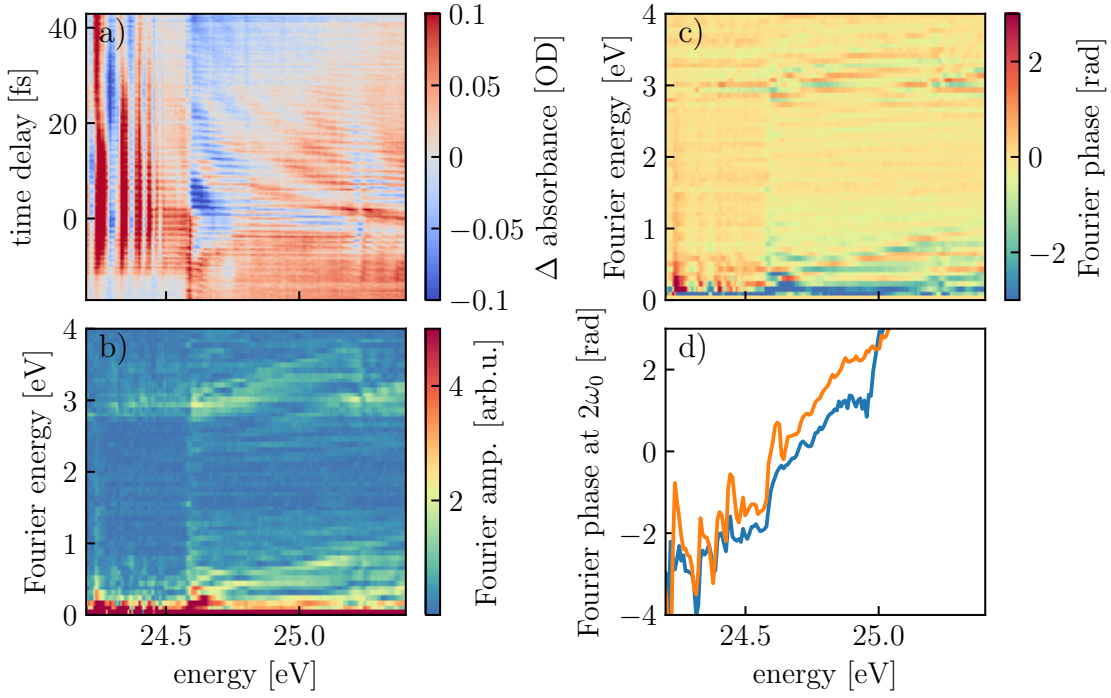

Figure E.2: Sub-cycle resolved transient absorption spectra of helium at the continuum threshold

a) Difference of optical densities with NIR light and without in the vicinity of the first ionization threshold of helium. **b)** **(c)** Fourier amplitude (phase) of the absorption oscillations along time delay of a). **d)** Lineouts of c) taken at 2.90 eV and 2.96 eV Fourier energy in blue and orange.

Table E.1: Peak intensity calibration for different iris positions
The intensity values marked with a * are estimates based on focus measurements from Maximilian Hartmann.

iris position	30	40	42	44	46	48	50	52	53
power [mW]	273	266	258	251	238	220	206	187	170
intensity [W/cm^2]	2.9×10^{14}						1.7×10^{14}		

iris position	54	55	56	57	58	59
power [mW]	160	150	137	123	108	95
intensity* [W/cm^2]		9.2×10^{13}		6.7×10^{13}	5.3×10^{13}	4.3×10^{13}

iris position	60	61	62	63	64
power [mW]	80	63	50	36	20
intensity* [W/cm^2]	3.2×10^{13}	2.0×10^{13}	1.4×10^{13}	6×10^{12}	

Bibliography

[1] A. Einstein, "Über einen die Erzeugung und Verwandlung des Lichtes betreffenden heuristischen Gesichttspunkt", Analen der Physik, 132 (1905).

[2] P. Maine, D. Strickland, P. Bado, M. Pessot, and G. Mourou, "Generation of ultrahigh peak power pulses by chirped pulse amplification", IEEE Journal of Quantum Electronics **24**, 398–403 (1988).

[3] A. McPherson, G. Gibson, H. Jara, U. Johann, T. S. Luk, I. A. McIntyre, K. Boyer, and C. K. Rhodes, "Studies of multiphoton production of vacuum-ultraviolet radiation in the rare gases", Journal of the Optical Society of America B **4**, 595–601 (1987).

[4] P. M. Paul, E. S. Toma, P. Breger, G. Mullot, F. Augé, P. Balcou, H. G. Muller, and P. Agostini, "Observation of a train of attosecond pulses from high harmonic generation", Science **292**, 1689–1692 (2001).

[5] P. B. Corkum, "Plasma perspective on strong field multiphoton ionization", Physical Review Letters **71**, 1994–1997 (1993).

[6] V. Stooß, S. M. Cavaletto, S. Donsa, A. Blättermann, P. Birk, C. H. Keitel, I. B řezinová, J. Burgdörfer, C. Ott, and T. Pfeifer, "Real-time reconstruction of the strong-field-driven dipole response", Physical Review Letters **121**, 173005 (2018).

[7] U. Scherz, *Quantenmechanik : Eine Einführung mit Anwendungen auf Atome, Moleküle und Festkörper* (Teubner, 1999), pp. 17–18.

[8] B. Thaller, *Visual quantum mechanics: selected topics with computer generated animations of quantum mechanical phenomena* (Springer, 2000), pp. 58–62.

[9] D. Meschede, *Gerthsen physik*, 24th ed. (Springer, 2010).

[10] A. Browaeys, D. Barredo, and T. Lahaye, "Experimental investigations of dipole–dipole interactions between a few rydberg atoms", Journal of Physics B: Atomic, Molecular and Optical Physics **49**, 152001 (2016).

[11] F. B. Dunning, J. J. Mestayer, C. O. Reinhold, S. Yoshida, and J. Burgdörfer, "Engineering atomic rydberg states with pulsed electric fields", Journal of Physics B: Atomic, Molecular and Optical Physics **42**, 022001 (2009).

[12] A.Kramida, Yu.Ralchenko, J.Reader, and N. A. Team, *Nist atomic spectra database*, `https://physics.nist.gov/asd`, retrieved: [2020, January 29].

[13] S. Harris, J. Macklin, and T. Hänsch, "Atomic scale temporal structure inherent to high-order harmonic generation", Optics Communications **100**, 487–490 (1993).

[14] X. Feng, S. Gilbertson, H. Mashiko, H. Wang, S. D. Khan, M. Chini, Y. Wu, K. Zhao, and Z. Chang, "Generation of isolated attosecond pulses with 20 to 28 femtosecond lasers", Physical Review Letters **103**, 183901 (2009).

[15] C. Kern, M. Zürch, and C. Spielmann, "Limitations of extreme nonlinear ultrafast nanophotonics", Nanophotonics **4**, 303 (2015).

[16] M. Lewenstein, P. Balcou, M. Y. Ivanov, A. L'Huillier, and P. B. Corkum, "Theory of high-harmonic generation by low-frequency laser fields", Physical Review A **49**, 2117–2132 (1994).

[17] P. Birk, V. Stooß, M. Hartmann, G. Borisova, A. Blaettermann, T. Heldt, K. Bartschat, C. Ott, and T. Pfeifer, "Attosecond transient absorption of a continuum threshold", Journal of Physics. B, Atomic, Molecular and Optical Physics **submitted** (2020).

[18] Q. Su and J. H. Eberly, "Model atom for multiphoton physics", Physical Review A **44**, 5997–6008 (1991).

[19] S. C. Rae, X. Chen, and K. Burnett, "Saturation of harmonic generation in one- and three-dimensional atoms", Physical Review A **50**, 1946–1949 (1994).

[20] L. Roso, L. Plaja, P. Moreno, E. C. Jarque, J. V. de Aldana, J. Roman, and C. Ruiz, "Multielectron atomic models using the rochester one-dimensional potential", Laser physics **15**, 1393–1409 (2005).

[21] Y.-C. Han and L. B. Madsen, "Comparison between length and velocity gauges in quantum simulations of high-order harmonic generation", Physical Review A **81**, 063430 (2010).

[22] J. Zhang and T. Nakajima, "Influence of coulomb potential for photoionization of h atoms in an elliptically polarized laser field: velocity gauge versus length gauge", Physical Review A **77**, 043417 (2008).

[23] S. Chen, M. J. Bell, A. R. Beck, H. Mashiko, M. Wu, A. N. Pfeiffer, M. B. Gaarde, D. M. Neumark, S. R. Leone, and K. J. Schafer, "Light-induced states in attosecond transient absorption spectra of laser-dressed helium", Physical Review A **86**, 063408 (2012).

[24] M. Wu, S. Chen, S. Camp, K. J. Schafer, and M. B. Gaarde, "Theory of strong-field attosecond transient absorption", Journal of Physics. B, Atomic, Molecular and Optical Physics **49**, 62003 (2016).

[25] M. Chini, X. Wang, Y. Cheng, Y. Wu, D. Zhao, D. A. Telnov, S.-I. Chu, and Z. Chang, "Sub-cycle oscillations in virtual states brought to light", Scientific Reports **3**, 1105 (2013).

[26] S. Chen, M. Wu, M. B. Gaarde, and K. J. Schafer, "Quantum interference in attosecond transient absorption of laser-dressed helium atoms", Physical Review A **87**, 033408 (2013).

[27] S. H. Autler and C. H. Townes, "Stark effect in rapidly varying fields", Physical Review **100**, 703–722 (1955).

[28] S. Yan, M. T. Seidel, and H.-S. Tan, "Perturbed free induction decay in ultrafast mid-ir pump-probe spectroscopy", Chemical Physics Letters **517**, 36–40 (2011).

[29] T. Ding, "Time-resolved spectroscopy of autoionizing states in few-electron systems", MA thesis (Universität Heidelberg, 2013).

[30] U. Fano, "Effects of configuration interaction on intensities and phase shifts", Physical Review **124**, 1866–1878 (1961).

[31] C. Ott, A. Kaldun, P. Raith, K. Meyer, M. Laux, J. Evers, C. H. Keitel, C. H. Greene, and T. Pfeifer, "Lorentz meets fano in spectral line shapes: a universal phase and its laser control", Science **340**, 716–720 (2013).

[32] L. Armstrong, B. L. Beers, and S. Feneuille, "Resonant multiphoton ionization via the fano autoionization formalism", Physical Review A **12**, 1903–1910 (1975).

[33] Y. Heller, V. Lukinykh, A. Popov, and V. Slabko, "Experimental evidence for a laser-induced autoionizing-like resonance in the continuum", Physics Letters A **82**, 4–6 (1981).

[34] S. S. Dimov, L. I. Pavlov, K. V. Stamenov, Y. I. Heller, and A. K. Popov, "Laser-induced nonlinear resonances in the continuum at third-harmonic generation in na vapor", Applied Physics B **30**, 35–40 (1983).

[35] T. Halfmann, L. P. Yatsenko, M. Shapiro, B. W. Shore, and K. Bergmann, "Population trapping and laser-induced continuum structure in helium: experiment and theory", Physical Review A **58**, R46–R49 (1998).

[36] P. Knight, M. Lauder, and B. Dalton, "Laser-induced continuum structure", Physics Reports **190**, 1–61 (1990).

[37] K. Amini, J. Biegert, F. Calegari, A. Chacón, M. F. Ciappina, A. Dauphin, D. K. Efimov, C. F. de Morisson Faria, K. Giergiel, P. Gniewek, A. S. Landsman, M. Lesiuk, M. Mandrysz, A. S. Maxwell, R. Moszyński, L. Ortmann, J. A. Pérez-Hernández, A. Picón, E. Pisanty, J. Prauzner-Bechcicki, K. Sacha, N. Suárez, A. Zaïr, J. Zakrzewski, and M. Lewenstein, "Symphony on strong field approximation", Reports on Progress in Physics **82**, 116001 (2019).

[38] J. Dormand and P. Prince, "A family of embedded runge-kutta formulae", Journal of Computational and Applied Mathematics **6**, 19–26 (1980).

[39] A. Blättermann, C. Ott, A. Kaldun, T. Ding, and T. Pfeifer, "Two-dimensional spectral interpretation of time-dependent absorption near laser-coupled resonances", Journal of Physics B: Atomic, Molecular and Optical Physics **47**, 124008 (2014).

[40] C. Figueira de Morisson Faria, P. Salières, P. Villain, and M. Lewenstein, "Controlling high-order harmonic generation and above-threshold ionization with an attosecond-pulse train", Physical Review A **74**, 053416 (2006).

[41] E. Goulielmakis, Z.-H. Loh, A. Wirth, R. Santra, N. Rohringer, V. S. Yakovlev, S. Zherebtsov, T. Pfeifer, A. M. Azzeer, M. F. Kling, S. R. Leone, and F. Krausz, "Real-time observation of valence electron motion", Nature **466**, 739–743 (2010).

[42] J. Mauritsson, T. Remetter, M. Swoboda, K. Klünder, A. L'Huillier, K. J. Schafer, O. Ghafur, F. Kelkensberg, W. Siu, P. Johnsson, M. J. J. Vrakking, I. Znakovskaya, T. Uphues, S. Zherebtsov, M. F. Kling, F. Lépine, E. Benedetti, F. Ferrari, G. Sansone, and M. Nisoli, "Attosecond electron spectroscopy using a novel interferometric pump-probe technique", Physical Review Letters **105**, 053001 (2010).

[43] H. Wang, M. Chini, S. Chen, C.-H. Zhang, F. He, Y. Cheng, Y. Wu, U. Thumm, and Z. Chang, "Attosecond time-resolved autoionization of argon", Physical Review Letters **105**, 143002 (2010).

[44] V. Stooß, "Strong-field spectroscopy: from absorption to time-resolved dynamics in strong fields", PhD thesis (Universität Heidelberg, 2018).

[45] M. Hartmann, "Characterization of few-cycle laser pulses", MA thesis (Universität Heidelberg, 2016).

[46] V. Stooß, M. Hartmann, P. Birk, G. D. Borisova, T. Ding, A. Blättermann, C. Ott, and T. Pfeifer, "Xuv-beamline for attosecond transient absorption measurements featuring a broadband common beam-path time-delay unit and in situ reference spectrometer for high stability and sensitivity", Review of Scientific Instruments **90**, 053108 (2019).

[47] O. Kfir, P. Grychtol, E. Turgut, R. Knut, D. Zusin, D. Popmintchev, T. Popmintchev, H. Nembach, J. M. Shaw, A. Fleischer, H. Kapteyn, M. Murnane, and O. Cohen, "Generation of bright phase-matched circularly-polarized extreme ultraviolet high harmonics", Nature Photonics **9**, 99–105 (2015).

[48] P. Dietrich, N. H. Burnett, M. Ivanov, and P. B. Corkum, "High-harmonic generation and correlated two-electron multiphoton ionization with elliptically polarized light", Physical Review A **50**, R3585–R3588 (1994).

[49] B. P. Abbott et al. (LIGO Scientific Collaboration and Virgo Collaboration), "Observation of gravitational waves from a binary black hole merger", Physical Review Letters **116**, 061102 (2016).

[50] Z. Wang, A. C. Bovik, H. R. Sheikh, and E. P. Simoncelli, "Image quality assessment: from error visibility to structural similarity", IEEE Transactions on Image Processing **13**, 600–612 (2004).

[51] M. Reduzzi, J. Hummert, A. Dubrouil, F. Calegari, M. Nisoli, F. Frassetto, L. Poletto, S. Chen, M. Wu, M. B. Gaarde, K. Schafer, and G. Sansone, "Polarization control of absorption of virtual dressed states in helium", Physical Review A **92**, 033408 (2015).

[52] S. Cavalieri, R. Eramo, and L. Fini, "Laser-induced structure in the continuum of sodium: a weak dressing field measurement", Journal of Physics B: Atomic, Molecular and Optical Physics **28**, 1793–1801 (1995).

[53] M. Pharr and G. Humphreys, *Physically based rendering: from theory to implementation* (Morgan Kaufmann, 2004).

[54] M. H. Kalos and P. A. Whitlock, *Monte carlo methods. vol. 1: basics* (Wiley-Interscience, 1986).

[55] W. Romberg, "Vereinfachte numerische integration", Norske Vid. Selsk. Forh. **28**, 30–36 (1955).

[56] F. Herzog, "Design and implementation of a gas jet array for ultrafast time-resolved absorption spectroscopy", BA thesis (Universität Heidelberg, 2019).

Danksagung

Halt! Noch nicht zuschlagen, das Wichtigste kommt noch. Ich möchte mich ganz herzlich bei allen bedanken, die mich während meiner Masterarbeit unterstützt haben!

Zuallererst gilt mein Dank Thomas Pfeifer und Christian Ott, die es mir ermöglicht haben, diese Arbeit in ihrer Gruppe durchzuführen und mir in vielen Diskussionen fachlich sehr zur Seite gestanden haben. Ein herzliches Dankeschön geht ebenfalls an Robert Moshammer, der freundlicherweise die Zweitkorrektur übernommen hat.

Ich möchte mich zutiefst bei Gergana und Paul für die gesamte Betreuung bedanken, für all die Zeit, die sie mit mir bis spät im Labor, für das Diskutieren von Daten und das Korrekturlesen meiner Arbeit aufgebracht haben. Ich habe viel von euch gelernt! Ebenfalls möchte ich die restliche Arbeitsgruppe mit einschließen, die mir bei Fragen immer zur Seite stand und mit dem ein oder anderem Spielchen am Kickertisch für aktive Pausen sorgte. Ich habe mich sehr wohl bei euch gefühlt.

Weiterhin geht ein großes Dankeschön an alle weiteren Korrekturlesenden. Ihr habt mir mit eurer Sicht auf den Text sehr geholfen Fehler zu finden und Formulierungen zu verbessern.

Ich möchte mich auch bei meinen Freunden und meiner Familie bedanken, die mich immer unterstützt haben. Bei meinen Eltern und meinem Bruder und ganz besonders bei meiner Freundin Anni. Danke, dass du es ermöglicht hast, dass ich diese Arbeit schreiben konnte und in all den vielen Stunden, die ich am Institut verbracht habe, dich liebevoll um unsere Tochter gekümmert hast. Danke, dass du immer für mich da warst.

Und zuletzt: Danke Nora! Die Zeit, die wir miteinander verbracht haben, hat mich immer wieder geerdet und jedes Quieken von dir hat mir neue Motivation gebracht. Vielen Dank, dass es dich gibt.

Erklärung:

Ich versichere, dass ich diese Arbeit selbstständig verfasst habe und keine anderen als die angegebenen Quellen und Hilfsmittel benutzt habe.

Heidelberg, den 20.02.2020 .....